

The response of the corona to different spatial distributions of heat input

Dissertation

zur Erlangung des mathematisch-naturwissenschaftlichen Doktorgrades

“Doctor rerum naturalium”

der Georg-August-Universität Göttingen

im Promotionsprogramm PROPHYS

der Georg-August University School of Science (GAUSS)

vorgelegt von

Tijmen van Wettum

aus Nieuwegein / The Netherlands

Göttingen, 2013

Betreuungsausschuss

Prof. Hardi Peter

Max-Planck-Institut für Sonnensystemforschung, Göttingen, Germany

Prof. Jens Niemeyer

Institut für Astrophysik, Georg-August-Universität Göttingen, Germany

Mitglieder der Prüfungskommission

Referent: Prof. Hardi Peter

Max-Planck-Institut für Sonnensystemforschung, Göttingen, Germany

Korreferent: Prof. Jens Niemeyer

Institut für Astrophysik, Georg-August-Universität Göttingen, Germany

Weitere Mitglieder der Prüfungskommission:

Prof. Dr. Manfred Schüssler

Max-Planck-Institut für Sonnensystemforschung, Göttingen, Germany

Prof. Dr. Laurent Gizon

Max-Planck-Institut für Sonnensystemforschung, Göttingen, Germany

Prof. Dr. Ansgar Reiners

Max-Planck-Institut für Sonnensystemforschung, Göttingen, Germany

Prof Dr. Ulrich R. Christensen

Max-Planck-Institut für Sonnensystemforschung, Göttingen, Germany

Tag der mündlichen Prüfung: 26. 09. 2013

Bibliografische Information der Deutschen Nationalbibliothek

Die Deutsche Nationalbibliothek verzeichnet diese Publikation in der Deutschen Nationalbibliografie; detaillierte bibliografische Daten sind im Internet über <http://dnb.d-nb.de> abrufbar.

ISBN 978-3-942171-76-2

uni-edition GmbH 2013

<http://www.uni-edition.de>

© Tijmen van Wettum



This work is distributed under a
Creative Commons Attribution 3.0 License

Printed in Germany

Contents

Summary	9
1 Introduction	11
1.1 Our central star	11
1.2 Solar atmosphere	12
2 Motivation	15
2.1 The hot Corona	15
2.2 Coronal energy budget	16
2.3 Heating mechanisms	17
2.3.1 AC heating	17
2.3.2 DC heating	18
2.3.3 No consensus	19
2.4 Modelling of the Solar corona	19
2.4.1 1D models	19
2.4.2 3D coronal box models	20
2.4.3 Dopplershifts	21
2.5 Motivation for present study	22
3 Magneto Hydro-Dynamics	23
3.1 Maxwell Equations	23
3.2 Ohm's law	24
3.3 MHD equations	25
3.3.1 Continuity equation	25
3.3.2 Equation of motion	26
3.3.3 Energy equation	27
3.3.4 Induction equation	30
3.4 Vector Potential	31
3.5 Ordering of plasma along the magnetic field.	31
3.6 Poynting flux	32
3.7 The flow of energy in the model	32
4 Treatment of model corona	35
4.1 Model philosophy	35
4.2 Numerical scheme used by the Pencil Code	35
Time step	36

4.3	Implementation of the MHD equations	36
	Coronal module	37
4.4	Numerical model setup	38
4.4.1	Boundary conditions	38
4.4.2	Initial conditions	39
4.5	Heating parametrizations	40
4.5.1	Ohmic heating in the model	41
4.5.2	Alfvénic heating	41
4.5.3	MHD turbulence	42
4.6	Synthetic emission	42
4.7	Mean atomic weight	43
4.8	Extraction of field-lines	45
5	Heating along individual fieldlines	47
5.1	Goal	47
5.2	Method	47
5.2.1	Horizontal averages	47
5.2.2	Heating along individual field-lines	49
5.2.3	The “random set” of field-lines	51
5.2.4	From field-lines to loop models	53
5.3	Details of 1D coronal models	54
5.4	One-dimensional coronal loop models	55
5.5	Conclusions	58
6	Coronal heat input and magnetic activity	61
6.1	Goal	61
6.2	Method	62
6.3	Results	62
6.3.1	Heating in time	63
6.3.2	Doppler shifts	68
6.3.3	Flux flux relation	68
6.4	Conclusion & Discussion	71
7	Testing parametrizations of coronal heating	73
7.1	Goal	73
7.2	Model set-up	73
7.3	Results	74
7.3.1	Emission	78
7.3.2	Doppler shifts	78
7.3.3	Direct comparison of heat input for parametrizations	79
7.4	Discussion and conclusion	80
8	Discussion and conclusion	85
8.1	Conclusion	85
8.2	Outlook	86
	Bibliography	87

Publications	93
Acknowledgements	95
Curriculum Vitae	97

Summary

Explaining the existence of the million degree corona on top of the much cooler Solar surface has provided scientist with a challenge for a several decades. It is not possible for a cooler object to heat something that is hotter by conduction, which implies that there is another mean of energy transport into the corona. The general consensus is that this role is taken by the magnetic fields that are ever present at the solar surface.

The focus of today's research is on the actual mechanism that thermalizes the energy transported by the magnetic field. Several mechanisms responsible for this conversion into thermal energy are being put forward. These suggestions fall often in the Alternating Current (AC) or Direct Current (DC) category. The first involves rapid changes of the magnetic field relative to the Alfvén crossing time of a coronal loop, while the second category involves slow changes. While a convincing case can be made for each suggested heating mechanism from modelling alone, the observational confirmation is lacking. The theoretical estimates on which scales the energy conversion happens in these models, are on the order of centimetres to metres. Observations, however, reach a resolution of 100 km, at best, in the relevant wavelengths, and as such no direct observational confirmation of one heating mechanism over the other is possible.

Synthetic observations derived from self-consistent 3D MHD models can provide the link between theory and observation. Investigation of the emission structures and distribution of Doppler shifts of emission lines can provide insight on which of these mechanisms is dominant. Fully self consistent 3D MHD models have already shown the feasibility of this method. In this work we will expand this approach in two ways.

First we investigate the effect of the strength of the magnetic field at the photospheric layer. We find that the behaviour of the Doppler shifts is strongly depended on the the magnetic field strength. When interpreting the stronger photospheric magnetic fields as higher magnetic activity, the patterns seen in the Doppler shifts as a function of formation temperature are consistent with observation of magnetically active stars. Also comparing the C IV emission with a proxy for the X-ray flux is roughly consistent with observations. Next we explore the observational consequences of different heating mechanisms using 3D MHD numerical experiments. This provides some insight on which of these mechanisms is dominant. For this we replace the Ohmic heating term in the energy equation with parametrized forms of the heating, which are derived from reduced MHD models. These models involve heating through Alfvén wave dissipation and MHD-turbulence. We find that the different heating parametrizations give similar coronae in terms of synthesized emission as it would be observed e.g. by EUV imaging. Thus EUV imaging alone are not sufficient to distinguish between these parametrizations. However, Doppler shift observations acquired by e.g. Hinode/EIS can provide the pivotal information. In our numerical experiments the different parametrizations of the heating leads to significantly

different distributions of the Doppler shifts of the synthesized emission lines in the transition region and corona. In particular, this applies to the average redshifts seen in the transition region and the average blueshifts in the coronal lines. Based on this, our results favour the turbulent cascade over the Alfvén wave heating, at least when considering an active region. Future observational and numerical studies will have to show to what extent this will hold in general.

Combining the results from the two investigations we conclude that different heating distributions produce different observables. But it is not trivial to conclude which distribution is the most likely.

1 Introduction

1.1 Our central star

The Sun has always played an important role in history, religion and science. Almost every religion had major role for the Sun god or goddess. The occurrence of a solar eclipse was often seen as a bad sign, and in many civilizations it was thought the Sun was being eaten by a giant monster. Therefore the prediction of such an event was considered of utter importance. As such the Chinese civilization was able to predict these already around 2000 BCE. The Greeks followed around 600 BCE. This is very impressive considering their ignorance on the nature of the cosmos. Around this time Chinese records mention the appearance of a darkening or obscuration on the solar disk. These are now understood to be sunspots.

The Dutch invention of the telescope in the beginning of the seventeenth century allowed for systematic recording of Sun spots. These recordings are still used today to reconstruct past solar activity. Some of the most well-known records of the sunspots are those by Galileo. The number of spots on the Sun follows a cycle of roughly eleven years. This was only found in the middle of the 19th century by a German astronomer Samuel Heinrich Schwabe. It might have been discovered as earlier as in the time of Galileo, if it were not for the peculiar behaviour of the Sun at that time. From roughly 1600 until 1750 nearly no sunspots appeared on the surface, and the solar cycle seemed to have stopped. Nowadays we know that the solar cycle is actually a 22 year cycle. In this cycle the magnetic North and South pole of the sun reverses and back again. During a solar minimum the Solar magnetic field is close to a dipole, but during a reversal the magnetic field becomes very chaotic. At this time strong patches of magnetic flux emerge from the solar surface. The strongest of those are able to push away the plasma and inhibit convection, making these areas show up as cool, dark patches on the solar surface, e.g. sun spots.

Core

The energy radiated away by the Sun surface originates from the core. In this region the temperature reaches well over 15 million degrees and together with the high pressure this is enough to fuse hydrogen into helium. The small difference in mass between these two atoms, is released as energy in the form of radiation and neutrinos. The latter provided the pivotal evidence that the process of nuclear fusion actually occurred in the Sun. Before that time it was thought the Sun was powered predominantly through the energy released by the gravitational contraction. This would however not agree with the age found for

the Earth and evolution to occur. The gravity powered Sun would have an estimated life-time of roughly 10 million years, whereas the age of the earth was estimated to be of the order of 5 *billion* years. The detection of the Solar neutrinos confirmed fusion takes place in the core, and the age of the Sun shifted to 5 billion years. It is expected that our star can be powered by fusion for another 5 billion years before the hydrogen runs out.

Radiative zone

It has been estimated that a photon (in the classic sense) remains between a hundred thousand and one million years inside the Sun. During this time the photon is scattered around by free electrons. This constant scattering provides a significant amount of pressure, as well as an important means of energy transport. In the radiative zone, just above the core, this is the dominant energy transport mechanism.

If one would fall into the Sun, and not burn instantly, only halfway radiative zone you would come to a rest. At this point the density equals that of a human body, i.e. water.

Convective zone

In the convective zone this mode of energy transfer changes. Convective motion takes over from radiation at roughly 86% of the Solar radius as the most efficient way of energy transport. Bubbles of hot plasma rise up from the tachocline, the interface between the radiative and the convective zone. From there the bubbles of hot plasma move upward toward the solar surface. There energy is lost through radiation. After cooling the cold plasma sinks back into the solar interior. This is what we observe as granular motion on the surface.

1.2 Solar atmosphere

The Solar atmosphere is separated in three different zones, distinguished by their different physical properties.

Photosphere

In this layer the most of the energy from the Sun is lost through radiation. The temperature at the bottom of the photosphere is 6600 K and drops further to 4300 K at the top. Not all radiation is lost directly from the photosphere, radiation in certain wavelengths are again absorbed by the upper photosphere which holds most of the observed absorption lines. The photospheric energy distribution characterizes the Solar spectrum which follows roughly a 6000 K Planck curve.

Chromosphere

The Chromosphere is named after its colourful appearance during a solar eclipse. The chromosphere is characterized by a rise in temperature, which is a result of acoustic waves dissipating. The chromosphere is very non-uniform, a view at the limbs sees this region

as a mass of spicules, or mottles as they are called on-disk, which are small jets of plasma. In contrast to the absorption-dominated photosphere the spectrum of the chromosphere is emission dominated, mainly as a result of the increasing temperatures. The temperatures in the chromosphere reach about 10,000 K.

Corona

The interface between the chromosphere and corona is the Transition Region (TR) in which is characterized by a sudden increase of temperature by several orders of magnitude. Here the temperature of the solar atmosphere surges from tens of thousands of degrees to over several million degrees.

The first mention of the solar corona was by the Byzantine historian Leo Diaconus, who mentioned a *"dim and feeble glow like a narrow band shining in a circle around the edge of the disk"* around the darkened Sun during the 968 eclipse in Constantinople. The corona is usually very faint and therefore only visible if the light of the Sun itself blocked, as is the case during a Solar eclipse. The low intensities are a result of the extremely low densities. Despite the clearly visible corona during an eclipse, the densities are lower than the best vacuum we can create on Earth. Modern observatories use a small occulter to block out the bright solar disk, or observe in high energy wavelengths in which the rest of the Solar atmosphere is not emitting.

The corona is where magnetic fields have free play and are not prohibited by the dense plasma as in the chromosphere and photosphere. This leads to coronal loops, bright loops-like structures of plasma captured by the strong magnetic fields. Also prominences, cooler and denser plasma hovering above the solar surface, kept up by magnetic fields. The magnetic fields lie at the source of extremely violent explosions, solar flares, which set off coronal mass ejection. These launch plasma from the solar surface into the interplanetary space, and if it hits Earth would be able to knock out satellites or even power plants on the surface. The extreme conditions the plasma is subject to in the corona is unique and unreproducible in laboratory conditions. Studying the corona is therefore crucial to fully understand the properties of plasma, the stuff where 99% of our universe is made of.

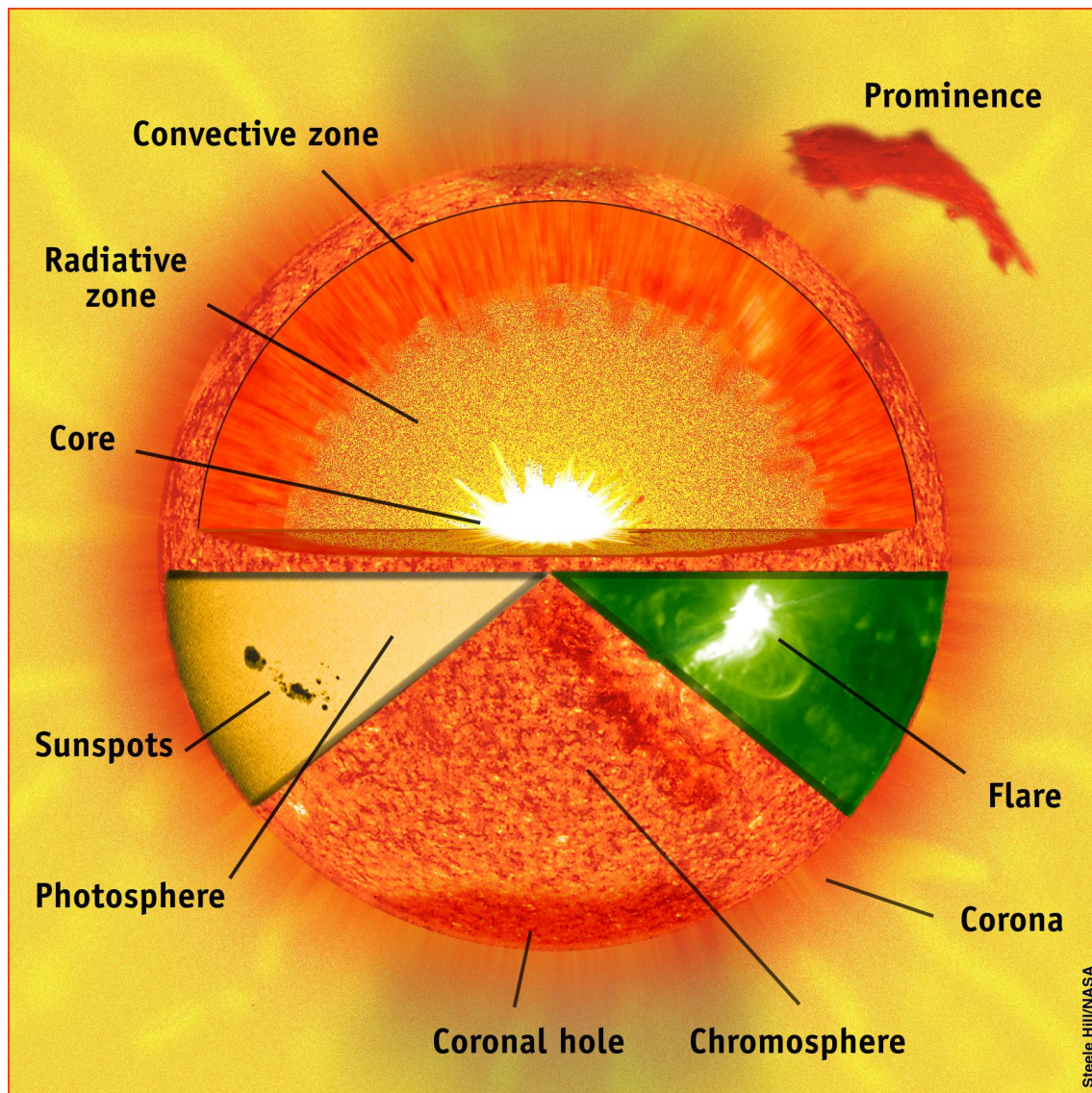


Figure 1.1: A cartoon depicting the different regions of the Sun. *Image courtesy of SOHO consortium. SOHO is a project of international cooperation between ESA and NASA.*

2 Motivation

In this chapter we discuss the context and motivation of our model. This is done by introducing the coronal heating problem, and discussing the proposed solutions. Next we give an overview on the current state of numerical models in this field and how our work fits within.

2.1 The hot Corona

The nature of the corona has been a mystery for a very long time. Several anomalous observations made this region hard to physically explain. The first to suggest the million degree solar corona was Hannes Alfvén in 1941 (Alfvén 1941). This conclusion was reached after examination of several of these anomalous observations. So was the energy distribution of the continuum spectrum observed in the corona the same as the photosphere. This would imply that the light from the photosphere was scatter off free electrons in the corona.

This was supported by the near absence of the Fraunhofer (absorption) lines, scattering on a distribution of high velocity electrons would wash out most of these lines, through the wide distribution of Doppler shifts. Only remnants of the strongest absorption lines could be observed, such as H and K absorption lines from singly ionized calcium, as was discovered by Grotrian (1931). The degree of "washing out" is a measure of the mean electron velocity, and thus the temperature of the coronal electrons. This way the author found a mean electron velocity of $7.5 \cdot 10^8 \text{ cm s}^{-1}$ and later $4 \cdot 10^8 \text{ cm s}^{-1}$ (Grotrian 1934), which would correspond to temperatures of respectively $1.2 \cdot 10^6$ and $0.35 \cdot 10^6$ degrees. The existence of so-called "forbidden lines" was observed by Edlén (1943) to whom the discovery of the million degree corona is usually attributed to. These lines belong to atoms with an extremely high degree of ionization, such as Fe XIV and Ca XV. To reach these levels of ionization through collisions would require very high electron energies. These lines are called "forbidden" because of their relatively low change of spontaneous de-excitation, which allows the ion to stay in an excited state for a long time. In higher densities the collisional de-excitation rates are therefore much higher than the spontaneous ones. The coronal densities are however very low, so that the collisions are so infrequent as to allow the spontaneous (radiative) de-excitation of these excited states. The existence of these highly ionized atoms, as well as the degree of Doppler broadening of the emission lines, would require temperatures of the order of a million degrees.

These, and several other lines of evidence, led to the conclusion that the corona actually *is* one million degrees and over. Something that was not expected at that time. This discovery led to a new question, "How is the corona heated?", which, in a slightly modified

version, remains one of the greatest unanswered questions in physics.

2.2 Coronal energy budget

The temperature of the corona is remarkably robust. If we think of a simplified picture of a coronal loop in equilibrium, with energy being deposited in the corona, a majority of this energy is transported downward through heat conduction and subsequently lost in the chromosphere through radiation. Scaling laws of coronal temperature and pressure based on this principle were derived as the RTV-scaling laws (Rosner et al. 1978), who found these as a result of early 1D models. They developed an order-of-magnitude estimate on how the apex temperature of a coronal loop scales with the energy input. When assuming all energy is transported downward and is lost there predominantly through radiation, we can construct a energy-balance equation

$$L_{\text{rad}} \approx \nabla \cdot \mathbf{q} \approx H \quad (2.2.1)$$

where, the radiative losses, $L_{\text{rad}} \propto \rho^2 T^\alpha$, are a function of the density ρ and temperature T . α is a result of approximating the radiative losses by a piecewise power law. This is of the same order as the second term, the energy conduction, which is given by $\mathbf{q} \propto T^{5/2} \nabla T$. This term is again of the same order as the energy input, H . We ignore here all the constants since our interest lies in how the terms scale with each other, not the absolute values. The full equations, including the constants are discussed in chapter 3.

The values of α are approximated by $-1/2$, which provides a good fit over the range of 10^5 K to 10^7 K. We know that for a classical gas $\rho \propto p/T$, where we take the pressure p to be constant along the loop. Estimating ∇ with the loop length $1/L$, leads to two scaling laws:

$$T_{\text{top}} \propto H^{2/7} L^{4/7}, \quad (2.2.2)$$

$$p \propto H^{6/7} L^{5/7}. \quad (2.2.3)$$

These laws relate the temperature at the top of the loop, T_{top} and the pressure, p , with the heating rate and loop length. The first scaling law shows that the temperature of a coronal loop is rather insensitive to the energy input. In order to double the coronal temperature, one needs to increase the energy input by more than a factor 10.

The coronal heating problem becomes apparent when considering the lower lying and cooler photosphere. The heating requires an upward non-thermal transport of energy through the lower cooler regions and a mechanism to deposit this energy into the corona. To balance the energy losses of the corona through radiation, particle acceleration and conduction, requires an energy flux of $3 \cdot 10^2$ Watt m^{-2} , for the quiet sun, to 10^4 Watt m^{-2} in active regions (Withbroe and Noyes 1977).

The magnetic fields that are ever present on the Sun provide both the means of energy transport and more than enough energy to keep the corona at one million degrees Aschwanden (2004). There is, however, no consensus in what way the magnetic energy is converted into thermal energy.

2.3 Heating mechanisms

It is clear from various observations that the heating of the corona is closely linked to the magnetic field. Strong enhancements in emission lines originating from hot plasma, coincide with regions of strong magnetic field. This puts the magnetic field at the forefront as the dominant energy carrier. This is reassuring, since acoustic waves are extremely inefficient in crossing the transition region. The drop in density in the TR causes these wave to shock and dissipate well before they reach the corona. Waves in the magnetic field can travel partially into the corona and deliver sufficient energy across the TR. Changes in the configuration of the field travel nearly unhindered through the transition region. Also this allows the transport of sufficient energy Aschwanden (2004) into the corona. The exact nature of this transport, and subsequent dissipation is still largely unknown. There are however, many suggestions which general fall within either of the two categories, alternating current (AC) heating and direct current (DC) heating. This depends on the time scales involved in respect to the time needed for an Alfvén wave to travel the across the whole loop.

2.3.1 AC heating

AC heating is characterized by fast changes in the magnetic field configuration, faster than the field line can adapt to the changing conditions. These fast changes often take the form of Alfvén waves which are excited by the convective motion at the solar surface. The downflows in the inter-granular lanes are highly turbulent (Cattaneo et al. 2003; Vögler et al. 2005; Stein and Nordlund 2006; Bushby et al. 2008) and as such causes transverse motions within the flux elements. A fraction of these waves reach the corona were, through some mechanism, they dissipate and convert the magnetic energy into thermal.

These Alfvén waves, a pure magnetic wave, have no density perturbation associated with it, and are therefore hard to detect. Tomczyk et al. (2007) reported the first observations of these waves using the high temporal and spatial resolution of the AIA instrument on SDO.

A problem with AC heating based on Alfvén waves is the strong increase of the Alfvén speed that increases from 15 km s^{-1} in the photosphere to over 1000 km s^{-1} in the corona. This leads, just as for sound waves, to a barrier. The strong reflection of the Alfvén waves allows only a small fraction of the energy to be transported into the corona. Due to the low densities in the corona this leakage of energy through the TR should be sufficient to heat the corona. The biggest obstacle for these suggestions is that Alfvén waves are notoriously hard to dissipate because of the independence on the local density.

It is suggested that field-lines in resonance have unique eigen-frequencies. When two neighbouring field-lines resonate out-of-phase, strong currents that form as a result of this could dissipate the wave energy and heat the loop (Ionson 1978). Also resonances of Alfvén waves with ions would deposit sufficient energy Aschwanden (2004). An attractive feature of the last suggestion is that it also work in open field-lines, and the deposited energy would not only be sufficient to heat the corona but also to accelerate the solar wind.

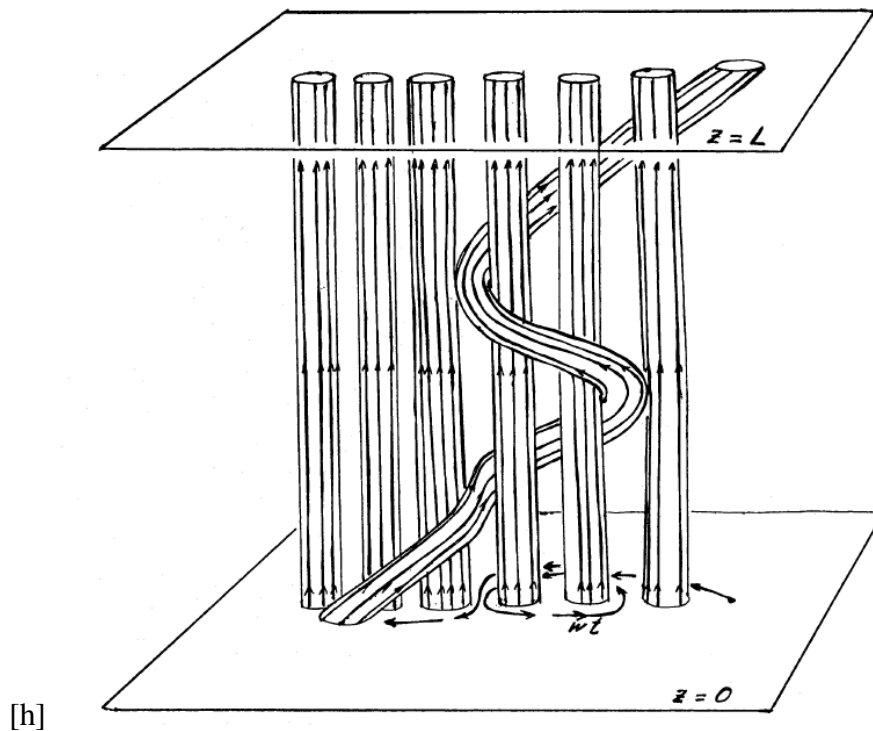


Figure 2.1: A schematic depiction of field line braiding. The cartoon depicts an unfolded loop. Photospheric motions entangle the different field-lines. Stress induced by this entanglement is released through reconnection events, which converts magnetic energy into thermal and kinetic energy. Image taken from Parker (1983)

2.3.2 DC heating

DC heating involves slowly changing magnetic fields, so that the fields can adapt to the changing conditions. These changes are thought to be induced by the granular motion of the photosphere that shuffles the magnetic fields around. In the photosphere the thermal pressure is stronger than the magnetic pressure and as such the magnetic field is forced to follow the granular flows. In the corona the field-lines are braided which induces currents which then dissipate and heat the corona. This model was first suggested by Parker (1972). This is schematically drawn in figure 2.1. In this model the energy is not continuously released, but will start when enough stress has been accumulated through the entangling of the magnetic field by photospheric motions. At a critical angle two braided magnetic field-lines will reconnect and release their stored energy as a short burst of energy. These short burst of energy are also named "nanoflares" after their relative strength in comparison to large scale flares.

The dissipation of magnetic energy in these models is thought of to occur through small scale reconnection events. This change in connectivity of field-lines induces a sudden contraction of field-lines, similar to letting go of a stretched rubber band. This causes an acceleration of the charged particles, which then collide with other particles, and in this way thermalizes the particle flow.

2.3.3 No consensus

The actual dissipation in both categories would happen on scales of well below metres, whereas the highest resolution observations reach down to roughly a hundred kilometres. Therefore all hypotheses for the heating mechanism eventually have to rely on indirect observations of the heating as the means of confirmation or falsification. It is expected that different rates and locations of heating lead to different dynamics of the corona, these can then be used as a probe to give a clue about the underlying mechanism. These observables can be Doppler shifts as a function of temperature, or the emission structure along a coronal loop.

It is, however, not trivial to conclude from the various observables the most likely heating mechanism. This is a result of the chaotic nature of the corona. Heating will cause a response of the plasma as a result of a change in the pressure balance, which in turn will change the radiative structure and subsequently influences the different observables available to us.

Large scale 3D magneto hydrodynamic (MHD) simulations are able to bridge the gap from heating to observables, but are limited by the same limitation as observations, the length-scales on which the energy conversion acts. Therefore these models have to fall back on parametrizations of the heating. Despite this limitation, the models are able to treat the heating self-consistently in time and space. Therefore realistic large scale simulations provide the link between theory and observation.

This is where this work makes a contribution. In changing the way the corona is heated, we hope to produce different structures and dynamics. These can then be used to derive several statistics that might give a hint on whether these heating mechanisms are feasible.

2.4 Modelling of the Solar corona

This subsection gives a short overview about the modelling done on the coronal heating problem and the corona in general. This is based on Peter (2007).

2.4.1 1D models

The first models developed to investigate the heating of closed coronal loops were one dimensional models. The 1D approach was required because of the limited computational power at that time, but such an approximation of a coronal loop is none-the-less a good simplification. Since the plasma is frozen-in into the magnetic field, nearly no flow across the magnetic field is allowed. The flow of plasma and the energy transport take place almost exclusively along the field-lines, and therefore one field line can be considered isolated from neighbouring lines.

Based on this principle of using the magnetic field line as a flow channel, a large amount of successful 1D models were produced. One set of these are the RTV models, which were mentioned in Sect. 2.2. Advances in computational capacity and power allowed for a more complete treatment of the coronal loops by including additional physics, such as radiative transfer and ionization. Very high resolutions are reached with the use of adaptive mesh refinement. This led to very thin transition regions, which is a result of the inefficient heat conduction at lower temperatures, which is compensated by a high

temperature gradient to accommodate the energy flux into the photosphere via heat conduction.

Besides closed coronal loops, the corona contains open field-lines. This means that the field-lines do not connect back in the nearby vicinity, but either far away or to the inter-planetary field. These open field-lines generally start from a funnel-like-structure in the corona. These originate from a concentrated magnetic field at the bottom of the corona and then fan out as a results of the difference in the pressure balance between magnetic and thermal pressure (Reeves 1976; Gabriel 1976). These funnels are believed to be the source of the solar wind (Tian et al. 2009). The emission measure, $EM = \int_V n_e dV$, calculated from funnel models were unable to reproduce the observed emission measure. This was a result of the extreme thin TR, which resulted in a too low emission at lower temperature. This lead to the proposal by Dowdy et al. (1986) of a "magnetic junk yard", a region of short and cool coronal loops which can account for the missing emission.

Despite the high resolution and high level of included physics of these 1D models, single coronal magnetic field-lines do not exist in a vacuum. Changes within one single strand has influence on neighbouring strands and vice-versa.

2.4.2 3D coronal box models

Although the energy transport and mass balance is modelled well in a 1D set-up, these models fall short in the heating mechanisms. Especially in Parker's braiding model the heating is a function of the 3D-configuration of the magnetic field. Therefore 1D models (as well as 2D models) have to rely on an ad-hoc parametrization of the heating, which often takes the form of an exponentially decreasing heating function.

The ability of Parker's field line braiding model to maintain a hot corona was demonstrated by Gudiksen and Nordlund (2002, 2005b,a). They developed a 3D MHD model which includes the photosphere and lower corona. By solving the full energy equation, including the field-aligned Spitzer heat conduction and optical thin radiative losses, the evolution of the corona is solved self-consistently. The model is driven by an evolving magnetic field at the bottom boundary, with the purpose of entangling the magnetic field-lines. This braiding results in the formation of current structures. These are assumed to dissipate and convert into thermal energy. This energy is sufficient to keep the coronal regions of the model at temperatures of the order of 1 million degrees. Statistical analysis of the results of these models show a good match with actual observations of e.g. emission structures and Doppler shifts (Peter et al. 2004, 2006).

The work presented in this thesis is based on the model developed by Bingert and Peter (2011) which follows the concept originally developed by Gudiksen and Nordlund (2005a). Also in this numerical experiment the full MHD equations, are solved. The major difference between the earlier work is the inclusion of magnetic network elements.

This type of model has proven itself successful in reproducing several observational constraints. Figure 2.2, taken from Zacharias et al. (2011), shows the Dopplershifts as a function of formation temperature. The diamonds indicate the calculated Dopplershifts from Bingert and Peter (2011). The dashed line is the trend derived from actual observations (Peter and Judge 1999). The observed red-shifts of several transition region lines are reproduced by the model. However, the observed blue shifts at higher temperature are not reproduced. This could be explained by the closed top boundary, which would

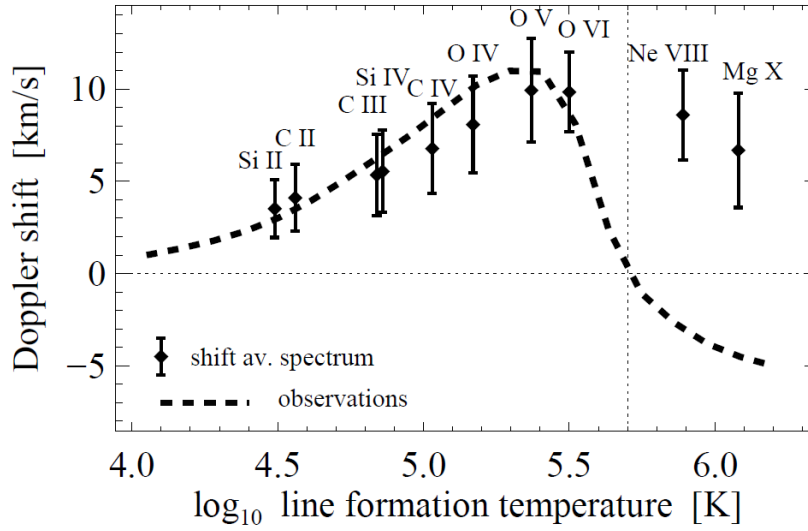


Figure 2.2: The Doppler shifts as a function of formation temperature of an active region. The diamonds are the calculated Doppler shifts from a 3D MHD simulation. The dashed line indicates the trend as derived from observations (Peter and Judge 1999). Image taken from Zacharias et al. (2011)

constrain significant up-flows. Follow-up models at higher resolution and an extended vertical range do find blue shifts at high temperature (P. Bourdin, 2013, Priv. Comm.).

Also the emission measure (EM), as derived from the model follows, the same trend as in the observations. Synthetic observations derived from synthesised emission found constant cross-sections of intensity for coronal loops as well as a similar intensity profile along the loop (Peter and Bingert 2012). Statistical analysis of the energy release shows a consistent scale-invariant distribution that is consistent with a nano-flare heated corona. These similarities to observations make the results of both models very robust.

2.4.3 Dopplershifts

The cause of the observed blue and red-shifts on the Sun are still under debate. Athay (1984) proposed that these observation could be explained by the down flows of plasma draining of cooling coronal loops. An alternative suggestion was proposed by Boris and Mariska (1982), which involved syphon flows along the coronal loops.

Spadaro et al. (2006); Hansteen et al. (2010) suggested that a localized heating would push mass up and down, away from the point of heating. This would cause lower lying, and this cooler, plasma to move downward, whereas the the higher, and hotter, plasma would move upward. This could explain the excess of observed redshift for cooler plasma, a blue shifts for hotter plasma.

2.5 Motivation for present study

In this work we want to investigate whether it is possible to use 3D-MHD models to investigate alternative heating mechanisms, such as Alfvén wave dissipation and MHD turbulence. Whether these different heating models produce observationally distinct or similar patterns is a crucial step in bridging the gap between model and observations. For this purpose we use the set up from Bingert and Peter (2011) as a starting point to investigate the effect on the corona and its dynamics as a result of different heating distributions and different levels of magnetic activity.

First we start with an investigation on the difference between the heating as a result Ohmic dissipation, and heating according to two different parametrizations presented in Sect. 4.5. We do that by investigating the different heating distributions along individual field-lines in the model from Bingert and Peter (2011), which is done in chapter 5.

Next we investigate the effect of a different magnetic field strength on the dynamics of the corona in chapter 6. We find a clear difference in Doppler shift for the models with different field strengths. This is relevant in the context of different stellar coronae for stars with different magnetic activity. Increasing the magnetic field strength, while keeping everything else constant is a first step for such an investigation. We find that the relation between the photospheric field strength and the total energy deposition in the corona is non-trivial. Additionally we find significantly different Doppler shift patterns for different magnetic field strengths. One of these models is then used as a reference model for the the next chapter.

The possibility to observationally distinguish between different heating distribution is pivotal to answer the question of the coronal heating. We want to find out if, and how, a different heating distribution changes the observables. For this purpose in chapter 7 we replace the heating though Ohmic dissipation with a parametrized for of the heating. The different distribution of heating leads similar coronal structures but to different dynamics. This makes emission structures unable to accurately distinguish between different heating mechanisms. Doppler shifts, however, show clearly distinct patters for different heating distributions. Further more the heating through MHD-turbulence produces the most Solar-like pattern in the Doppler shifts.

3 Magneto Hydro-Dynamics

In this section we describe the MHD equations and the corresponding physics that are used in our model. The actual mathematical implementation of these equations might differ, and will partially be discussed in the next chapter, the physics described by these equation do not change. A more complete introduction into solar MHD is provided by Priest (1982).

3.1 Maxwell Equations

The Maxwell equations for in a vacuum are, in differential form, given by

$$\nabla \cdot \mathbf{B} = 0 \quad \text{No monopoles,} \quad (3.1.1)$$

$$\nabla \cdot \mathbf{E} = \frac{\rho_e}{\epsilon_0} \quad \text{Gauss,} \quad (3.1.2)$$

$$\nabla \times \mathbf{E} = -\frac{\partial \mathbf{B}}{\partial t} \quad \text{Faraday,} \quad (3.1.3)$$

$$\nabla \times \mathbf{B} = \mu_0 \mathbf{j} + \frac{1}{c^2} \frac{\partial \mathbf{E}}{\partial t} \quad \text{Ampère.} \quad (3.1.4)$$

In here \mathbf{E} and \mathbf{B} denote respectively the electric and magnetic field, ρ_e the charge distribution, \mathbf{j} the current density, and t the time. ϵ_0 and μ_0 represent the permittivity and permeability of the vacuum, they relate with the speed of light, $c^2 = \frac{1}{\epsilon_0 \mu_0}$.

The first equation tells us that magnetic field-lines (imaginary lines that follow the magnetic vector field) are closed, which excludes the existence of monopoles¹. Or, in other words, the same amount of field-lines that enter an arbitrary volume in space also leave that volume.

The second equation shows that any distribution of charge in space is accompanied by an electric field radiating in- or outward. The third and last equation couple the magnetic and electric fields. Any change in one, will induce the other field. These equations give rise to electromagnetic waves, also known as photons. The last equation includes, besides the time derivative of the electric field, also the current, \mathbf{j} . This expresses a flow of charges particles.

In our setting the typical velocities, v_0 are much smaller than the speed of light, c . From this we can make some order-of-magnitude estimates. From Eq. (3.1.3) we get

$$\frac{E_0}{l_0} \approx \frac{B_0}{t_0}, \quad (3.1.5)$$

¹Recent developments in particle physics, such as grand unified theories and super string theories, do predict the existence of monopoles. However, at the moment of writing, there is no (conclusive) evidence of their existence.

with l_0 and t_0 a typical length and time. Applying this to the most right term of Eq. (3.1.4) we get

$$\frac{1}{c^2} \frac{E_0}{t_0} \approx \frac{v_0^2}{c^2} \frac{B_0}{l_0} \approx \left(\frac{v_0^2}{c^2} \right) | \nabla \times \mathbf{B} |. \quad (3.1.6)$$

We can therefore safely neglect the displacement current, $\frac{\partial \mathbf{E}}{\partial t}$, since it is much smaller than the other terms. As a result of this simplification, currents are always closed, since the divergence of a curl is always zero. This way Maxwell's version of Ampère's law then reverts back to it's original pre-Maxwellian form,

$$\nabla \times \mathbf{B} = \mu_0 \mathbf{j}. \quad (3.1.7)$$

Using the approximation of Eq. (3.1.5) we can estimate the fraction of the magnetic and electric energy densities

$$\frac{\epsilon_0 E_0^2}{B_0^2 / \mu_0} = \frac{l_0^2}{t_0^2 c^2} = \frac{v_0^2}{c^2}, \quad (3.1.8)$$

from which we see that the energy in the electric field is much smaller than in the magnetic field.

The small energy content of the electric field is also a result of the requirement of charge neutrality. From Eq. (3.1.2) we can see that the electric field depends on the distribution of charged particles. Any charge instability causes strong electric fields that move particles of opposed charge toward each other, and in doing so almost instantly negate the charge-instability. Small scale charge instabilities can occur due to the thermal motion of the particles. Typical lengths on which these thermal charge instabilities can occur are expressed by the Debye length

$$\lambda_D \equiv \sqrt{\frac{\epsilon_0 k T}{e^2 n}}, \quad (3.1.9)$$

where n denotes the electron density and e their charge, k represents the Boltzmann constant and T the temperature. For a coronal plasma this is roughly 0.07 metre. In our simulations the typical lengths are of the order hundreds of kilometres, and thus the assumption of charge neutrality is justified.

3.2 Ohm's law

For a free moving particle in a perfectly conduction fluid the electric field vanishes in the local rest frame (denoted by a prime),

$$\mathbf{E}' = \mathbf{E} + \mathbf{v} \times \mathbf{B} = 0 \quad (3.2.1)$$

where \mathbf{v} the velocity of the gyrocentre of the particle. A charged particle in a constant magnetic field with a perpendicular electric field will exhibit a drifting motion in the direction perpendicular to both. This drift velocity is given by

$$\mathbf{v} = \frac{\mathbf{E} \times \mathbf{B}}{B^2}. \quad (3.2.2)$$

Inserting this in Eq. (3.2.1) shows the electric field vanishes. In the reference frame of the particle the currents are connected with the electric field through Ohm's law

$$\mathbf{j}' = \sigma_e \mathbf{E}', \quad (3.2.3)$$

here σ_e is the *electric* conductivity. Combining this equation with the invariance of the magnetic field and the currents,

$$\mathbf{B}' = \mathbf{B} \quad \mathbf{j}' = \mathbf{j}, \quad (3.2.4)$$

this leads to Ohm's law in its simplified form

$$\mathbf{j} = \sigma_e (\mathbf{E} + \mathbf{u} \times \mathbf{B}). \quad (3.2.5)$$

Since we can express \mathbf{j} by $\frac{1}{\mu_0} \nabla \times \mathbf{B}$, the electric field has been reduced to a secondary quantity.

3.3 MHD equations

The four MHD equations are given by

$$\frac{D\rho}{Dt} = -\rho(\nabla \cdot \mathbf{u}), \quad (3.3.1)$$

$$\rho \frac{D\mathbf{u}}{Dt} = \mathbf{j} \times \mathbf{B} - \nabla p + \rho \mathbf{g}, \quad (3.3.2)$$

$$c_V(\gamma - 1)\rho \frac{DT}{Dt} = p(\nabla \cdot \mathbf{u}) + \mathcal{S}, \quad (3.3.3)$$

$$\frac{\partial \mathbf{B}}{\partial t} = \nabla \times (\mathbf{u} \times \mathbf{B}) - \nabla \times \eta (\nabla \times \mathbf{B}). \quad (3.3.4)$$

where ρ denotes the mass density, and \mathbf{u} the velocity vector. The thermal pressure is indicated by p and the gravity by \mathbf{g} . In the energy Eq. (3.3.3) c_V denotes the heat capacity at constant volume and γ the adiabatic index. \mathcal{S} includes all energy sinks and sources, which are further discussed in Sect. 3.3.3. Finally, η represents the magnetic resistivity. The different equations are discussed in the following subsections.

In the above equations we have used the Lagrangian time derivative for a comoving observer, which relates to the Eulerian time derivative for an observer at a fixed position through,

$$\frac{D}{Dt} \equiv \frac{\partial}{\partial t} + \nabla \cdot \mathbf{u}. \quad (3.3.5)$$

3.3.1 Continuity equation

The general continuity equation is in the form of

$$\frac{\partial \phi}{\partial t} = -\nabla \cdot \mathbf{f}_\phi. \quad (3.3.6)$$

This shows that any change of a conservative physical quantity ϕ in time is only due to a non-zero divergence in the flux, \mathbf{f} , of that quantity. In the case of the equation mass this flux is the mass flow, thus $\mathbf{f} = \mathbf{u}\rho$.

Eq. (3.3.1) therefore expresses that the only change in density is due to either an inflow or outflow of mass, and is not created. There are no sinks or sources for the mass, and therefore the total mass is conserved.

3.3.2 Equation of motion

Eq. (3.3.2) describes the effect of the different force densities on the plasma. These forces include the pressure, gravity and the Lorentz force.

In a rotating body other forces, such as Coriolis or centrifugal force, also act on the plasma. These are, however, too small, to be included in our model. The centrifugal force in the corona, for example, is about 0.004% of the gravitational force, and can thus be safely be neglected.

Pressure and the equation of state

In order to calculate the pressure from the density and temperature we need an equation of state. For an ideal gas, which is discussed in more detail in Sect. 4.7 this is given by

$$p = (c_p - c_v)\rho T, \quad (3.3.7)$$

which relates the temperature and density with the pressure through the specific heats. These are the specific heat at constant pressure, c_p and at constant volume, c_v . They represent the ratio of energy input and the the change in temperature as a result of this energy input, when keeping either the volume or pressure constant. The ratio between these specific heats are given by adiabatic index

$$\gamma \equiv \frac{c_p}{c_v}, \quad (3.3.8)$$

which is the case of an ideal gas is $\frac{5}{3}$. The pressure force is a result of a gradient in the pressure field.

Gravity

The gravitational force is defined as the gradient of a scalar field

$$\mathbf{f}_g = -\rho \nabla \phi. \quad (3.3.9)$$

The vertical extend of our model is about 50 Mm and is located at the solar surface. With this the gravitational force at the bottom is roughly 1.13 times stronger than at the top. Since we assume that this difference in gravity from bottom to top does not play a significant role in our modelled setting, we simplify this to

$$\mathbf{f}_g = -\rho g_\odot \hat{\mathbf{z}}, \quad (3.3.10)$$

where g_\odot is the gravity at the solar surface.

Lorentz force

The existence of currents that are not parallel to the magnetic field give rise to the Lorentz force,

$$\mathbf{f}_{\text{Lor}} = \mathbf{j} \times \mathbf{B}. \quad (3.3.11)$$

Replacing \mathbf{j} with equation Eq. (3.1.7) and expanding leads to

$$\mathbf{f}_{\text{Lor}} = \frac{1}{2\mu_0} [\nabla B^2 - 2(\mathbf{B} \cdot \nabla)\mathbf{B}]. \quad (3.3.12)$$

The first term on the right side is the gradient of the magnetic energy density, and can thus be interpreted as the magnetic pressure force. This pressure, $B^2/2\mu_0$ term acts isotropic in space.

The second term on the right side is a tension term, and cancels the magnetic pressure in the direction of the magnetic field. This term is also a straightening force for when the magnetic field is curved. The Lorentz force only acts perpendicular to the magnetic field.

Viscosity

A fluid with a non-uniform flow is subject to viscous forces. These are calculated via the non-isotropic rate-of-strain tensor, given by

$$S_{ij} = \mu \left(\frac{\partial u_i}{\partial x_j} + \frac{\partial u_j}{\partial x_i} - \frac{2}{3} \delta_{ij} \nabla \cdot \mathbf{u} \right), \quad (3.3.13)$$

where μ represents the dynamic viscosity. The force related to the viscosity is then

$$\rho \frac{D\mathbf{u}}{Dt} = \nabla \cdot S_{ij} = \rho \nu (\nabla^2 \mathbf{u} + \frac{1}{3} \nabla (\nabla \cdot \mathbf{u})) \quad (3.3.14)$$

where ν is the kinematic viscosity, which has the same units as a diffusion constant and relates to the dynamic viscosity via

$$\nu = \frac{1}{\rho} \mu \left[\frac{\text{m}^2}{\text{s}} \right]. \quad (3.3.15)$$

We can therefore think of this as 'momentum-diffusion', as it tends to remove strong gradients of momentum. The loss of momentum by viscous forces has a counter part in the energy equation, Eq. (3.3.25).

3.3.3 Energy equation

Equation (3.3.3) only considers the thermal energy. A full description of the energy flows and conversions is given in Sect. 3.7. The \mathcal{S} -term representing the different energy sinks, sources and transport terms includes the conduction, radiative losses, viscous heating, and Ohmic heating,

$$\mathcal{S} = \nabla \cdot \mathbf{q} + L_{\text{rad}} + Q_{\text{Ohm}} + Q_{\text{visc}}. \quad (3.3.16)$$

The following discusses these four terms.

Conduction

The basic equation for the diffusion of a quantity $\phi(\mathbf{x}, t)$ is

$$\frac{\partial \phi}{\partial t} = -\nabla \cdot (D \nabla \phi) \quad (3.3.17)$$

where D the diffusion factor, which could be either a scalar or a tensor.

Conduction is the manifestation of diffusion for thermal energy. In a magnetized plasma this is different from a normal gas in the sense that the majority of the conduction takes place exclusively along the magnetic field-lines. This is explained by the electrons being 'captured' by the magnetic field, as they are forced to gyrate around a magnetic field line. The larger gyro radius of the ions allows some conduction perpendicular to the magnetic field, but at a very low rate because of their limited movement range in that direction. It is therefore justified to think of conduction in an MHD gas as exclusively along the magnetic field-lines. Spitzer (1962) derived the diffusion constant for a magnetized plasma as

$$\kappa_{\text{Spitzer}} \approx \kappa_{\parallel} \delta_{ij} + (\kappa_{\perp} - \kappa_{\parallel}) b_i b_j, \quad (3.3.18)$$

which is for a coronal plasma

$$\kappa_{\parallel} \approx 2 \cdot 10^{-11} \left(\frac{T}{[\text{K}]} \right)^{\frac{5}{2}} \left[\frac{\text{W}}{\text{m K}} \right]. \quad (3.3.19)$$

The ratio of perpendicular over parallel conduction is depending on temperature, density and magnetic field

$$\frac{\kappa_{\perp}}{\kappa_{\parallel}} = 2 \times 10^{-31} \frac{n^2}{T^3 B^2} \quad (3.3.20)$$

is, under coronal conditions, in general a very small number, and thus it is justified to think of thermal conduction to be pure field aligned.

The change in thermal energy as a result of conduction is the diffusion equation, such as Eq. (3.3.17), and in its final form given as

$$\mathbf{q} = \kappa_{\text{Spitzer}} \nabla T = \kappa_{\parallel} T^{5/2} \nabla T, \quad (3.3.21)$$

where the last equality is for conduction along the magnetic field-lines.

Radiative losses

For our model we assume an optical thin medium, this implies that the radiation is a pure loss-function; no absorption takes place. For certain wavelengths the corona is slightly more opaque, but the very low density prevents thermalization of absorbed photons. Excited states will spontaneously de-excite by emitting a photon before being de-excited through a collision with another particle.

The radiative loss curve is calculated assuming ionization equilibrium. This assumption is justified when the dynamic time scales are larger than the recombination time, as is the case in the corona. This leads to radiative losses being an energy sink only, in the form of

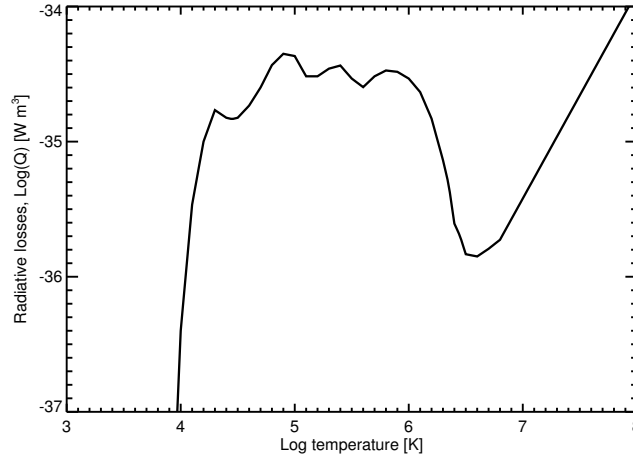


Figure 3.1: The radiative losses as a function of temperature approximated by a piecewise powerlaw. The actual radiative losses of the plasma scales with ρ^2 .

$$L_{\text{rad}} = n_e n_H Q(T) \approx \rho^2 Q(T). \quad (3.3.22)$$

The last approximation holds in case of a fully ionized plasma where $n_e = n_H \propto \rho$. The radiative loss function $Q(T)$ can be approximated by a piecewise power law

$$Q(T) = \chi T^\alpha [\text{W m}^3] \quad (3.3.23)$$

where the coefficients α and χ are specified for a number of temperature regimes. In our simulation we use the continuous loss function $Q(T)$ following Cook et al. (1989), shown in Fig. 3.1.

Ohmic heating

The plasma is heated through the dissipation of the magnetic field. Currents induced by the magnetic field are assumed to be dissipated within the grid scales. This implies that any current structure is directly thermalized, the Ohmic heating then enters the energy equations as

$$Q_{\text{Ohm}} = \mu_0 \eta \mathbf{j}^2. \quad (3.3.24)$$

This follows self-consistently from the induction equation, which will be discussed below. In two of our runs this heating term is turned off and replaced by an alternative heating, these are described in more detail in Sect. 4.5.

Viscous heating

The momentum lost by viscosity in the equation of motion is converted into thermal energy through

$$Q_{\text{visc}} = 2\rho \nu S^2, \quad (3.3.25)$$

with the rate of strain tensor defined in Eq. 3.3.13.

3.3.4 Induction equation

The induction equation follows straightforward from the two Maxwell equations, Eq. (3.1.4) and Eq. (3.1.2) in the MHD approximation. In combination with Ohms law, Eq. (3.2.5), this results in

$$\frac{\partial \mathbf{B}}{\partial t} = \nabla \times (\mathbf{v} \times \mathbf{B}) - \nabla \times (\eta \nabla \times \mathbf{B}). \quad (3.3.26)$$

For a constant resistivity, η , this simplifies to

$$\frac{\partial \mathbf{B}}{\partial t} = \nabla \times (\mathbf{v} \times \mathbf{B}) - \eta \nabla^2 \mathbf{B}. \quad (3.3.27)$$

In this equation the second term on the right hand side is the diffusion of the magnetic field, which we earlier encountered in the the energy equation as the Ohmic heating term in Eq. (3.3.24). In the induction equation his term is *always* negative and destroys the magnetic field. The first term on the right hand side represents the advection of magnetic field and the Lorentz force, this term can be negative as well as positive.

In rotating planets with a liquid inner core, the first term on the right hand side can be much stronger than the diffusion term and because of this could give gives rise to a global magnetic field. This also holds for the convective layer of the Sun. Here the magnetic fields are produced, which we later see the effects of at the Solar surface when they emerge.

Magnetic diffusion

Now that we have introduced the induction equation we quickly look back to the previous section where we mention that Ohmic diffusion follows self- consistently from the induction equation. Taking the time derivative of the magnetic energy, $e_B = B^2/(2\mu_0)$, leads to

$$\frac{1}{2\mu_0} \frac{\partial B^2}{\partial t} = \frac{1}{\mu_0} \mathbf{B} \cdot \frac{\partial \mathbf{B}}{\partial t}. \quad (3.3.28)$$

We can now insert the induction equation for the time derivative of the magnetic field. Then using a vector identity ² and Ampère's law, Eq. (3.1.7), to find

$$\frac{\partial e_B}{\partial t} = \frac{1}{\mu_0} \mathbf{u} \cdot (\mathbf{B} \times \mathbf{j}) - \eta \mu_0 j^2. \quad (3.3.29)$$

In this a change in magnetic energy, can occur through the action of the Lorentz force, which can be both positive or negative, which is the first therm on the right side. The second term on the right side changes the magnetic energy through the diffusion of magnetic field. The energy lost by the magnetic field adds to the thermal energy in our case. In a less simplified case this energy also goes into particle acceleration.

² $\nabla \cdot (\mathbf{a} \times \mathbf{b}) = \mathbf{b} \cdot (\nabla \times \mathbf{a}) - \mathbf{a} \cdot (\nabla \times \mathbf{b})$

3.4 Vector Potential

Instead of using \mathbf{B} in the MHD equations we can also write the equations as a function of the vector potential \mathbf{A} instead. They relate through

$$\mathbf{A} = \nabla \times \mathbf{B}. \quad (3.4.1)$$

The requirement of a divergent free magnetic field is automatically satisfied since the divergence of a curl is always 0. This is a strong motivation to use the vector potential instead of the magnetic field, as one does not have to worry about violating the solenoidality of the field. Then Ampère's law, Eq. (3.1.7) can be written as

$$\nabla \times \mathbf{B} = \nabla \times (\nabla \times \mathbf{A}) = \nabla(\nabla \cdot \mathbf{A}) - \nabla^2 \mathbf{A} = \mu_0 \mathbf{j}. \quad (3.4.2)$$

We can add any function to \mathbf{A} whose curl vanishes, without having any effect on \mathbf{B} . Taking the gradient of a scalar field satisfies this condition (the curl of a gradient is 0), such as

$$\mathbf{A} = \mathbf{A}_0 + \nabla \phi, \quad (3.4.3)$$

with \mathbf{A}_0 the original field and ϕ the scalar field.

We can exploit this to eliminate the divergence of \mathbf{A} by requiring

$$\nabla^2 \phi = -\nabla \cdot \mathbf{A}_0 \quad (3.4.4)$$

so that

$$\nabla \cdot \mathbf{A} = \nabla \cdot (\mathbf{A}_0 + \nabla \phi) = \nabla \cdot \mathbf{A}_0 + \nabla^2 \phi = 0. \quad (3.4.5)$$

This way Ampère's law reverts to

$$\nabla^2 \mathbf{A} = -\mu_0 \mathbf{j}. \quad (3.4.6)$$

On our simulation the gauge is chosen as $\phi = 0$, also known as the Weyl gauge.

3.5 Ordering of plasma along the magnetic field.

The use of field-lines to visualize and understand the magnetic field is an often employed tool, and as such it is worthwhile to explore the physical significance of this concept of magnetic field-lines. This is discussed in more detail by Longcope (2005).

The existence of a magnetic field limits a charged particle's freedom of movement. The Lorentz force on a charged particle in the presence of magnetic field is $\mathbf{F} = q(\mathbf{v} \times \mathbf{B})$. Along the direction of the field the particle is free to move, but its perpendicular velocity is constantly deflected in the direction perpendicular to $\hat{\mathbf{v}}$ and $\hat{\mathbf{B}}$. Therefore this force causes the particle to gyrate around a hypothetical line.

This effect severely limits the mean free path perpendicular to the magnetic field, and effectively quenches the thermal conduction in that direction. This results in neighbouring volumes of plasma to be thermally isolated from each other, if they are not connected by the magnetic field. This effect lies behind the strand-like structure of coronal loops. Any heating event will only heat the plasma through thermal conduction along the direction

of the magnetic field. Or in other words, any heating event will predominately heat the plasma contained within the bundle of field-lines in which this heating event took place. The increase of temperature also increases the radiate losses of the heated plasma, which then can be observed. There is still a unsettled debate on the thickness of these strands, and whether beyond the spatial resolution of our instruments these strands are made up from even thinner strands.

3.6 Poynting flux

Magnetic energy can be transported. This is expressed by the Poynting flux,

$$\mathbf{S} = \frac{1}{\mu_0} \mathbf{E} \times \mathbf{B}, \quad (3.6.1)$$

which has the units Wm^{-2} . Using Ohm's law, Eq. (3.2.5), to replace \mathbf{E} we get

$$\mathbf{S} = \eta \mathbf{j} \times \mathbf{B} - \frac{1}{\mu_0} (\mathbf{u} \times \mathbf{B}) \times \mathbf{B}. \quad (3.6.2)$$

Here the first term on the right hand side is recognisable as the Lorentz force which we encountered earlier in Sect. 3.3.2. The second part expresses the advection of magnetic energy through the motion of the plasma perpendicular to the magnetic field. Plasma can freely move in the direction of the magnetic field without changing the energy density of the magnetic field. Also worth noting is that the Poynting flux is always perpendicular to the magnetic field.

That last statement might make the interpretation of the Poynting flux unnecessary complicated. Imagining a small perturbation on the background magnetic field, a vector perpendicular to the perturbed magnetic field has a non-zero component in the direction of the unperturbed magnetic field. In case of sinusoidal perturbation the perpendicular components of the Poynting flux compared to the background field cancel out, and the component parallel to the background magnetic field remains. This way the Poynting flux *is* able to transport energy in the direction of the magnetic field.

3.7 The flow of energy in the model

To understand the flow of energy in our model we write down the full energy equation as

$$e = \frac{\rho u^2}{2} + \frac{p}{\gamma - 1} + \frac{B^2}{2\mu_0}. \quad (3.7.1)$$

The three terms on the right side represent respectively, the kinetic energy, the thermal energy, and the magnetic energy. Energy can not be created or destroyed, other than by the sinks and sources present in the equations.³ However, several processes can, and will, convert the different forms of energy into each other. The flows of energy, including the

³The non-conservative nature of our form of the MHD equations *does* create and destroy energy, but this is non-physical and very little compared to the physical sinks and sources, we will therefore ignore this in the discussion.

sinks and source, are shown in a comprehensive diagram in fig. 3.2.

Energy enters our domain at the bottom boundary. The driving of the magnetic field creates a Poynting flux into our domain, which increases the magnetic energy there. In the corona, this energy is predominantly converted into thermal energy through Ohmic dissipation. Another part of the magnetic energy can be used to accelerate the plasma by the Lorentz force, i.e. converting magnetic energy in to kinetic energy. Since the term $\nabla \times (\mathbf{u} \times \mathbf{B})$ can both be positive and negative this can also be used to induce magnetic energy from kinetic energy. A similar case hold for the connection between thermal energy and kinetic energy. Kinetic energy is lost through viscous forces, but (uncompensated) gradients in thermal pressure causes an acceleration of mass. In this case the Ohmic dissipation is somewhat of an exception for not having a compensating mechanism. Magnetic energy can be converted into thermal energy, but not directly back into magnetic energy. Thermal energy is transported downward into the dense chromosphere through conduction. In this high density region the radiative losses become a very efficient because of the ρ^2 dependence. Since the corona in our model is treated as optically thin, the radiation is not absorbed anywhere, and is thus lost from our model.

To summarize, energy is inserted in our domain through the Poynting flux and in the same way transported into the corona, there the energy is thermalized and transported back into the chromosphere where it is lost as radiation.

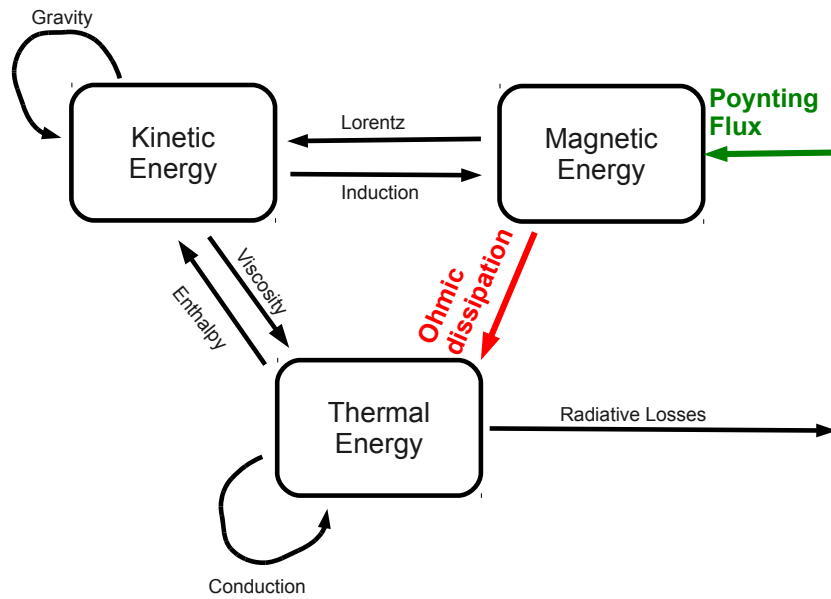


Figure 3.2: A schematic representation of the energy flows in our model. Energy enters our domain through the Poynting flux as a result of the granular diver at the bottom boundary, which stresses the magnetic field. The conversion of magnetic to kinetic energy is two way, meaning that the kinetic energy can be converted in to magnetic energy (through induction), but magnetic energy also into kinetic (through the Lorentz force). The same hold for the conversion between kinetic and thermal energy. The conversion of magnetic energy into thermal is a one way process, and the most important source of thermal energy in our model. The energy in our domain is only lost through radiation. Some processes can transport energy, but not convert it, gravity and conduction are indicated as an example of such a process.

4 Treatment of model corona

In this chapter we discuss the basic set-up of the model.

4.1 Model philosophy

The numerical models used in this work describe a part of the solar atmosphere in a box. At the bottom of the box the top of the photosphere is included, in which the magnetic field is anchored. Above the photosphere a roughly 5 Mm dense layer as the chromosphere before reaching the TR. In our model the chromosphere is mainly considered a mass reservoir, because in order to properly describe this region one has to include radiative transfer with NLTE effects included and a much higher resolution. When heat is deposited into the corona through some heating mechanism, the thermal conduction along the magnetic field transports the energy downward into the dense chromosphere where it is lost through radiation. Using the density and temperature, the synthetic emission can be used to compare the models with observables.

In the models in chapter 6, the heating takes place through the dissipation of braided magnetic fields. In these models the bottom boundary mimics the granular motion of the solar surface. This evolves the magnetic field and braids the coronal fields. Ohmic dissipation removes this stress by converting the non-potential magnetic energy into thermal energy, and in this way heats the corona.

The models in chapter 7 replace the heating as a result of the Ohmic dissipation with two other heating functions. These functions are based on parametrizations which were derived from other high resolution models of single strands of coronal loops. Since these functions do not require braiding, the granular driver is not used for these models.

4.2 Numerical scheme used by the Pencil Code

In order to solve the MHD equation we employ the Pencil Code (Brandenburg and Dobler 2002). This code is open source and available for free via Google-code via <http://pencil-code.nordita.org/>. Although primarily developed by Axel Brandenburg and Wolfgang Dobler, the list of contributors counts 40 people, at the moment of writing, and has not stopped growing. The modular set-up of the code allows a flexible use for a wide variety of physical problems.

The name is derived from the method of calculating the numerical domain. This is constructed by elongated arrays of data, so-called pencils, in the x -direction of the do-

main. This direction aligns with the physical storage of the data in the computer, which makes this storage very efficient. Additionally, this methods allows for easy parallelisation through MPI (Message Parsing Interface).

For the spatial derivatives we employ 6th order spatial derivatives. This requires the information of the three neighbouring grid points in order to calculate the derivative. The use of this high-order finite-difference scheme is a compromise between the numerical accuracy of spectral codes and time consumption of the calculation. In order to properly solve equations at the boundaries, an additional three grid points are needed outside of the physical domain. Through these three 'ghost cells' the boundary conditions are imposed on the model. The time evolution is calculated through a 3rd order Runge-Kutta scheme. This scheme divides the time step into several sub-timesteps before calculating the actual time step. A special $2N$ -version of this scheme is used, which only requires two version the variable-array in the computer memory rather than the four versions usually required.

Time step

To ensure numerical stability the time-step is limited by by the Courant time step. This condition ensures that any moving 'information' can not travel further than only a fraction of a grid point, which is a necessary condition for a numerical stable solution. The time-step is calculated by

$$\delta t = \min \left(c_{\delta t} \frac{\delta x_{\min}}{U_{\max}}, c_{\delta t, v} \frac{\delta x_{\min}^2}{D_{\max}}, c_{\delta t, s} \frac{1}{H_{\max}} \right) \quad (4.2.1)$$

where

$$\delta x_{\min} \equiv \min(\delta x, \delta y, \delta z) \quad (4.2.2)$$

and

$$\delta U_{\max} \equiv \max \left(|\mathbf{u}| + \sqrt{c_s^2 + v_A^2} \right), \quad (4.2.3)$$

where c_s and v_A are respectively the sound speed and Alfvén speed. Their combination $\sqrt{c_s^2 + v_A^2}$ is the speed of the fast-acoustic wave, the fastest wave possible in MHD. Further

$$D_{\max} \equiv \max \left(\nu, \gamma \frac{K}{c_p \rho}, \eta, D \right), \quad (4.2.4)$$

is defined by the different diffusion constants. Finally, H_{\max} relates to the viscosity and shock diffusion. The $c_{\delta t}$, $c_{\delta t, v}$ and $c_{\delta t, s}$ are weighting constants that can be chosen freely, but should be smaller than 1.

4.3 Implementation of the MHD equations

The full MHD equations as they are implemented in the code are different from the equations presented in the previous chapter. The values of both the density ρ and temperature T are in logarithmic form. In this form the MHD equations allow for a large range of values up to several orders of magnitude. This is important for the model where the density differs by about 10 orders of magnitude from top to bottom.

The magnetic field is replaced by the vector potential \mathbf{A} instead. This way Alfvén waves are better resolved and the calculation of the helicity, $\mathbf{A} \cdot \mathbf{B}$, straightforward. However, the main advantage for our application of the code is that we do not have to worry about the solenoidality of the magnetic field (i.e. $\nabla \cdot \mathbf{B} = 0$), as shown in Sect. 3.4.

In addition to the MHD equations several additional diffusion terms are included, such as the isotropic thermal condition (the last term in eq. (4.3.3)), for numerical stability.

The full set of equations as used by the code are

$$\frac{\partial \mathbf{u}}{\partial t} = -(\mathbf{u} \cdot \nabla) \mathbf{u} + \frac{1}{\rho} [-\nabla p + \mathbf{j} \times \mathbf{B} - \rho \mathbf{g}_\odot + 2\nu \nabla \otimes (\rho \mathbf{S})], \quad (4.3.1)$$

$$\frac{\partial \ln \rho}{\partial t} = -(\mathbf{u} \cdot \nabla) \ln \rho - \nabla \cdot \mathbf{u}, \quad (4.3.2)$$

$$\begin{aligned} \frac{\partial \ln T}{\partial t} = & -(\mathbf{u} \cdot \nabla) \ln T - (\gamma - 1) \nabla \cdot \mathbf{u} + \eta \mu_0 \mathbf{j}^2 + 2\rho \nu \mathbf{S} + \\ & \frac{\gamma}{c_p \rho T} \left[-\left(\frac{0.8\rho}{m_p}\right)^2 Q(T) + \nabla \cdot (K_0 T^{5/2} \mathbf{b}(\mathbf{b} \cdot \nabla T)) \right] + \\ & \frac{\gamma}{c_p \rho T} \left[\nabla \cdot (c_p \chi \rho \nabla T) + \nabla \cdot (c_{\text{iso}} |\nabla T| \nabla T) \right], \end{aligned} \quad (4.3.3)$$

$$\frac{\partial \mathbf{A}}{\partial t} = \mathbf{u} \times (\nabla \times \mathbf{A}) + \eta \nabla^2 \mathbf{A}. \quad (4.3.4)$$

The constants in here are

μ	$= 0.667$	-	Mean atomic weight,
\mathbf{g}_\odot	$= 274$	m s^{-2}	Surface gravity,
c_p	$\approx 312 \cdot 10^2$	$\text{J kg}^{-1} \text{K}^{-1}$	Heat capacity at constant pressure,
γ	$= c_p/c_v = 5/3$	-	Adiabatic index,
η	$= 10^{10}$	$\text{m}^2 \text{s}^{-1}$	Magnetic diffusion,
ν	$= 10^{10}$	$\text{m}^2 \text{s}^{-1}$	Viscosity,
χ	$= 5$	$\text{m}^2 \text{s}^{-1}$	Temperature diffusion,
K_0	$= 2 \cdot 10^{-11}$	$\text{kg m s}^{-3} \text{K}^{-1}$	Spitzer heat conduction,
m_p	$= 1.67 \cdot 10^{-27}$	kg	Proton mass.

There are additional diffusion algorithms in place for numerical stability, which are not included in the above set of equations. There is additional diffusion in regions that qualify as a shock, and a hyper diffusion scheme is present at the level of the 6th order derivative.

Coronal module

The module we use for our experiments provides us with the specific physics in the corona, and routines specific to our model set-up. The radiative losses or coronal plasma are described by the radiative loss function in Sect. 3.3.3. This is implemented in a linearly interpolated piecewise fashion over 38 points. Below 4000 K the radiative cooling is close to 0 to avoid over-cooling high density regions and reach negative temperatures.

The photospheric driver is similar to Gudiksen and Nordlund (2002, 2005b,a), who modelled this granular motion after observationally derived quantities. These include the velocity distribution and amplitude, and the granular lifetime. Also the vorticity of the granular motion is included. Just as in observations the regions with the strongest magnetic field have reduced granular velocities. This motion shuffles the foot points of the magnetic field through each other and entangles the field. In time, patches with opposing flux might meet and cancel, and the stronger concentrations of magnetic field will diffuse away through the random motion and magnetic diffusion. To cancel this we decreased the resistivity near the bottom to avoid too strong diffusion. At the same time we also add a small fraction of the initial magnetogram to the current one, so that it stays close to its initial active-region configuration. During the run the total magnetic flux through the bottom boundary is kept constant to counteract the magnetic cancellation.

4.4 Numerical model setup

The set-up of the models used in Sect. 7 and 6 are nearly identical. Each numerical experiment is done with a three dimensional rectangular box. This box is build from 128 grid points in each dimension. The x and y axis cover 51.2 Mm, and the z -axis 45 Mm. This brings the resolution of our model to 400 km in the horizontal direction and 352 km in the vertical directions.

4.4.1 Boundary conditions

The boundary conditions are imposed on the model through the use of ghost cells, the additional three grid points outside the physical domain.

For the horizontal directions the domain is assumed to be periodic.

The top boundary is closed, this means we allow for no energy or mass transport through the boundary. Preferably one would like an open top boundary, allowing for in- and out-flow of mass and energy. But this could also lead to unconstrained in- or outflows, because of the lack of information on the state of the corona outside of the box. For the magnetic field, the box is not closed, and is extrapolated according to a potential field extrapolation. This leads to some inconsistencies at the top boundary, such as mass flows along the field-lines that cannot continue. This leads to an enhancement of the currents at the top of the corona. Therefore one should be careful with the interpretation of the dynamics at the very top of the computational domain.

The bottom boundary is the driver of the dynamics in our model. Through this boundary new energy is inserted into the system by the driving at the bottom in the form of the Poynting flux. At the bottom of the box the field is extrapolated, but kept vertical with only a small deviation.

The driver at the bottom does include magnetic diffusion, which is a problem for the magnetic field there. This diffuses into a dipole in a short time if we use the same value of η as used in the coronal region. To avoid this problem we use a modified profile of the η value by decreasing it by two orders of magnitude near the bottom. This also decreases the heating rate through Ohmic dissipation near the bottom of the domain.

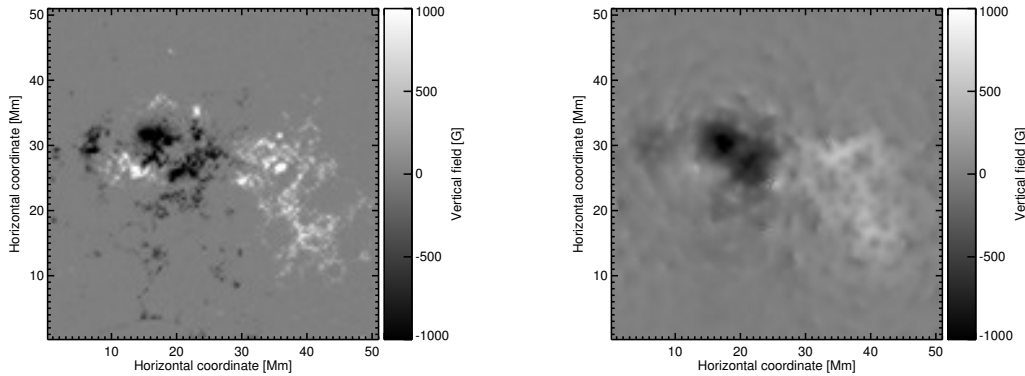


Figure 4.1: The vertical magnetic field at the bottom boundary. Left: The initial magnetic field at $t = 0$ seconds. Right: The vertical magnetic field after 45 minutes. The initial magnetogram is deformed through the granular motion imposed on the plasma at the bottom boundary. The basic structure of a dipole is conserved and small scale magnetic structures are seen throughout the plane.

The evolved magnetic field after 90 minutes can be seen in the right panel of Fig. 4.1. The disturbed field shows the patterns from the granular motion, but retains the dipolar nature of the initial magnetogram (Fig. 4.1, left panel). Despite the lower η the magnetic field is still fairly diffuse in comparison with the initial conditions, but will not diffuse much further than the state displayed now.

4.4.2 Initial conditions

Our initial conditions take the form of a hydrostatic corona with a tanh-profile for the temperature. Starting at 6000 K at the bottom, to 1.5 million Kelvin at the top. By solving for a hydrostatic solution, which includes gravity, we end up with a density in the corona of about 10^8 particles cm^{-3} , which roughly matches the density derived from observations (Priest 1982).

At the bottom we use a downscaled version of an observed active-region magnetogram, as shown in the left panel of Fig. 4.1. We include an initial magnetic field through a potential field extrapolation. Since a potential field is current-free and consequently force-free, this can be super imposed on the hydrostatic corona, without introducing a force imbalance (within the limits of the numerical precision).

When we turn on the model we damp all velocities for roughly 50 seconds after which we slowly remove the quenching. We do this to reduce the initial shock in the system that would appear as a turn-on effect.

Figure 4.2 shows a 3D rendering of one of our experiments at roughly 45 minutes into the simulation as an example. The colours in the vertical cut represent the temperature, where green is cool and red is hot $\log T[\text{K}] \approx 6$. The horizontal surface indicates the layer at which the plasma is $\log T[\text{K}] = 5$. The green and red shades on this iso-surface represent respectively the downward and upward magnetic field at that height. This iso-surface

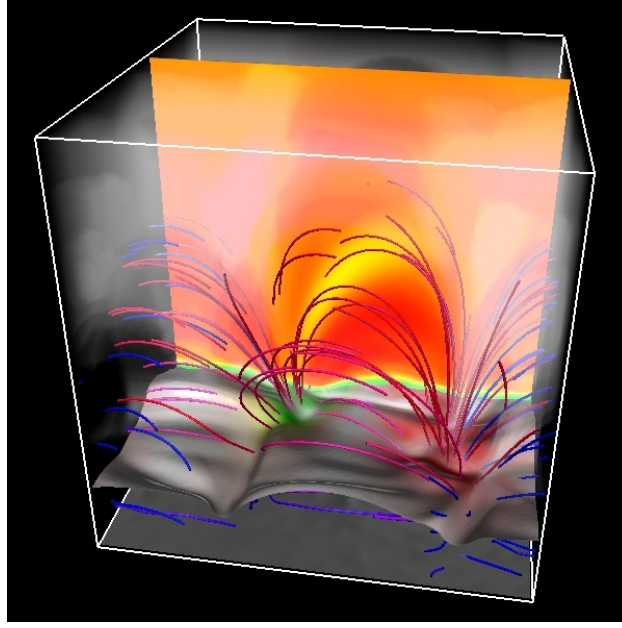


Figure 4.2: A 3D rendering of one the experiments described in this work. The colours in the vertical cut represent the temperature, where green is cool and red is hot. The iso-surface indicates the layer at which the plasma is $\log T[\text{K}]=5$. The green and red colours on this iso-surface represent the magnetic field at that height. This is also seen by the lines which trace the magnetic field. The mist represents the emission produced which would be observed by the 171 Å filter on SDO/AIA (Lemen et al. 2012) (see section 4.6). Image produced by VAPOR.

indicates the TR, the thin region that separates the chromosphere and corona. The lines in the box trace the magnetic field, and thus represent the magnetic field lines. Those that exit the box through one of the sides enter the domain on the other side as a result of the periodic boundaries. The mists represents the emission produced which would be observed by the 171 Å filter on SDO/AIA (Lemen et al. 2012) (see section 4.6)

4.5 Heating parametrizations

For our goal to investigate different heating mechanisms of the corona, we focus on two heating mechanisms in particular. Although a large amount of different models and suggestions are available, only a few offer the possibility to be directly applied to our model-framework. The two suggestions investigated, which are discussed in more detail in the following subsections, offer this possibility through parametrizations of the respective heating mechanisms. Both these parametrizations are derived from Reduced-MHD (RMHD) models. This branch of MHD allows high resolutions by reducing the equation to only consider the deviations from a background atmosphere.

4.5.1 Ohmic heating in the model

Heating in our model acts predominantly through Ohmic dissipation, as in Eq. (3.3.24). The value for the magnetic diffusivity in the Sun, as derived from transport theory, estimates this value to be of the order of $1 \text{ m}^2 \text{ s}^{-1}$. To estimate the typical length scales involved one can use the magnetic Reynolds number, which is an order-of-magnitude estimate of the ratio between the advective (inductive or creative) term in the induction equation, and the diffusive (destructive) term,

$$R_m = \frac{uL}{\eta}. \quad (4.5.1)$$

Where u is the typical velocity and L the typical length scale. The energy is dissipated on length scales of L where R_m is of the order 1. For the corona these values are far below our grid resolution. Formation of structures below grid resolution can and will lead to numerical errors, and therefore we increase the value of η to $10^{10} \text{ m}^2 \text{ s}^{-1}$ so that L is of the same order of magnitude as our grid size.

This leads to an overestimation of the size and thickness of the current sheets, and dissipation will become a significant loss of magnetic energy for even a small deviation from a potential field. We assume that locations where our model evolves strong currents also represents locations where in reality strong currents evolve, albeit at smaller scales.

Conservation of energy ensures that the *amount* of energy dissipated is equal to what would be dissipated in a more realistic case. Although in such case the evolution away from the potential field configuration might take longer, the *total* energy dissipated is the same. So it might be that more energy is stored in the magnetic field at smaller scales, the energy flux from Ohmic heating is of the same order in the model as in a more realistic case.

In conclusion, we do not resolve the actual current structures that heat the corona in the braiding model (as suggested by Parker, Sec. 2.3.2), but we will assume that the large current structures in our model represent an ensemble of many small current structures below our resolution limit. As such, we will consider Eq. (3.3.24) as a parametrisation of heating through field-line braiding.

4.5.2 Alfvénic heating

One of the heating mechanisms that we investigate is Alfvén wave turbulence, or, as we refer to it in the rest of the thesis, "Alfvénic heating". It is based on an earlier suggestion of current cascades (van Ballegooijen 1986), in which the random motions of the granular motions causes the free magnetic energy to form smaller and smaller structures until eventually dissipated.

A scaling law from RMHD models based on this principle is derived by van Ballegooijen et al. (2011). These numerical experiments model a single kilogauss magnetic flux tube with both ends in the photosphere. The background atmosphere in the tube includes the

effects of gravity and the expansion of the magnetic field in the lower corona. This is relevant for taking into account the reflection of the Alfvén waves. At the two bottom boundaries Alfvén waves are excited by foot-point motions. Through varying several model parameters such a scaling law can be derived,

$$Q_{\text{alf}} \approx 2.9 \cdot 10^{-4} \left(0.45 + \frac{33}{\tau_0} \right) \left(\frac{v_{\text{rms}}}{1.48 \text{ km s}^{-1}} \right)^{1.65} \left(\frac{L}{50 \text{ Mm}} \right)^{-0.92} \left(\frac{B}{50 \text{ G}} \right)^{0.55} \left[\frac{\text{W}}{\text{m}^{-3}} \right] \propto B^{0.55} L^{-0.92} v_{\text{rms}}^{1.65}, \quad (4.5.2)$$

where v_{rms} is the (root-mean-squared) velocity of the foot-point motions, L the length of the loop, and B the local magnetic field strength. τ_0 is a model depended parameter relevant to the driver. The constants originally included in the derived scaling law are dropped in the approximation here, since we are interested only in the dependencies on the different physical parameters.

4.5.3 MHD turbulence

The heating parametrization derived from Rappazzo et al. (2006) is based on the same philosophy as the models from Gudiksen and Nordlund (2002) and Bingert and Peter (2011), the field-line braiding of Parker (1972). This numerical experiment, however, reaches high resolution and extremely large Reynolds numbers, and can therefore resolve the small structures on which the energy is dissipated. The model set up is similar to the set up of the previously discussed model. This allows the derivation of a scaling law depending on the model parameters such as the loop length and driver velocity. The scaling law given by Rappazzo et al. (2006) for the energy flux

$$S \propto \ell_{\perp}^2 \rho v_A u_{\text{rms}}^2 \left(\frac{\ell_{\perp} v_A}{L u_{\text{rms}}} \right)^{(\alpha+1)/(\alpha+2)}, \quad (4.5.3)$$

where v_A is the Alfvén speed, u_{rms} the rms velocity at the bottom boundary, ℓ_{\perp} the typical perpendicular length scales, ρ is the local density, and L the magnetic loop length. α is a model dependent function of the loop parameters. The power, $(\alpha + 1)/(\alpha + 2)$ we approximate by 0.75, which is halfway the two possible limits. To get an estimate of the volumetric heating rate we divide the flux by the loop length and substitute v_A with $B(\mu_0 \rho)^{-1/2}$ to find the dependency on the magnetic field and density, this leads to

$$Q_{\text{turb}} \propto B^{1.75} L^{-1.75} \rho^{0.125} u_{\text{rms}}^{1.25} \ell_{\perp}^{2.75}, \quad (4.5.4)$$

where parameters are the same as above.

4.6 Synthetic emission

One test to evaluate the results of our models is to compare synthetic observations with real observables. The synthetic emission spectra from which we calculate our synthetic

observations are produced based on the CHIANTI atomic database (Dere et al. 1997). This database allows us to calculate the emission for a large amount atomic transitions in the plasma depending on temperature and density. This is important for comparison with the AIA/SDO observations, where one filter is sensitive to a relative large wavelength range. Therefore the emission detected is produced by a large sample of atoms and transition lines over wide range of temperatures. Although one "wavelength" of AIA is often interpreted as plasma at a certain temperature, it only means that the response function of that filter, has a maximum at that temperature. This does not mean that the emission observed comes exclusively from plasma at that temperature. Therefore great care has to be taken in the interpretation of the observations.

Integrating the synthesized emission in the box in one direction allows us to produce synthetic observations of the numerical model. This allows us to investigate the basic structure and evolution of the system as it would be observed by an actual observatory. In addition to investigating the emission structures, synthetic observations also allow us to derive synthetic Doppler images, by investigating the line-shift of the lines as a result of bulk flow of the plasma. Also here great care has to be taken in the interpretation of the Dopplergrams. As can be seen from the Eq. (3.3.22), the emission scales with the density squared. So small-scale high density regions of up- or downflowing plasma, have an unpropotional high influence on the observed flows. None-the-less, statistics of observed Doppler velocities as a function of formation temperature provides an important test for the validity of our models.

4.7 Mean atomic weight

We assume in our models a constant value for the mean atomic weight μ . This is however not the case in the real solar atmosphere, since the mean atomic weight is heavily depending on degree of ionization. A different values would result in a change in our physics. The importance of μ comes from its role in the equation of state,

$$p = \frac{R_{spec}}{\mu} \rho T \quad (4.7.1)$$

where $R_{spec} = \frac{k_B}{m_u} = 8314.4621 \frac{\text{J}}{\text{kg K}}$ is the gas constant. This equations shows that doubling μ results in half the photospheric pressure. In a hydrostatic equilibrium (assuming no magnetic field or a potential field) we know that

$$\nabla p = -g_z \rho, \quad (4.7.2)$$

where the pressure balances the gravitational force, g_z . Using this with the equation of state for an ideal gas gives

$$\frac{\partial \ln \rho}{\partial z} = -\frac{\partial \ln T}{\partial z} - \frac{g\mu}{R_{spec}T}. \quad (4.7.3)$$

We see that μ has an influence on both the temperature and density profile. In addition the density has an additional influence on the temperature through the radiative losses.

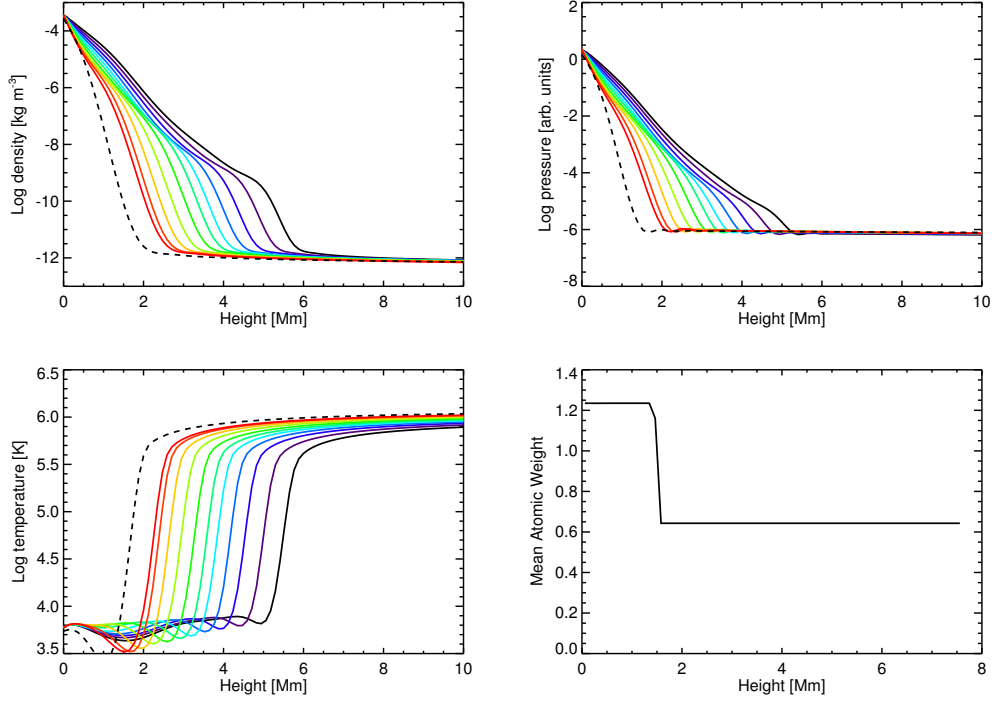


Figure 4.3: The first 3 plots show different profiles for (from left to right, from top to bottom) density, pressure, and temperature as a function of height for different values of μ . The colours from blue to red indicates an increasing mean atomic weight. The dashed line represents the results when μ is calculated when including temperature dependent ionization. The bottom right panel shows the values of μ for this temperature dependent ionization.

The mean atomic weight for a fully ionized is given by

$$\mu^{-1} = \sum_i \frac{X_i(1 + Z_i)}{\mu_i}. \quad (4.7.4)$$

Where X_i is the weight fraction of nuclei of type i and Z_i its charge and μ_i the atomic weight of the nuclei of type i . A fully ionized nuclei contributes 1 plus the number of electrons (i.e. its charge) to the number of particles. For a fully neutral gas this changes to:

$$\mu_0^{-1} = \sum_i \frac{X_i}{\mu_i}. \quad (4.7.5)$$

When we consider a gas with 90% H and 10% He, we have a μ that varies between 1.08 and 0.533. From equations 4.7.4 and 4.7.5 we can see that the contribution of the rare higher mass elements can easily be neglected.

Fig. 4.3 displays different profiles for a set of 1D atmospheric models, with the full energy equation (radiative losses, conduction) included, that evolved into a in hydrostatic equilibrium. What we see for an increase in the values of μ is that the density drops faster with height, and so steepening the transition region. The latter moves downward as a result of the shorter scale height of the density. The higher regions of the hydrostatic loop

model appear to remain un-influenced by the change in μ . Therefore the coronal temperature, the coronal density, and therefore also the coronal pressure do *not* depend on the choice of the mean atomic weight.

The value of the mean atomic weight is assumed to be constant over the computational domain. On the Sun, however, the mean atomic weight is a function of temperature. At lower temperatures, such as in the photosphere, hydrogen is predominantly neutral. Higher up in the corona, the temperatures are high enough so that hydrogen is fully ionized. The additional electrons from the ionization have a significant effect on the mean atomic weight. Since our interest lies in the coronal dynamics, and a different value for μ has nearly no effect on those, we choose to employ a constant values for μ throughout the domain. This is also in favour of not overcomplicating an already complicated problem.

4.8 Extraction of field-lines

In the models described in chapters 5 and 7, we have to extract the field-lines in the model. This is needed in order to calculate the heating rates according the parametrizations, Eqs. (4.5.2) and (4.5.4), which require the length of the loops. For this purpose we track from each gridpoint the field-lines that passes through it back to it's origins.

A field line, with space-curve $\mathbf{r}(l)$ satisfies the differential equation

$$\frac{d\mathbf{r}}{dl} = \frac{\mathbf{B}(\mathbf{r}(l))}{|\mathbf{B}(\mathbf{r}(l))|}. \quad (4.8.1)$$

Which is a property that we use in our routine to trace the field-lines. In small steps Δl we trace the direction of the magnetic field in both directions until it reaches the bottom boundary. If the field leaves the domain via the top, the full path, and thus actual length of the field line cannot be recovered. We assume the field line is much longer than any other field line in the domain.

After tracing the field-lines the information on the length of each field line at each gridpoint is stored. The values of these lengths are then used for the parametrizations of the heating in Eqs. (4.5.2) and (4.5.4). This procedure of tracing field-lines at each gridpoint is very time consuming, and thus not viable to do during the run of the numerical experiment. We therefore trace the magnetic field-lines prior to the start of the the numerical experiment, and assume that then during the run the lengths of the field-lines at the gridpoints do not change significantly.

This does not mean that the length of a field-lines itself cannot change, but only that the length of the field-lines passing through a specific gridpoint doesn't change. When for example a fieldline extends and moves slightly upward, the position where this line was earlier is now replaced with a new fieldline that will have roughly the same length as the other field line had before. Other sources of error in field-line lengths are reconnection events and foot-point shuffling. To reduce the error from these sources we turn off the granular driver our models with the parametrizations.

5 Heating along individual fieldlines

This chapter is based on the published paper: van Wettum et al. (2013)¹

5.1 Goal

The work presented in this chapter is a first step to investigate the feasibility of replacing the Ohmic heating with a parametrized heating. The goal of this experiment is to find out how the heating of these parametrization behave along individual field-lines as well as globally and compare this to the energy distributions through Ohmic dissipation. Furthermore we investigate whether these parametrized heating functions produce a different coronal loop in terms of density, temperature and emission.

5.2 Method

The equations provided in Sect. 4.5 allow us to calculate the distribution of a parametrized heating in a 3D MHD model. For this purpose use the results of the model by Bingert and Peter (2011). The set-up of this experiment is similar to the coronal model set-up we described earlier in detail in chapter 4.

We select one snapshot of the model when the simulation is, after roughly one hour of solar time, in a quasi steady state. One snapshot contains the relevant parameters, such as density and magnetic field strength, which allows us to calculate the relative heating rates according to the two parametrizations, Eqs. (4.5.2) and (4.5.3). The loop lengths are extracted by tracing the field-lines at each grid point back their origins or until the point where they leave the box through the top boundary, as is described in Sect. 4.8. This way we can calculate the length of each field line at each point in the box. For the field-lines that leave the box through the box top boundary we lack the information to calculate the length of the line and therefore assume a length much larger than any of the other field-lines, 1000. Mm.

Since our focus is on the different distributions of the heating, rather than the absolute values we ignore the different constants in front of the parametrizations.

5.2.1 Horizontal averages

Using the method described above we calculate the relative heating rates at each point in the physical domain of the model. The horizontally averaged heating rates for Ohmic

¹van Wettum, T., Bingert, S., & Peter, H. 2013, A& A, 554, A39

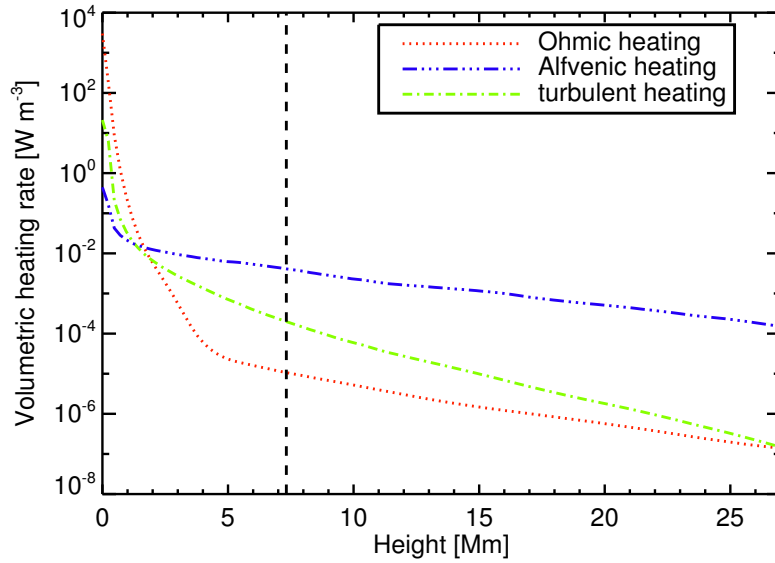


Figure 5.1: Horizontally averaged heating rates for different parametrizations. The dashed line indicates the average height of the base of the corona ($\log T[K]=5.5$). The Alfvénic and turbulent heating rates are in arbitrary units. See Sect. 5.2.1.

heating Eq. (3.3.24), Alfvénic heating Eqs. (4.5.2), and turbulent heating Eq. (4.5.3), are shown in Fig. 5.1. The heating rates associated with Alfvénic and Turbulent heating are plotted in this figure in arbitrary units. What we are interested in is how the heating rates change with height, not their absolute magnitude.

All three parametrisations drop roughly exponentially in the coronal part of the volume. For the Ohmic heating case, this is well known from previous studies. The fact that this exponential drop is common to all these three processes underlines the result (in part based on observations) that the energy input into the corona should be concentrated towards the footpoints (e.g. Aschwanden et al. 2007). While the (exponential) scale height for the drop of the heating rate is about 5 Mm for the Ohmic and Alfvénic heating, it is only 3 Mm for the turbulent heating. Thus the turbulent heating drops slightly faster than the two other mechanisms.

This common exponential drop for the three mechanisms is interesting because different (1D loop) models made different assumptions about the spatial distribution. While many models have assumed this exponentially dropping heat input (e.g. Serio et al. 1981; Müller et al. 2003), there are also numerous models that assume a spatially constant heating rate (e.g. Patsourakos and Klimchuk 2006; Klimchuk 2006).

Based on the horizontal averages alone as shown in Fig. 5.1, one cannot conclude that the distribution of the heat input along each magnetic field line is non-constant, but drops with height. Since the heating rates depend inversely on the loop length, it could be the result of stronger heating along the short field lines in the lower regions, even if the heating rate along each individual field line is constant. In the following we investigate individual field lines to determine if the drop of the horizontally averaged heating rate is because the heating drops with height for each field line or because longer field lines are heated less.

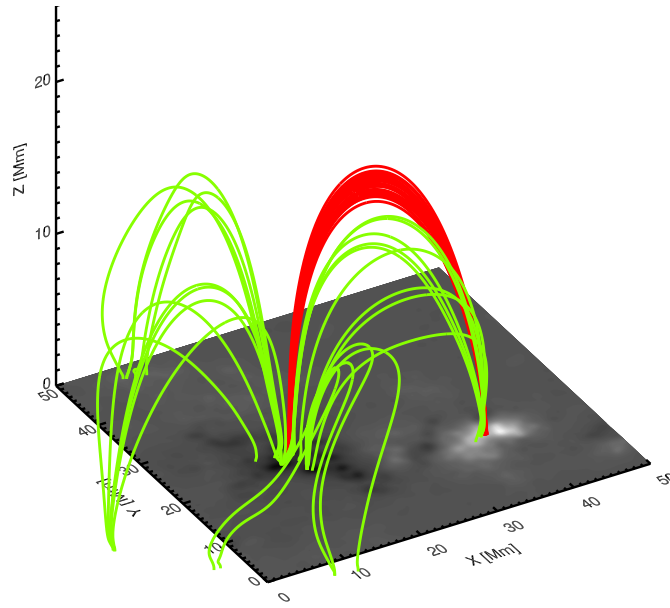


Figure 5.2: Three-dimensional illustration of selected field-lines for this investigation. The red lines belong to the bright loop selection, and the green ones to selection of the random set of field-lines. The grey-scale image shows the magnetogram at the bottom boundary of the simulation (which is based on observations).

5.2.2 Heating along individual field-lines

For the investigation of the heating along the individual field-lines we made several selections of field-lines and calculated the heating rates for each parametrization along each of them. We will discuss and further investigate two of these selections below.

Selection of loops

The first selection of field-lines was based on a bright loop in the synthetic emission in the model by (Bingert and Peter 2011). This is done by selecting only the denser and hottest field-lines in the corona. These field-lines have lengths between 45 and 50 Mm, a maximum temperature of more than $\log T[\text{K}] = 6.15$, and a minimum density of more than $10^{8.5}$ particles per cm^3 . This leads to the selection of the field-lines, indicated with red, in Fig. 5.2. Since this selection of field-lines is associated with the bright loop in emission we refer to it as the 'bright loop'.

The second selection is a more randomized selection of field-lines with looser constraints. Now the field-lines are no constrained to central region and the maximum-temperature requirement is loosened a bit to $\log T[\text{K}] = 6.05$. This more randomized selection acts as an additional check to see whether the results we get from the bright loops selection also hold for other field-lines. Due to its more randomized nature we refer to this selection as the 'random set'.

For each set we investigate the heating rates along a randomly selected subset of 25 loops to avoid cluttering the figures.

Bright loop

The heating rates along the bright loop are shown in the 3 panels in Fig. 5.5. From top to bottom, shown are the heating rates according to the different parametrizations of Ohmic, Alfvénic, and turbulent heating. We plot this as a function of the arc length along the field line, where the length of each field line is normalized to unity. The field-lines in the set differ in length by 10% at most. Furthermore, for the Alfvénic and turbulent heating the heating rates are normalized in respect to the heating just below the thermal transition region.

The most striking difference is that the Ohmic heating varies much more strongly than the Alfvénic and turbulent heating on small scales (smaller than a couple of % of the field-line length). This is because Ohmic heating depends on the spatial derivatives of the magnetic field (actually, the square thereof). Naturally, these show much stronger small-scale (but well-resolved) variations than the magnetic field itself. The original spatial variation of the Alfvénic and turbulent heating rate in the respective numerical models (van Ballegooijen et al. 2011; Rappazzo et al. 2008) also shows a stronger spatial variation. The heating rate becomes smooth only when the average behaviour of deriving the parametrisations as a function of B and other quantities is considered. Apart from the small-scale variation, the (smoothed) Ohmic heating and the turbulent heating along the magnetic field-lines are rather similar. In both cases the heating rate drops from the base of the corona (indicated in Fig. 5.1 by vertical dashed lines) to the loop apex by about a factor of 150 to 200. This is not too surprising because the Rappazzo et al. (2008) 3D reduced MHD model for the turbulent heating is, in principle, quite similar to our 3D MHD model for Ohmic heating (Bingert and Peter 2011). In both cases the foot points are smoothly driven at boundaries, which braids the magnetic field and induces currents. The reduced MHD model lacks the realistic set-up and the proper treatment of the energy equation to get the coronal pressure correct, but it can afford a much higher resolution in the numerical experiment and properly resolves the turbulent nature of the dissipation process. It is reassuring that these two models provide results for the heating rate that are not too different.

In contrast, the results for the Alfvénic heating following the van Ballegooijen et al. (2011) parametrisation show a different drop of the heating rate. From the coronal base to the top of the loop, the heating rate drops only by a factor of five to six (second panel of Fig. 5.3). Comparing the Alfvénic and turbulent parametrisations, Eqs. (4.5.2) and (4.5.3), clearly indicates that the magnetic field B makes the difference. The lengths L of the field-lines in the set are the same within 10%, the horizontal velocities at the footpoints v_{rms} due to the granulation cover only a small range, and the drop of the density ρ is not very important because of the comparably large barometric scale height (and the turbulent heating depends only weakly on ρ). However, the drop of the magnetic field from the coronal base to the loop apex by a factor of about 20 is mainly responsible for the large drop of the turbulent heating ($20^{1.75} \approx 190$) and the only small drop of the Alfvénic heating ($20^{0.55} \approx 5$). To highlight the differences in the spatial distribution of the three heating parametrisations, we plot the ratio of Ohmic to Alfvénic and turbulent heating in Fig. 5.4. This underlines that (on average) the turbulent heating is quite similar to the Ohmic heating. They both show a much stronger concentration towards the footpoints, which is mainly because of the different dependence on the magnetic field strength. The heating rates also

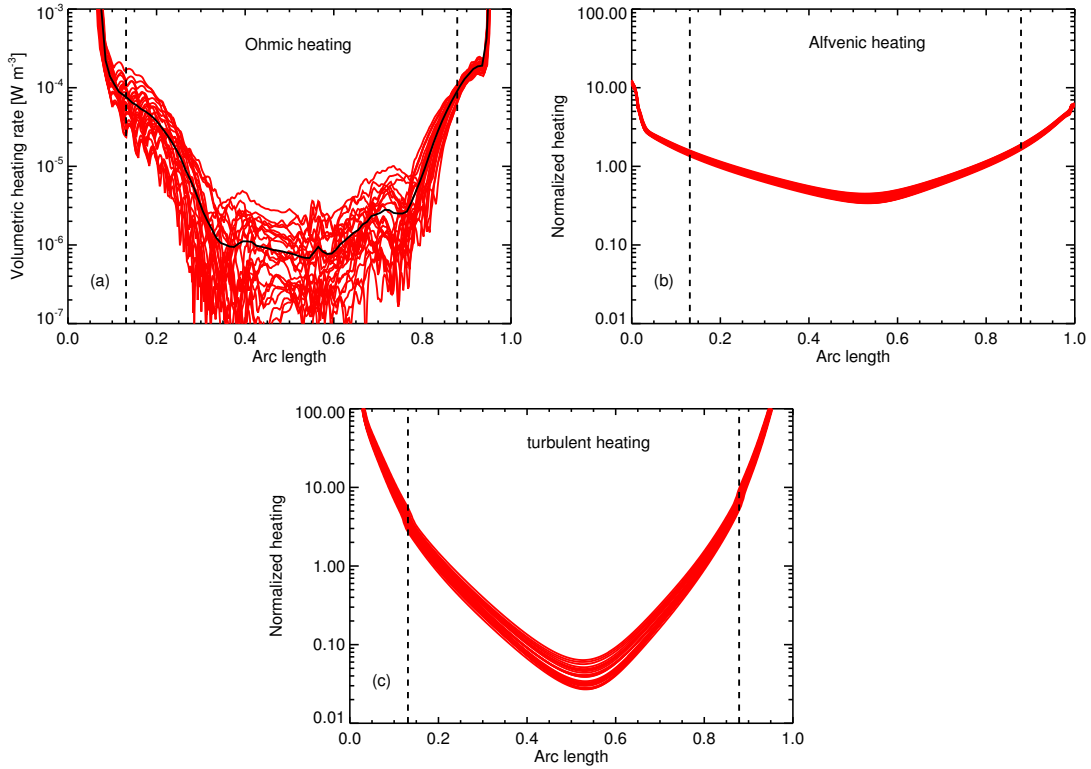


Figure 5.3: Volumetric heating rates along individual field-lines of the bright loop set, marked in red in Fig. 5.2. The lengths of the field-lines are normalized to unity. The thick black line in the top panel shows the average of the Ohmic heating for the selected field-lines. The Ohmic heating rates are averaged over five minutes to reduce the effect of transient events. The dashed lines indicate the average position of the coronal base at $\log T[\text{K}]=5.5$ for the selected field-lines. The Alfvénic and the turbulent heating are plotted normalized to the heat input just below the coronal base. All panels cover the heating rate over four orders of magnitude on the ordinate. See Sect. 5.2.2 and 5.2.2.

differ quite significantly below the base of the corona. This is not surprising because the parametrisations for the Alfvénic and turbulent heating are derived for the corona. So taking them seriously in the chromosphere would be overstretching these approximations. The 3D MHD model with the Ohmic heating shows a much stronger energy input in the chromosphere, which is because of the strong shearing of the magnetic field in the lower, denser part of the atmosphere, where plasma- β is no longer smaller than unity.

5.2.3 The “random set” of field-lines

The preceding discussion is for a quite special structure, namely, for field-lines associated with a bright loop. As a sort of blind test we now investigate a more random set of field-lines that are not associated with any particular coronal structures. This random set is plotted in green in Fig. 5.2 (see 5.2.2 for the definition). The volumetric heating rates and the ratio of the heating rates are plotted in Figs. 5.5 and 5.6

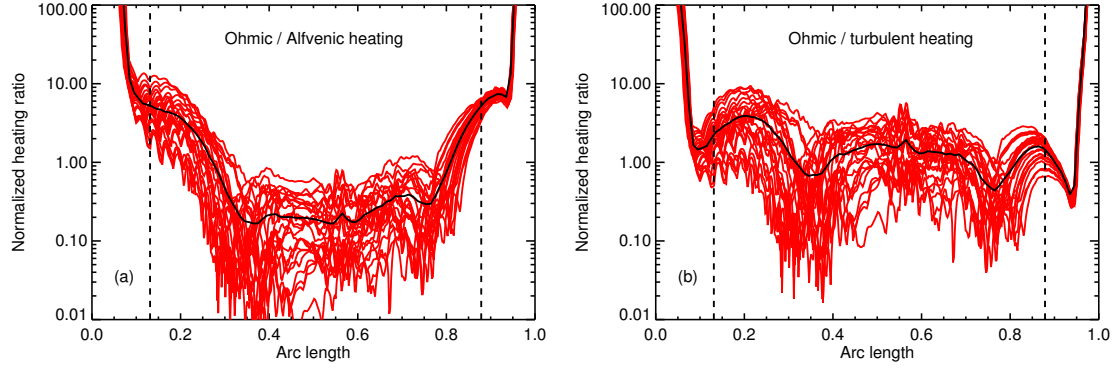


Figure 5.4: Normalized ratio of Ohmic heating to Alfvénic and turbulent heating (volumetric heating rates) for the field-lines of the bright loop set, marked in red in Fig. 5.2. The lengths of the field lines are normalized to unity. The thick black lines show the average of the ratios for the selected field-lines. The dashed lines indicate the average position of the coronal base at $\log T[\text{K}] = 5.5$ for the selected field-lines. Both panels show the ratio over a range of four orders of magnitude. See Sect. 5.2.2.

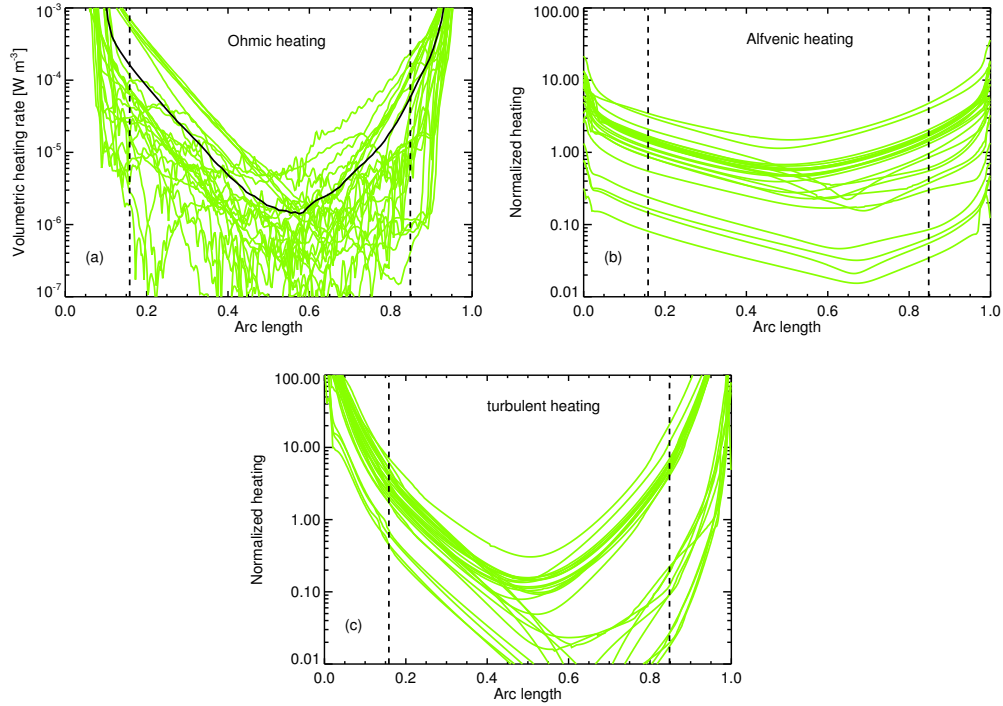


Figure 5.5: Similar to Fig. 5.3, but for the volumetric heating rates of the random set of field-lines marked in Fig. 5.2 as green lines. The asymmetry of the field line shapes shows up clearly, especially for turbulent heating. See Sect. 5.2.3.

Interestingly, this selection gives overall similar results as the bright loop set, albeit with a larger scatter. This is a result of greater variety of field-lines that sample different regions

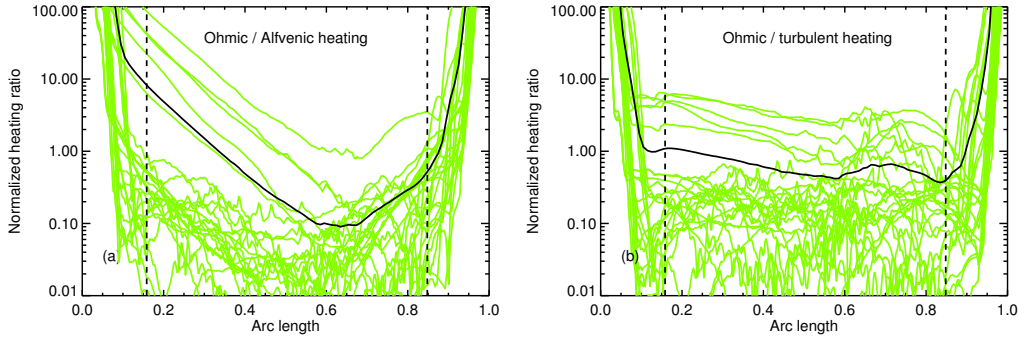


Figure 5.6: Similar to Fig. 5.4, but for the ratios of the heating rates of the random set of field-lines marked in Fig. 5.2 as green lines. See Sect. 5.2.3.

in the simulation box in different states. Despite the larger scatter, this clearly shows that the results outlined for the bright loop set can be generalized for the whole corona. This is not too surprising because in a low- β plasma the magnetic effects should be not too sensitive to the loading of the field-lines with plasma. Thus field-lines that are strongly loaded with hot plasma will show the same properties of the (magnetic) heating as other field-lines that are not loaded with plasma. Of course, there is still the correlation between heating and coronal density that determines which field-lines are loaded with how much plasma (for a discussion of the appearance of loops see e.g. Peter and Bingert 2012).

There is one pointed difference between the bright loop and the random set, though. The heating rates of the latter show stronger asymmetries between both sides of the loop, which are particularly strong for the turbulent heating parameterisation (middle panel of 5.5). This is because some of the field-lines in the random set are quite far from being semi-circular (cf. green lines in Fig. 5.2). These more strangely shaped field-lines are hosting the asymmetric heating mainly because of the field-strength asymmetry. Moreover, in the side where the field line does not reach very high into the corona, the density is higher and thus according to Eq. (4.5.3) the turbulent heating is stronger. This shows that the back-reaction of the heat input on the magnetic structure cannot be completely neglected (as noted in Sect. 5.2).

5.2.4 From field-lines to loop models

We have looked at the spatial distribution of three different parameterisations of coronal heating for two different selections of coronal field-lines. The volumetric heating rates of all parameterisations drop for all field-lines, and this drop is roughly exponential with height. The main difference is that the heat input for the Ohmic and turbulent case is much more concentrated towards the foot points than in the case of Alfvénic heating.

It is instructive to explore whether this difference in foot-point dominated and more uniform heating has a significant effect on the coronal emission (and the dynamics). Therefore, we now synthesize coronal emission from 1D loop models with a spatial distribution of the heat input similar to the average of the set of field-lines associated with the bright loop. Based on this, we can investigate to what extent one can distinguish the heating

parameterisations based on observable quantities. Obviously, this can only be a first step because in the end it has to be done within the framework of a 3D MHD model.

5.3 Details of 1D coronal models

The 1D loop model describes a semi-circular 1D coronal loop with a length of 45 Mm. Along the loop we solve the mass and momentum balance, including gravity. The energy balance includes heat conduction parallel to the magnetic field and optically thin radiative losses. The heating is exponentially dropping according to Eq. (5.4.1) with a scale height λ_i . Using the Pencil Code (Brandenburg and Dobler 2002) we solve these equations on a 2048 grid, closely following Peter et al. (2012). Starting from an initial condition with a prescribed temperature profile in hydrostatic equilibrium, we evolve the equations.

The results of the numerical experiments are shown in Fig. 5.7 for the parametrisation of the Ohmic heating ($\lambda_{\text{Ohm}}=1.8$ Mm) and in Fig. 5.8 for the Alfvénic heating ($\lambda_{\text{alf}}=6.8$ Mm). Temperature, density, and velocity are plotted as a space-time plot, i.e. as a function of arc length along the loop (normalized to the loop length) and time. In the case of Alfvénic heating (Fig. 5.8), the coronal loop reaches a stable static state after some 2000 s. For the discussion of this parametrisation in Sect. 5.4, we thus select a snapshot at $t=2500$ s, where the velocity is very close to zero, less than 3% of the sound speed. The situation is different for the Ohmic heating (Fig. 5.7). The strong concentration of the heating towards the footpoints evaporates chromospheric material, which then climbs up the loop towards the apex, where the heating rate is quite low. As the density increases, the radiative losses of the plasma increase and the plasma effectively cools. In a runaway process, a condensation forms because radiation becomes more efficient with decreasing temperature. Finally the condensation slides down one side of the loop. Because the heat input is kept constant, the whole procedure starts again. This process of loss of equilibrium is well known (e.g. Müller et al. 2003; Karpen et al. 2006; Peter et al. 2012), and the results we find for the onset of the condensation (depending on λ_i) are consistent with previous studies. From an inspection of Fig. 5.7, it is clear that there are long stretches of time between condensations wherein the loop is comparably stable at hot temperatures without any condensation present. During the time span shown in Fig. 5.7, this covers about 3000 s. This is long compared to the sound-crossing time, which is of the order of 400 s. Arguing that we want to catch the loop undergoing Ohmic heating in a phase when it is hot and free of condensation, we select a snapshot at $t=7500$ s (cf. Fig. 5.7) for the further analysis in Sect. 5.4. At this time the velocity along the loop is almost zero everywhere, so that we consider this a quasi-steady state. The 3D MHD model our study, based upon Bingert and Peter (2011), does not find such condensations in their synthesized emission. In that 3D model, the heat input along the loop is not symmetric, which is evident from the first panel of Fig. 5.3. Even comparably small deviations from a symmetric heating will lead to different pressures at the coronal base of the two loop legs, which will drive a siphon flow through the loop (e.g. Boris and Mariska 1982). To some extent, such a siphon flow will prevent strong condensations from forming because the flow carries away the plasma as soon as it starts to condense (Z. Mikić, priv. comm.). Thus we do not see a condensation in our 3D model. Furthermore, because condensations do not form, the loop apex can reach higher temperatures, as we see in the 3D model. We see the condensations form

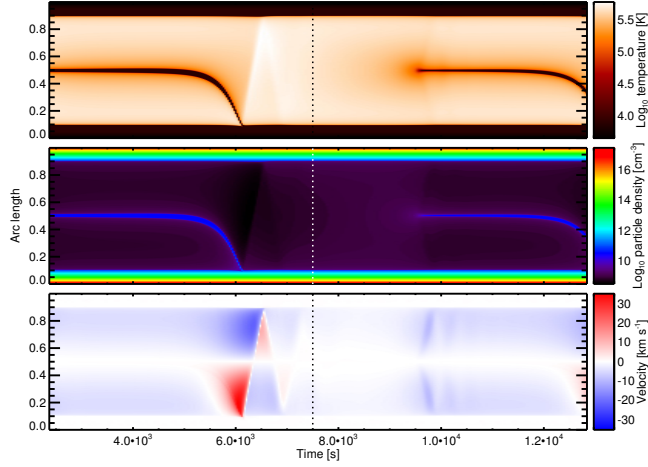


Figure 5.7: Variation of temperature, density, and velocity along the loop in the 1D model. Here we show the results for the parameterisation of Ohmic heating with a scale height of $\lambda_{\text{Ohm}} = 1.8$ Mm for an exponentially dropping heat input following Eq. (5.4.1). The arc length is normalized to the loop length of 45 Mm. The vertical dashed line indicates the time of the snapshot, which is further analysed in Sect. 5.4.

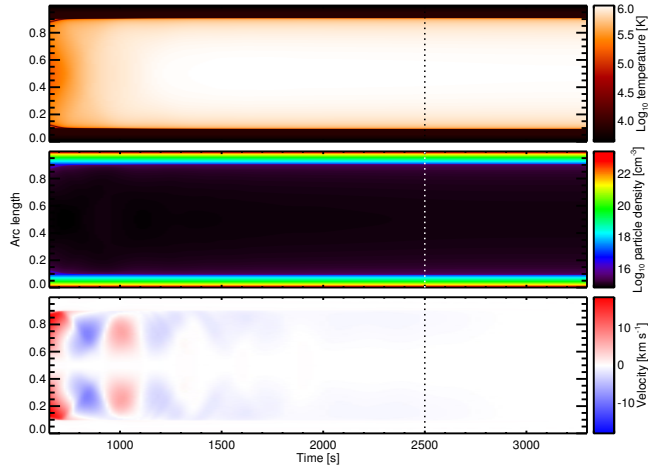


Figure 5.8: Same as Fig. 5.7, but for the case of Alfvénic heating with a scale height of $\lambda_{\text{alf}} = 6.8$ Mm.

in the more idealized 1D loop model with a perfectly symmetric heating rate. However, in view of the above discussion it is reasonable to concentrate on the phase between the condensations and to use the snapshot at $t = 7500$ s for the analysis in Sect. 5.4.

5.4 One-dimensional coronal loop models

In the following, we construct simple 1D models of a coronal loop with constant cross-section and a prescribed heating function. All quantities depend only on the arc length along the magnetic field line defining the loop. The velocity is parallel to the loop. Besides accounting for the conservation of mass and momentum (including gravity), we solve the energy equation. The latter accounts for optically thin radiative losses (following Cook et al. 1989) and heat conduction parallel to the magnetic field. This ensures that the coronal pressure is set self-consistently, which is pivotal if the resulting coronal emission radiated from the loop is to be synthesized, as we do here. The 1D models are run using the Pencil Code (Brandenburg and Dobler 2002) and follow the procedure of Peter et al. (2012).

For the purpose of comparing the synthesized emission from the 1D, loop we adopt the

average heating rate of the set of field-lines associated with the bright loop (red lines in Fig. 5.2, definition in Sect. 5.2.2, discussion in Sect. 5.2.2). This loop has a height of roughly 15 Mm and a foot-point distance of about 28 Mm. This corresponds to a roughly semi-circular shape with a length of about 45 Mm which we will use in our numerical 1D model.

The volumetric heating rate Q_i in the 1D model, which we will assume to fall off exponentially, is

$$Q_i = H_{0,i} \exp\left(-\frac{z}{\lambda_i}\right), \quad (5.4.1)$$

where z denotes the geometric height and $H_{0,i}$ is the heating rate at $z=0$. The scale height λ_i for the heating remains to be determined for the three heating parametrisations, here represented by the index i .

To determine the scale heights λ_i , we show in Fig. 5.9 the volumetric heating rates as a function of the geometric height z , including both loop legs, and not as a function of the arc length as before. We now fitted a simple exponential function in the form of Eq. (5.4.1), which provides values for the λ_i . For the fitting procedure we ignored all data points below the coronal base (at $\log T$ [K]=5.5, roughly at 3 Mm). These fits are over-plotted in Fig. 5.9 and the values for the λ_i are given. The exponential drop gives quite a good fit to the average variation. As suspected from the discussion in Sect. 5.2.2, Ohmic and turbulent heating show very similar results. This is why in the following we only compare the Ohmic and Alfvénic parametrisations. In the Ohmic case we adopt a scale height of $\lambda_{\text{Ohm}}=1.8$ Mm, for the Alfvénic case $\lambda_{\text{alf}}=6.8$ Mm. For the Ohmic case we use a heating rate at $z=0$ of about $H_{0,\text{Ohm}}\approx 3$ mW/m³ (see first panel of Fig. 5.9). We determine the value for $H_{0,\text{alf}}$ using the requirement that the heat input into the corona (i.e. integrated above the coronal base) has to be the same in both cases.

Because of the short scale height λ_{Ohm} , the loop for the parametrisation of the Ohmic heating is subject to a loss of equilibrium near the apex. This process is well documented in the literature (e.g. Müller et al. 2003; Karpen et al. 2006; Peter et al. 2012, and references therein). It leads to the episodic formation of condensations in the loop that eventually slide down into the photosphere. For the following discussion we thus investigate a snapshot in the comparably long time between two condensations (near $t\approx 7500$). The loop model of the Alfvénic heating with the longer scale height λ_{alf} reaches a static solution, which we then select for further analysis. For the times we analyse the two 1D models, the velocities along the loop are very close to zero, less than 3% of the sound speed, in both cases.

The temperature and density along the 1D model loops are plotted in Fig. 5.10 (top row). In the case of the Ohmic parametrisation (in red), the temperature is below the temperature at the apex as found in the 3D model. The condensation that formed earlier on is an effective sink for the energy, and thus preventing strong condensation, e.g., by a siphon flow induced by asymmetric heating, could allow the temperature to reach higher values near the apex. However, the focus of the following discussion is not to what extent the 1D models can reproduce the results of the 3D model, but if one can find observable differences for the two loop models with different heating parametrisations.

For the Ohmic and the Alfvénic heating we now calculate the coronal emission from the 1D loop model as it would be observed by the extreme UV imager on-board the Solar Dynamics Observatory, the Atmospheric Imaging Assembly (AIA, Lemen et al. 2012).

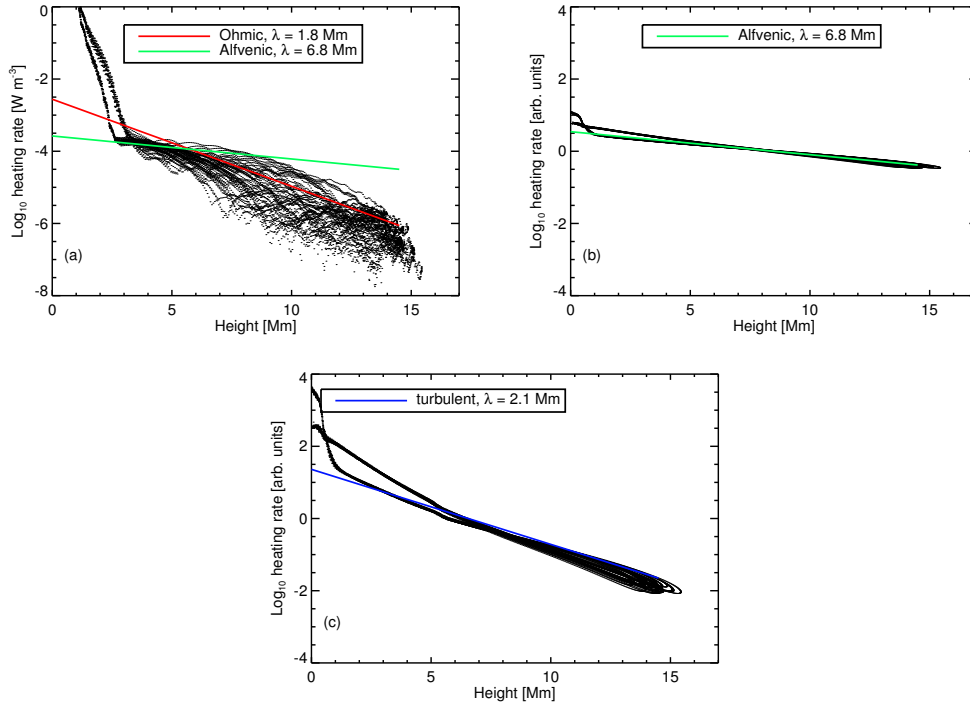


Figure 5.9: Volumetric heating rates over geometrical height for the bright loop (red in Fig. 5.2) for the three parametrisations. The black dots show the actual heating rates along the field-lines. The straight lines display the best exponential fit according to Eq. (5.4.1). The resulting scale height for the heating rate, λ_i , is listed. For comparison the exponential drop of the Alfvénic heating is over-plotted (in arbitrary units). See Sect. 5.4.

In particular, following the procedure of (Peter et al. 2012), we synthesize the emission for the 131 Å and 171 Å channels that are dominated by emission from ion Fe viii and ion Fe ix from plasma at temperatures of about 5.7 and 5.9 in $\log T$ [K] (Boerner et al. 2012). The resulting emission in these two pass bands for the two loop models is shown in the bottom panel of Fig. 5.10.

Overall, the (relative) spatial distribution of the 171 Å emission is quite similar for both, the Ohmic and the Alfvénic heating (Fig. 5.10 c,d). However, because of a lower density (and temperature), the absolute level of the emission is different. Still, when investigating actual observations to test which heating mechanism might be dominant, we would have to rely mostly on the relative distribution of the emission along the loop and not so much on the absolute level. Thus, at least in the case that we look at here, it would be hard to distinguish the heating mechanisms based on the 171 Å band alone.

A clearer difference is seen in the 131 Å channel, where Alfvénic heating has two distinct “horns” near the foot points of the loop but is significantly weaker in the centre of the loop, when compared to the case of Ohmic heating. This is somewhat unexpected because the Ohmic heating shows a much stronger concentration towards the footpoints. However, the emission we see does not directly reflect the spatial variation of the heat input but is a convolution of temperature and density, both of which are set by the heat input. Because of the higher apex temperature for the Alfvénic heating case, the spatial regions where

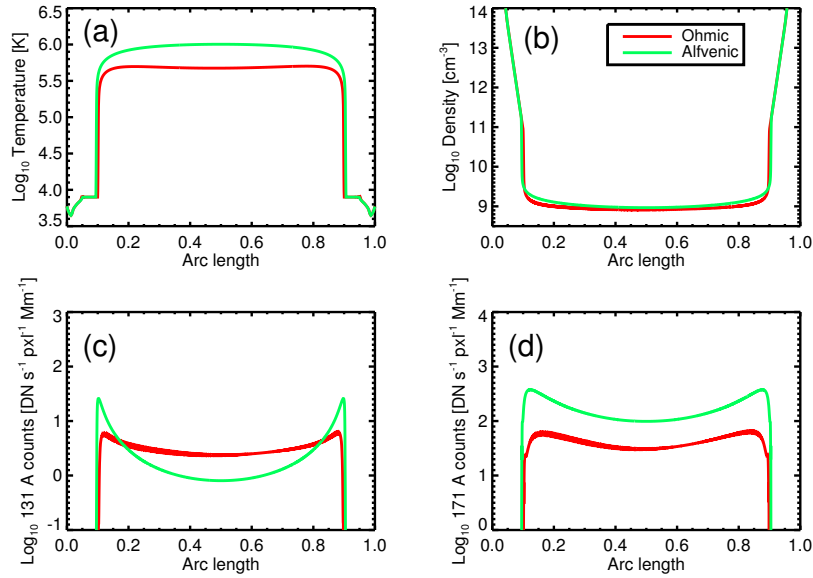


Figure 5.10: Variation along the loops in the 1D models for the parametrisation of the Ohmic (red) and Alfvénic heating (green). The arc length is normalized to the loop length of 45 Mm. The top panels show the temperature and the density, the velocities are very close to zero. The bottom panels show the coronal emission synthesized from the model as it would be observed with AIA in the 131 Å band (c) and the 171 Å band (d). See Sect. 5.4.

the (comparatively cool) 131 Å emission originates are narrower and shifted down when compared to the Ohmic case.

Depending on the band pass of coronal emission, two quite different heating mechanisms might produce similar or very different spatial distribution of the emission along the loop. In this example the 171 Å band is similar, the 131 Å band is different. For other 1D loop experiments with different total heat input, one can expect to find similar results, even though other channels might then be similar or different. So after all, observations of the coronal emission should hold the potential to distinguish between different spatial distributions of the heat input if one is not focusing on a single emission line or extreme UV bandpass alone.

5.5 Conclusions

In this paper we investigated differences and similarities of three mechanisms to heat the corona: Ohmic heating following braiding of magnetic field-lines by photospheric motions, the dissipation of Alfvén waves, and MHD turbulence. For our study we used the results of a self-consistent 3D MHD simulation (Bingert and Peter 2011). From this we calculated the Ohmic heating rate as resulting from that model, and heating rates that would be given by parametrisations for Alfvénic heating (van Ballegooijen et al. 2011), and turbulent heating (Rappazzo et al. 2008).

We find that all the horizontally averaged heating rates drop roughly exponentially with height. This is true for the average and also when investigating the heating rate along individual field-lines. We find a drop of the volumetric heating rate that is roughly exponential with height, along magnetic field-lines that are associated with a bright coronal loop in the 3D model, and along basically all other field-lines reaching into the corona. The Ohmic and the turbulent heating show roughly the same spatial distribution. This is not really surprising because the reduced MHD model for the turbulent heating is based upon Rappazzo et al. (2008), and is similar in principle to the full 3D MHD model (Bingert and Peter 2011). In both models the field-lines are braided and the non-linearity of the MHD equations drives the formation of small scales. This induces currents at small scales that are dissipated. While the full MHD model properly includes the energy equation, the reduced MHD models allow a much higher resolution. It is reassuring that these two models, using different approaches, give roughly the same result on the spatial distribution of the heating. In contrast, the Alfvénic heating (van Ballegooijen et al. 2011) shows a significantly smaller degree of concentration of the heating rate towards the foot points.

Using the spatial distribution of the heat input from the 3D models, we ran 1D loop models to make a first estimate whether one can distinguish the different mechanisms by the distribution of the coronal emission along the loop. For this we synthesized the emission to how it would be seen with AIA. Here we find that some bands (for our example at 171 Å) look quite similar, while others (here at 131 Å) show quite different variations along the loop.

The good news is that the different heating mechanisms will produce different observables (when considering enough bands). However, the bad news is that probably fiddling around with 1D models might be not sufficient because there are too many free parameters. Here we showed only results for one loop for two AIA bands, and the situation is quite different for other loops and/or other bands. Accounting for spatial complexity, new 3D models with a self-consistent treatment of the heat input based on driving in the photosphere will help in pinpointing the observational similarities and differences of the different heating mechanisms.

6 Coronal heat input and magnetic activity

6.1 Goal

The Sun is not unique for having a corona. Surveys show X-ray emission, a commonly used tracer for magnetic activity, across almost the whole of the main sequence (Güdel (2004)). Although some of these observations could also be explained by sources other than a corona, such as strong solar winds in OB-stars, this provides clear evidence that coronae exist on majority of main sequence stars. A more complete discussion on stars and magnetic activity is provided by Reiners (2012) and Güdel (2004).

There is ample evidence of a connection between chromospheric emission and X-ray emission of cool stars and their magnetic activity. A relation between the emission of Ca II K emission and C IV emission was found by Schrijver et al. (1989); Schrijver (1990). The Ca emission is another often used tracer for magnetic activity. The relation follows a power law as a function of the observed unsigned magnetic flux fB ,

$$F_{\text{Civ}} \propto \langle fB \rangle^{0.7}. \quad (6.1.1)$$

A similar power law for the X-ray luminosity was found by Pevtsov et al. (2003) and Saar (2001).

$$F_X \propto \Phi^\alpha, \quad (6.1.2)$$

where Φ denotes the magnetic flux and α takes the value of 1.15 for active stars and 0.95 for cool stars.

The investigation described in this chapter explores the effect of a different unsigned magnetic flux in the photosphere on the dynamics and observables of the corona and TR. We interpret this higher magnetic flux as if the host star would have a higher magnetic activity. In addition to this we briefly look at the effect of a different driver velocity. Or, to phrase it differently, we investigate the effect of a different Poynting flux into the corona. After synthesizing the emission we expect to find a relation between the magnetic field and coronal emission.

Run	$B_0[10^{13}]\hat{B}$	v_0 [km s ⁻¹]
Run 1.1	1.0	1
Run 1.2	1.0	2
Run 2.1	1.8	1
Run 2.2	1.8	2
Run 3	2.4	1
Run 4	4.0	1

Table 6.1: Overview of the setting of the six numerical experiments. These differences are the only differences between the models. B_0 relates to the total unsigned magnetic flux at the bottom boundary. The u_0 is the mean granular velocity of the driver.

6.2 Method

For this purpose have performed several numerical experiments with a nearly identical set-up of a corona in a box. The general set-up of the model is already discussed in chapter 4. For this experiment we use different amplitudes of the magnetic field at the bottom boundary to mimic a higher or lower magnetic activity. The threshold for the quenching of the granulation driver is increased or decreased accordingly to keep the same surface of the photosphere driving the magnetic foot points. In addition two experiments also had a different strength of the granular velocity driver at the bottom boundary. An overview of the different parameters used in the six numerical experiments are given in table 6.1. Each run starts from identical initial conditions with the exception of run 2.1, which is a continuation from run 2.2. These differences mentioned are the only differences between the different runs.

The heating of the corona is through the dissipation of currents, induced by the braided magnetic fields. In our model we use a threshold magnetic field strength at the bottom boundary above which the granular motion is quenched. This threshold has to be adapted with accordingly when increasing or decreasing the magnetic field at the photosphere, since the same surface area has to participate in the braiding to ensure a fair comparison.

6.3 Results

Most of the runs cover over one hour of solar time. Runs 1.1 and 1.2 encountered numerical problems which forced the simulations to terminate early. The experiments lasted fortunately long enough for the purpose of our investigation, but too short to investigate a possible observed oscillatory behaviour. Aside from this problem each model was able to produce a corona and TR.

As a test on whether the different runs are able to produce coronal structures similar to observations, we investigate the synthesized emission structures of the different runs as it would be detected by the 171 Å filter of the AIA instrument on SDO (Lemen et al. 2012). Pre-calculated tables based on the CHIANTI database (Dere et al. 1997) of the response functions of this instrument allow us to calculate the total emission at a gridpoint as a function of density and temperature. The results are displayed in Figs. 6.1 and 6.2. These

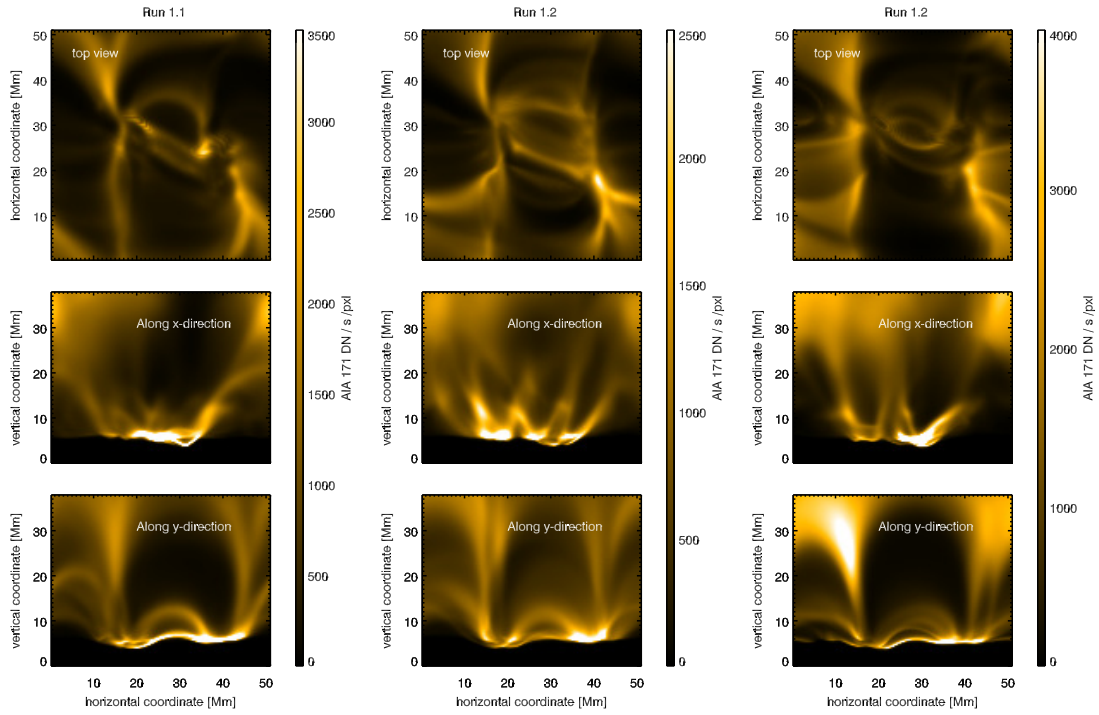


Figure 6.1: Synthetic observations for the AIA 171 Å filter for the (from left to right) runs 1.1, 1.2 and 2.1 in table 6.1. The response function of the AIA 171 Å filter peaks at $\log T[\text{K}] = 5.8$. The top panel shows the integrated intensities along the z -axis. The middle and bottom panel show the sideview from the box along respectively the x and y -axis. The intensity ranges differ per run for clarity.

figures show the synthesized coronal emission integrated along the major axes. The intensity ranges are scaled differently for each run for clarity. This can be excused since the emission scales with the density squared, a factor two difference in intensity is only a factor $\sqrt{2} = 1.4$ in density.

The figures we see that each model produces a loop dominated hot corona. The actual structures of these coronae are quite similar, which is expected for nearly identical magnetic field structures at the bottom. Each model contains a clear loop structure connecting the main two polarities in the centre. A more diffuse loop structure is found connecting the two polarities through the periodic side boundaries.

6.3.1 Heating in time

The different magnetic field strengths and heating distributions affect the dynamics and structure of the corona. We want to investigate how the heating rates of the numerical experiments differ, and how they behave as a function of time. The temporal variability is displayed in Fig. 6.3 in which the total Ohmic heating in the physical domain is plotted as a function of time. Run 2.1 is a continuation of run 2.2, and thus shown behind that run, all other runs start from $t = 0$.

The total Ohmic heating of the experiments with a stronger magnetic field are higher

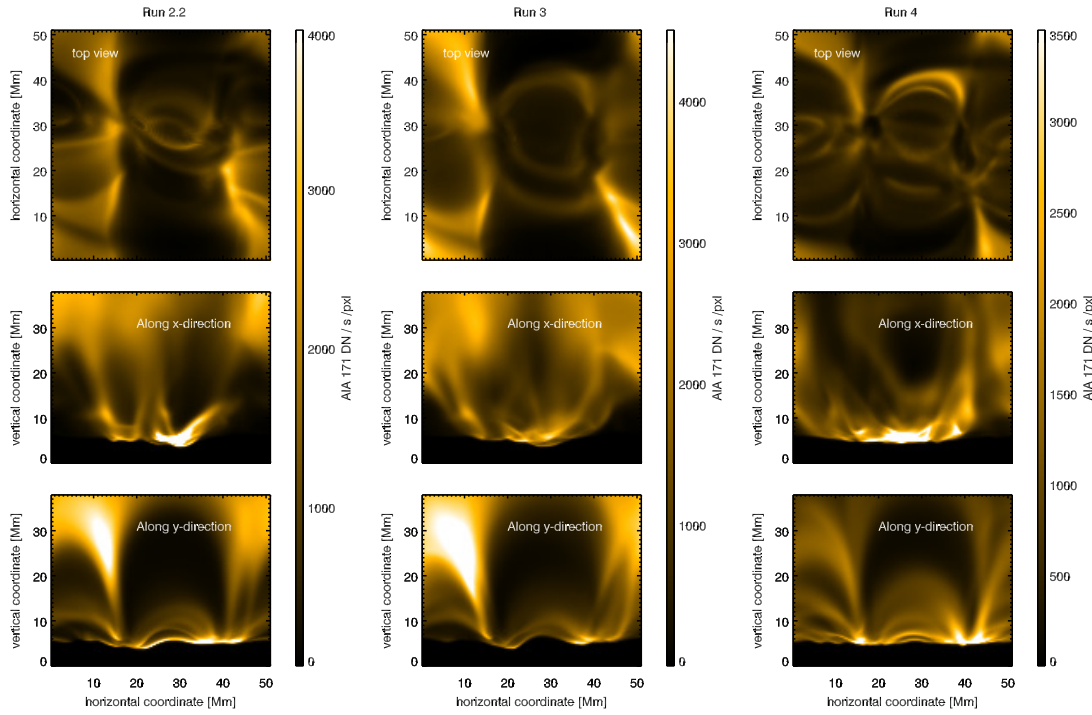


Figure 6.2: Similar to 6.1, but for the (from left to right) runs 2.2,3 and 4 in table 6.1.

than those with a weaker magnetic field. All runs start with a strong heating as a result of switching on the simulation. This initial heating is limited to only the lower few gridpoints of the box, and fades in roughly 20 minutes. At this point in the heating in most of the simulations reaches a plateau. An exception to this are runs 1.1 and 1.2. These appear to have a strong oscillatory behaviour of Ohmic heating in time. Whether this is truly oscillatory could not be determined, as the strong heating-induced dynamics caused numerical instabilities and the simulations could not advance further.

The symbols in Fig. 6.3 mark a sets of snapshots that we use for further investigation below. These snapshots are chosen at a time in which the simulations are relatively steady. For most runs these snapshots accurately represent the rest of the run, with an exception for those belonging to run 1.1 and 1.2, as there is no existing representative timespan due to the dynamic nature of these runs.

The Fig. 6.4 shows the temporal averaged heating of the selected snapshots versus the magnetic field strength at the bottom. Runs 1.2 and 2.2, which have a stronger velocity driver, are shifted slightly to the right for clarity. From this we see that in general the total Ohmic heating in the physical domain is higher for the experiments with a stronger magnetic field at the bottom. This seems, however, not to scale with the amplitude of the square of the magnetic field as one would expect from energy-considerations (magnetic energy scales with B^2), but with a linear relation instead.

This could be explained by looking at the Poynting flux in more detail, which is the flux of magnetic energy. The last term of Eq. (3.6.2) is a double cross product. The vertical

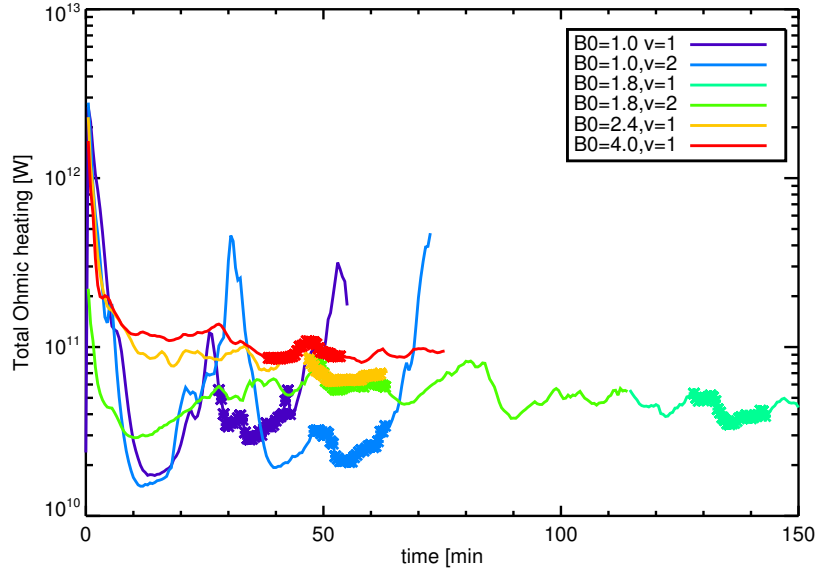


Figure 6.3: The integrated Ohmic heating in the physical domain as a function of time for the different runs. The marked points are a selection of snapshots use for further investigation.

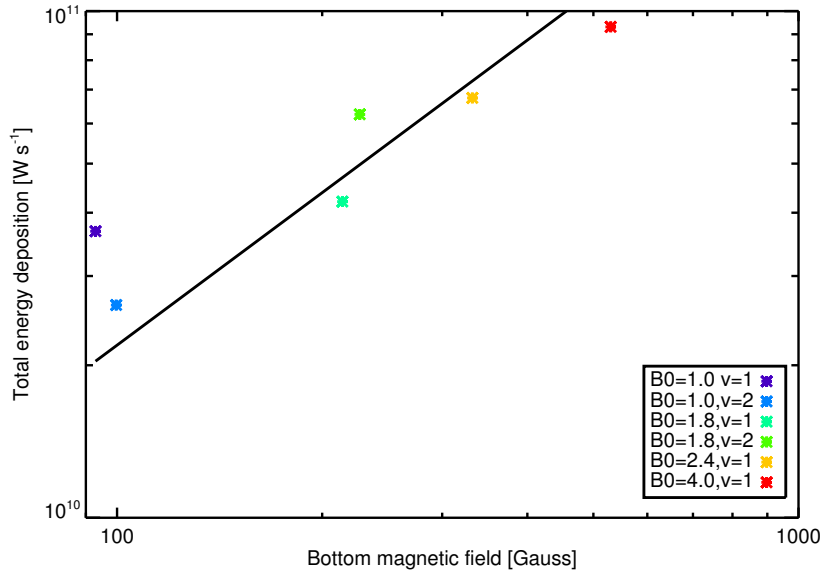


Figure 6.4: Time averaged heating as a function of the magnetic field strength at the bottom. The two runs, 1.2 and 2.2, with a higher diver velocity are shifted slightly to the right for clarity. The black line indicates a linear relation between the bottom magnetic field and the total heat deposited.

component can be rewritten, in a simplified way as,

$$S_z \propto (u_h \times B_v) \times B_h, \quad (6.3.1)$$

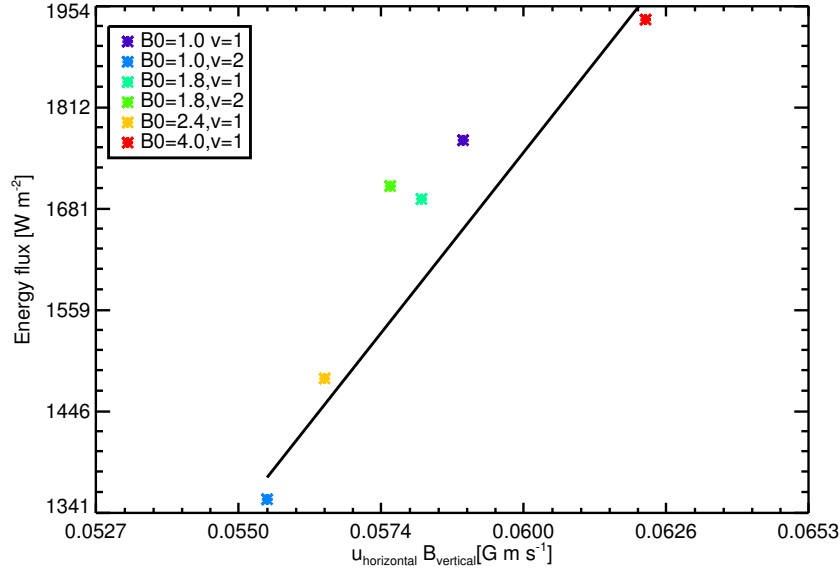


Figure 6.5: The averaged energy flux into the corona just below the Transition Region (roughly 4 Mm from the bottom) as a function of $u_h B_v$. The black line shows the relation $F_{\text{TR}} \approx (u_h B_v)^3$. Note that both axis are logarithmic scaled.

where the subscripts v and h denote the vertical and horizontal directions respectively. Since the magnetic field at the bottom boundary is predominantly vertical, doubling the magnetic field will yield a doubling in the vertical component, but no doubling in the horizontal. As such, the vertical magnetic energy flux scales linearly with B . Assuming that the total heat input directly relates to the coronal energy input, and thus the coronal emission, a close-to a linear relation between the magnetic flux at the surface and the X-ray emission would be expected, which is in fact observed (see Eq. (6.1.2)).

We investigate this suggestion by investigating the product of the vertical magnetic field and the horizontal velocity field at 3.9 Mm with the total heating above that region, averaged over the earlier marked snapshots. This height is just below transition region and just above the region of the step in the magnetic diffusion η . This is displayed in the bottom panel of Fig. 6.5. Although the points do scale with the magnetic field strength at the bottom boundary, we can find good fit between this proxy of the Poynting flux at the bottom of the TR and the total energy deposition above that layer. We find a good fit for $(u_h B_v)^3$. Higher up this relation breaks down as the horizontal magnetic field and vertical flows become more dominant.

One caveat of the plots of Fig. 6.3 is that the averages are dominated by the heating in the lower regions of the physical domain, due to the exponential drop with height. This can be seen in Fig. 6.6, where the horizontally and temporally averaged heating rates are shown over height.

The peak around 3 Mm is an effect of the η -step function described in Sec. 4.5.1, which reduces the magnetic diffusion, and thus the Ohmic heating, by a factor 100 below that height. The heating rates in the corona do not directly line up with the magnetic field

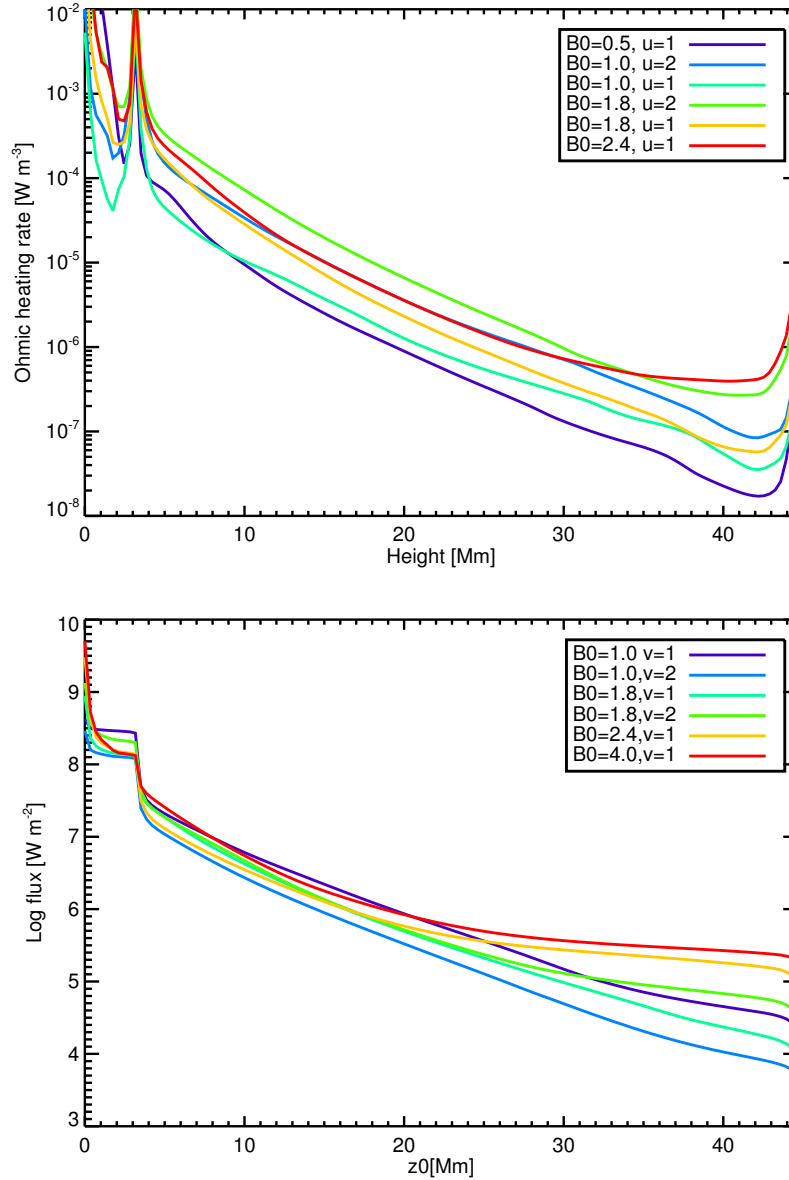


Figure 6.6: *Top*: The horizontally and temporally averaged Ohmic heating over height for the different runs. The peak around 3 Mm is a result of the η -step function at that height. The heating rates do not differ from each other by more than a factor 10. *Bottom*: The horizontally and temporally averaged Ohmic heating-flux as a function of height for the different runs.

strengths. The slope of the heating rates are all roughly the same. The increasing slope at the top is an artefact of the closed boundary, that causes the formation of strong currents there. It can however be argued that, although the formation of the currents there is a numerical artefact, the energy deposited originates from the driver at the bottom.

When considering (a proxy of) the flux in the form of

$$F(z) = \int_z^\infty H(z') dz', \quad (6.3.2)$$

with F denoting the flux, and H the (horizontally averaged) volumetric heating rate. The result of this is shown in the bottom panel of Fig. 6.6. With this proxy we find a good match with the field strengths and driver velocities starting from roughly 25 Mm and upwards, with an exception for run 1.1.

When moving upwards into the corona, the heating rates stop to line up with the magnetic field strength at the bottom. The heating of plasma above a certain temperature is investigated in the top panel of Fig. 6.5. In here we see the total averaged heating as a function of the magnetic field at the bottom (with run 1.2 and 2.2 shifted slightly to the left again), for different temperature thresholds of the coronal plasma. It shows no clear relation between the magnetic field strength and the total heating for any of the thresholds.

6.3.2 Doppler shifts

Stronger or weaker heating events can have an influence on the velocity field throughout the corona.

The Doppler shifts of synthesized emission lines for the selected snapshots and their average are shown in Fig 6.7 as a function of the formation temperature. The coloured lines are for the individual snapshot, and the black line indicates the average of those. The vertical black error bars represent the 0.1σ spread of the Doppler shifts. The calculated Doppler shifts for the cool lines, emission lines with low formation temperatures, are more static in time, whereas the hotter lines vary more strongly in time. Of all six runs, run 2.2 and 3 have the most solar-like pattern of Doppler shifts.

A recent study by Linsky et al. (2012a,b) investigated the relation between Dopplershifts as a function of formation temperature and rotation period of rapidly rotating Solar-like stars. Fast rotation periods are coupled with stronger magnetic fields as a result of the stronger dynamo action. It was found that for more rapid rotating stars the red-shifts of the C IV and Si IV lines increased. This is displayed in Linsky et al. (2012b) their Fig. 6, which shows stronger red shifts for emission lines formed at high temperatures for active stars. Less active /slower rotating stars show a more Solar like pattern where these emission lines are more blue-shift. In the context of these findings, our results are consistent with these findings.

6.3.3 Flux flux relation

We use the total emission of the different lines in order to compare our results with the flux-flux relations mentioned earlier in Sect. 6.1. Since the C IV emissions scales with the magnetic flux, and the X-ray flux in turn also scales with the magnetic field strength, we expect a relation between the C IV emission and X-ray flux. Although we don't

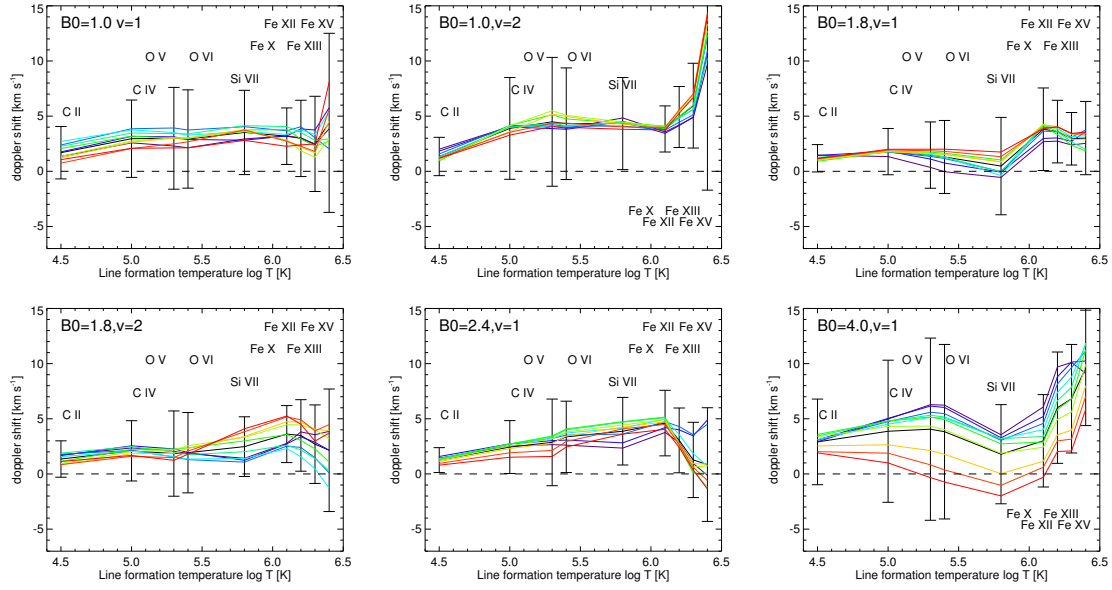


Figure 6.7: Doppler shifts for the different runs. The different colours represent the different snapshots, and the black line the average. The error bars indicate the spread of observed Doppler shifts.

have synthesized emission lines in the range of X-rays, we assume that the lines with the highest formation temperature are a good approximation for it. In general Fe XV formed at roughly 3 MK shares many characteristics with the X-ray emission on the Sun. When we combine Eqs. 6.1.1 and 6.1.2, assuming α is 0.95, we end up with an expected relation of

$$F_X \propto F_{C\,IV}^{0.98/0.7} \approx F_{C\,IV}^{1.4}. \quad (6.3.3)$$

This relation is plotted by a black line in Fig. 6.8.

In this figure the symbols represent the mean C IV emission per snapshot compared to the mean emission of the other emission lines in that snapshot. The emission from the different lines are all normalized in respect to the maximum emission of that line and then shifted for clarity in order of their formation temperature. The respective lines, indicated with different colour and sign, from bottom to top represent the emission from: C II, O V, O VI, Si VII, Fe X, Fe XII, Fe XIII, Fe XV. This order (from bottom to top) also follow the formation temperature of these lines from bottom, around $\log T[K] = 4.5$, to top, $\log T[K] = 6.4$, for Fe XV.

Especially for the emission lines coming for the highest formation temperatures the peak of the emission distribution does not coincide exactly with the formation temperature. This is the result of the ρ^2 dependence of the emission, and thus the slightly cooler, but denser, plasma emits more photons in that wavelength range than the hotter plasma. This means that the emission coming from, i.e. Fe XV, does not represent the 3 MK plasma, but a lower temperature plasma which is denser.

The bottom few lines follow a relation close to linear since the formation temperatures are very close to each other, and thus the lines probe the same region of the simulation. The emission lines at the top of the plot, coming from hot plasma, loosely follow a power law relation with the C IV emission as from the derived relation in Eq. (6.3.3).

Maybe more interesting that the lines of Si VII, Fe X, and Fe XII seem to be independent of the C IV emission. It is unknown whether a similar trend, or the lack thereof, is seen in observations. This motivates new observations to explore this range T in the coronae.

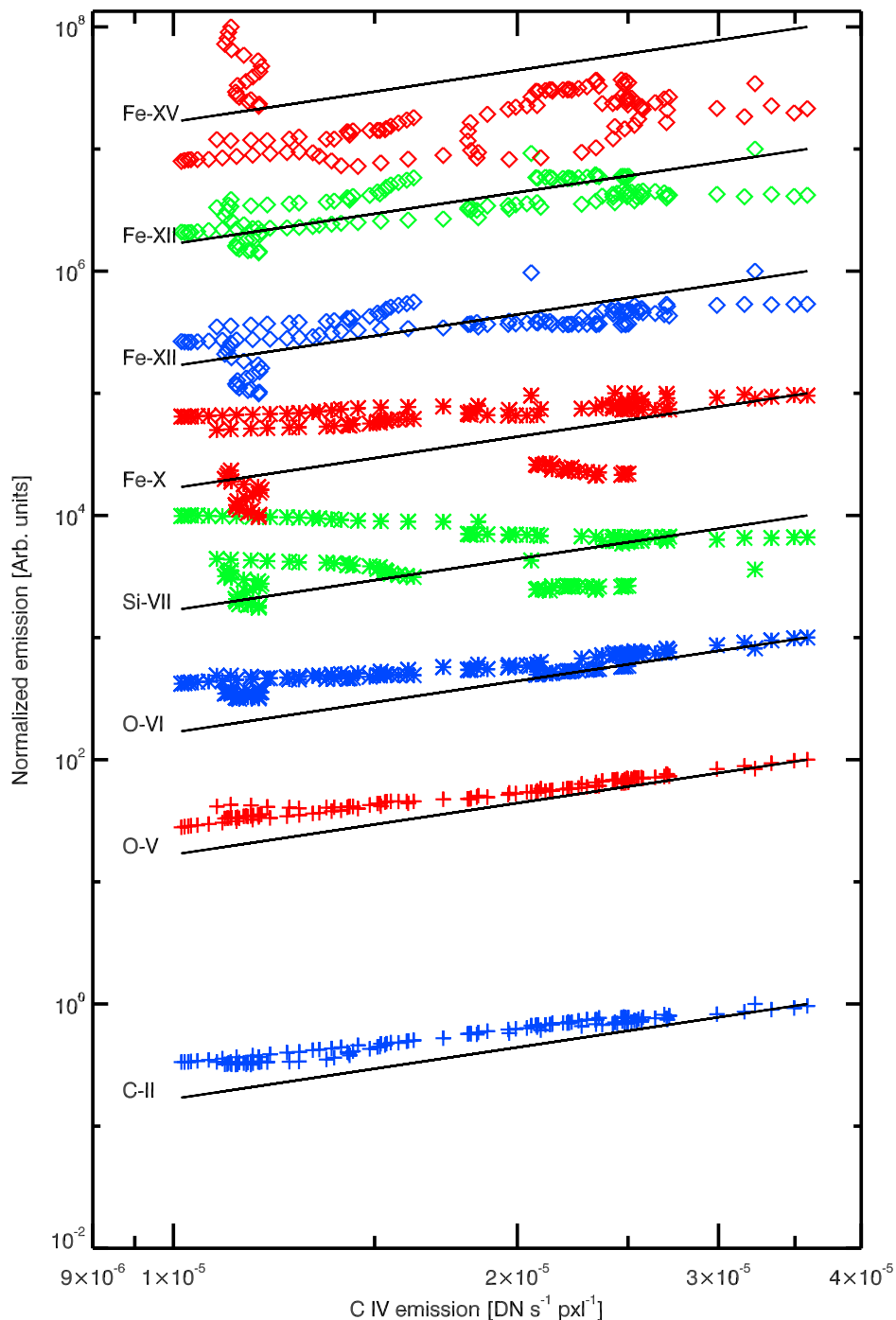


Figure 6.8: The normalized emission of several synthesized emission lines. The ion responsible for the emission line is indicated on the left. The black line shows the relation $F_{C\,IV}^{1.4}$ which is expected from observations.

6.4 Conclusion & Discussion

In this chapter we have described investigation of the effect of a varying magnetic photospheric field strength on the coronal dynamics. This was done with six nearly identical numerical experiments of a corona in a box, just differing the amount of magnetic flux. Four different amplitudes of the magnetic field were applied, where two of the models had an additional experiment with a stronger granular driving velocity.

The total Ohmic heating rates do not line up everywhere with the magnetic field strength at the bottom boundary. The horizontally averaged heating rates around the TR appear all to be around the same amplitude. The total flux in this region also no longer scale with the magnetic field strength. However, roughly 20 Mm above the TR, the total energy flux starts to scale with the magnetic field strength. When investigating a proxy for the Poynting flux, the product of the vertical magnetic field with the horizontal velocities, we find a relation where the total energy deposition above the base of the TR, lines up with $(u_h B_v)^3$ at that location.

The emission structures of the coronae produced by these models are very similar, in the sense that they all produce a hot, loop-dominated corona. The Doppler shift, however, are very similar. Of the six runs, only run 2.1 and 2.2 produce a similar pattern as observed in Solar observations. The different distribution of the Doppler-shift as a function of line formation temperature are consistent with the results of Linsky et al. (2012a) and Linsky et al. (2012b). E.g. the emission lines from hotter plasma are more red shifted for higher magnetic activity than for lower activity.

Whether the behaviour of the runs with the weakest magnetic field is possible oscillatory could not be determined in this work. Changing the simulation parameters to allow the simulation to overcome the numerical instabilities would also make the simulation incomparable with the other runs. It would be non-the-less interesting to see whether we can reproduce this observed behaviour in a future, more specialized numerical set-up. And, in case we reproduce the oscillatory behaviour, what the cause of this behaviour is, and if it is possible to trace back this behaviour to observed regions on the Solar surface.

The models are limited in the ranges of magnetic fields covered. For a full coverage and a proper investigation of the relation between magnetic field strength and corona one would need a much larger range of photospheric magnetic field strengths. But magnetic fields that are much stronger, by orders of magnitude, or weaker do not only influence the corona, but also the lower lying regions. Magneto-convective simulations of the convective layer show that very strong magnetic fields have a significant effect on the convective motion. Naturally this leads to a coronal structures very different from the Solar corona. For a model description of these regions this requires proper treatment of the lower atmospheric regions in order to have a driver matching the both the distribution of magnetic fields and velocities. This would require the combination of the results of magneto-convective simulations with coronal models as presented in this work. A first step in this direction, of coupling convective models with coronal model, is taken by F. Chen, 2013 (Priv. Comm.). This work the couples results from a model of an emerging flux-tube in the convective layer is coupled with a coronal model.

7 Testing parametrizations of coronal heating

7.1 Goal

In this chapter we investigate the effect of a different heating distribution on the corona and its dynamics. We do this by replacing the heating by Ohmic dissipation in Eq. (3.3.3) by parametrizations for heating mechanisms via *MHD turbulence* and *Alfvén wave dissipation*. We use this to explore the observational consequences of the different heating mechanisms using 3D MHD numerical experiments. The main goal is to identify to what extent such different parametrizations would lead to differences in coronal emission that can be distinguished by current instrumentation. Synthesized EUV emission and Doppler shifts provide insight on which of these mechanisms is dominant.

7.2 Model set-up

The basic set-up of the numerical experiments discussed in this chapter is described in chapter 4. In the work presented in this chapter we replace the heating by Ohmic dissipation in Eq. (3.3.24) with two parametrizations based on Alfvén wave dissipation (see van Ballegooijen et al. (2011), Sect. 4.5.2) and MHD turbulence (see Rappazzo et al. (2006), Sect. 4.5.3). We still allow for Ohmic dissipation in the induction equation, which is required for numerical stability, but the energy removed by Ohmic dissipation is not fed back into the energy equation. As a reference and starting point for these models we use the results at 45 solar time from the fully self consistent run 2.2 with Ohmic dissipation ($B_0 \propto 1.8$ and $u_0 = 2$), which was presented in the previous chapter.

For a fair comparison of the different models we scale the parametrizations so that the total energy deposition into the corona is roughly the same as the Ohmic heating. For this we extract the total energy deposition through Ohmic dissipation in the reference run at 45 minutes into the simulation. At this point the heating rates are steady in time (Fig. 6.3). The mean rms-velocity and the vertical velocity in the domain are indicated in Fig. 7.1. The orange dashed line shows the rms velocity and the blue dotted the averaged vertical velocities (for comparison, the soundspeed is about 100 km s^{-1}). The vertical black dashed line indicates at what time we chose the snapshot from the reference run to use as the starting point of the runs with the parametrized heating. Since both velocities vary relatively little in time, and together with the plateau in the heating rate from the top panel

of Fig. 6.3, we assume that we reached a quasi steady state.

For the scaling of the heating the total energy input by Ohmic dissipation into the corona in the reference is calculated by upward integrating the total Ohmic heating from the average height where the temperature reaches $\log T[\text{K}] = 5.0$. This is where the TR is located. We used this result to scale the Eqs. (4.5.2) and (4.5.3) to ensure a roughly equal energy deposition into the corona.

This is effectively the same as finding the combined values of the constants in those equations, which are otherwise not available in our set-up. One could argue that u_{rms} is available in our model, however, extracting these values would require additional communication with the processors at the bottom boundary to retrieve the velocity field there. The latter would then still be inaccurate since u_{rms} represents the velocity field *within* a magnetic patch, *not* the bulk flow.

The heating rates very close to the bottom boundary are artificially set to 0. This is to avoid numerical problems due to extremely high heating rates from very small loops. In this region the radiative losses are very high in comparison with the expected heating rates, it would effectively cool any heated plasma back to about 3500 K within one time-step. The radiative losses below that temperature are nearly 0, and the plasma does not cool further than that. Since our main interest lies in the corona and its dynamics, and the lower chromospheric regions mainly as a mass reservoir, we can justify turning off the heating in the bottom layer of our physical domain.

In order to calculate the full parametrized heating, we need the length of the magnetic field-line at each point in the box. We trace the magnetic field-lines with the method described in Sect. 4.8. In this work we assume that the lengths of the field-lines does not change significantly in time during the runs. To ensure our assumption is valid we turn off the granular velocity driver at the bottom boundary. In contrast to the braiding mechanism, a driver is not required for the parametrized heating of the plasma.

The horizontally averaged heating rates for the three numerical experiments over height are depicted in Fig. 7.2. These heating rates are for the Ohmic heating at 45 minutes (the snapshot used as initial condition for the 2 parametrized runs), for the Alfvénic and turbulent heating these curves are calculated at 50 minutes into the simulation. In here we see that the heating for the 2 parametrizations are differently distributed from Ohmic heating. The heating rates are all of the same order, which confirms that the scaling of the heating works properly. Also each heating rate drops exponentially with height. The dashed line indicates a fit-by-eye which is used to find the approximate scale heights for the heating. The scale height of the Ohmic heating and turbulent heating are with roughly 4 Mm of the same order, which matches the results of the scale heights of the heating along individual loops of Fig. 5.9. The Alfvénic heating, with a scale height of 9 Mm drops slower with height. The scale heights found in that experiment are a shorter than those in this work because those are calculated along individual field-lines, while this work examines the horizontal averages.

7.3 Results

A first check to investigate the validity of these models is to investigate their ability to retain a hot corona with a TR. A temporally and horizontally averaged profile of the

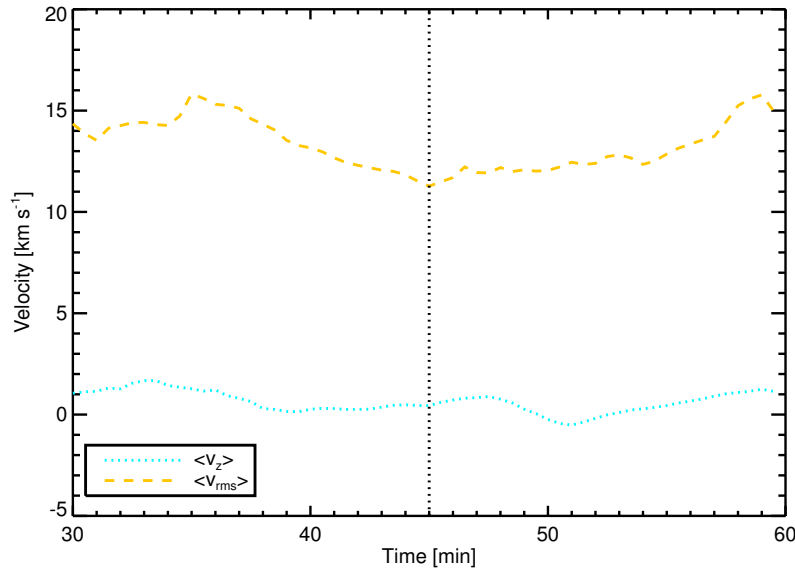


Figure 7.1: The average vertical and rms velocities of the reference run over time. The dashed line indicates snapshot-90 which is used as initial condition for the experiments with the parametrized heating. For comparison, the sound speed in the corona is of the order of 100 km s^{-1} .

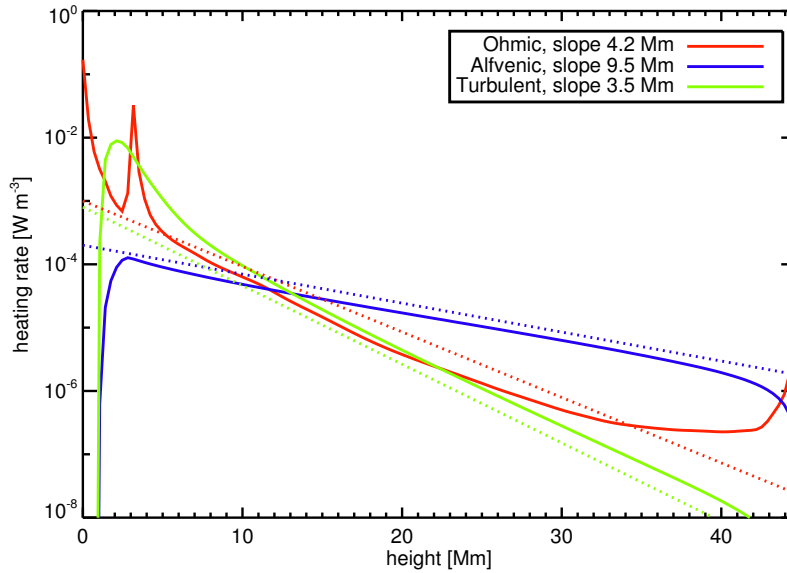


Figure 7.2: *Bottom:* Horizontally averaged heating of the different heating parametrizations over height. The dashed lines indicate a fit by eye for the scale heights, which are indicated in the legend.

temperature and density of the different runs can be seen in Fig. 7.3. The red, blue, and green curve are respectively the profiles for the reference run (Ohmic heating), Alfvénic

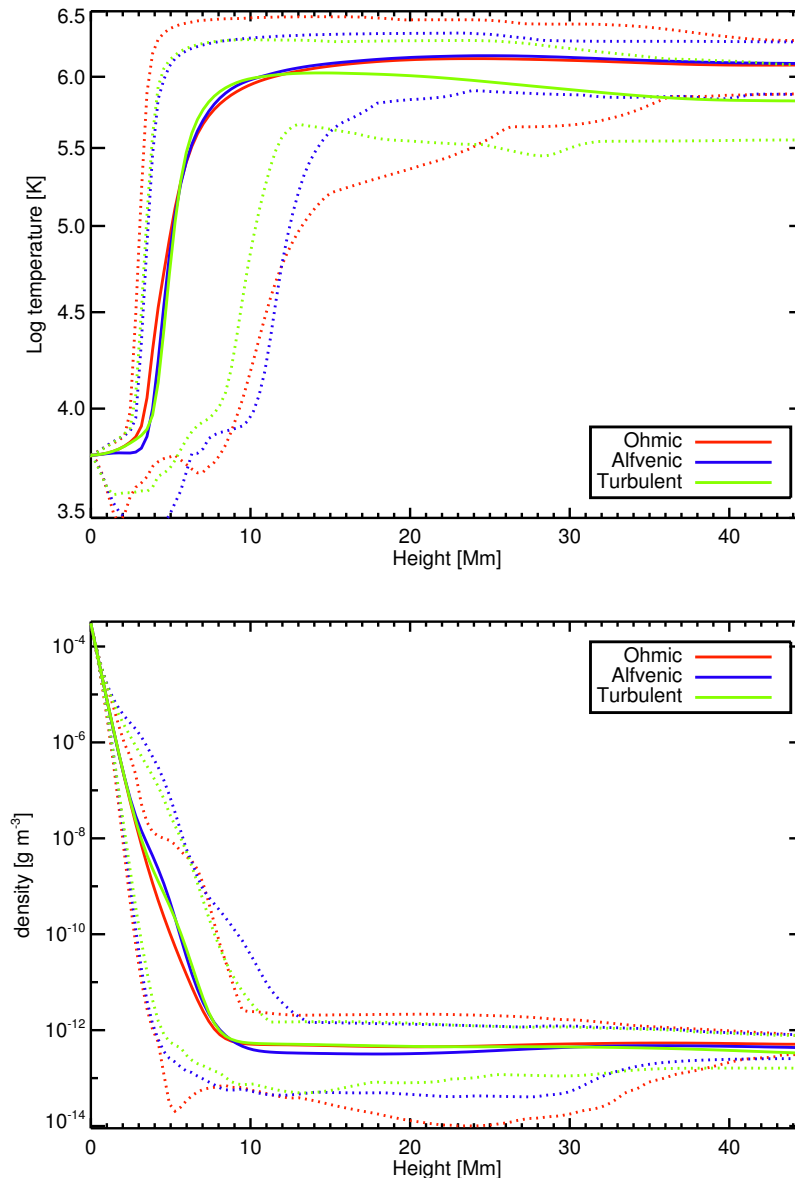


Figure 7.3: Time averaged temperature (*top*) and density (*bottom*) profile for the different heating functions over height. The red line represents the Ohmic heating, blue the Alfvénic and green the turbulent heating. The dashed lines indicate both the maxima and minima.

heating and turbulent heating. The dashed lines indicate the maxima and minima of the plotted variables. All models are able to produce a hot corona with a steep TR as far as the horizontally averaged temperatures and densities structures go. The temperature profiles are very similar, despite the spatially different heating distributions. The profiles of the minimum temperatures indicate that the actual temperature differences might not be that similar. The same is seen in the the density profile, a large variation in the maxima and minima over height, but the averages all match each other closely.

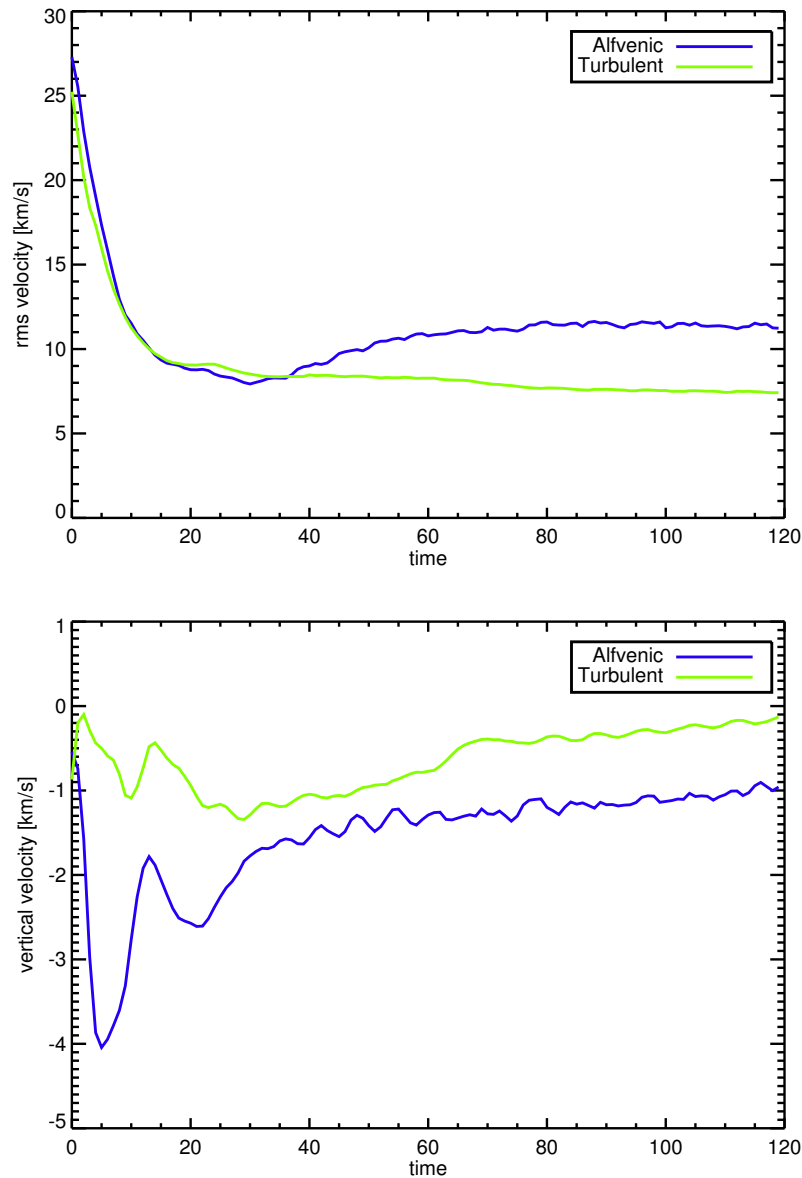


Figure 7.4: The temporal evolution of the rms velocity (*top*) and the vertical velocity (*bottom*) for the two different numerical experiments. The green line represents model with turbulent-heating and the blue line represents the Alfvénic-heating.

In Fig. 7.4 we see the average rms- and vertical velocities of the two models with the Alfvénic and Turbulent heating. This is an indication on how dynamic the runs are. Due to the more static heating in time and the lack of a driver, the velocities in these models are significantly lower than in the reference run. Initially the sudden change of the heating leads to a change in pressure balance, and as such an increase in velocities. In time the rms-velocities damp out and the models reach a quasi steady state.

7.3.1 Emission

We use the same method as described in Sect. 6.3 to produce synthetic observations of our experiments. The resulting synthetic emission for the models result in overall similar emission structures. This is displayed in Figs. 7.5 to 7.7 for different response functions corresponding to three AIA/SDO filters (Lemen et al. 2012). These are the 131 Å which corresponds to 5.6, 7.0 and 7.2 $\log T[\text{K}]$, 171 Å which has a peak in the response function at 5.8 $\log T[\text{K}]$, and the 193 Å filter, which correspond to 6.1 $\log T[\text{K}]$. In each figure from left to right the synthetic observations are calculated from the reference run at 45 minutes, then the Alfvénic and turbulent heating parametrizations at 50 minutes.

Each parametrization produces a loop dominated corona, including stronger emission at the foot-points. The synthetic emission from the reference run are more chaotic and structured, which can be attributed to the driver. The granular velocity driver causes more short and small scale heating events, which results in more small-scale structures in emission, whereas the parametrized heating is nearly constant in time. At the top of the domain the emission from the models with parametrized heating is lower than that of the reference model, for the latter the heating at the top of the domain actually increases as a result of the imperfect boundary conditions.

Beside details such as the exact location of the loop brightnings, there are no features that would set one model aside as non-coronal. Each model produces emission structures that are coronal-like, and as such, these integrated emission structures cannot be used to distinguish between different heating mechanisms.

7.3.2 Doppler shifts

The thermal energy of an heating event along a coronal loop is spread rapidly along the whole of the loop as a result of the efficient heat conduction. This nearly isothermal loop would then appear also nearly uniform in emission, independent on where the actual heating event took place. We would therefore expect no major difference in the emission structures. Beside intensity observation we also have access to Doppler observations.

A different distribution of heating in the corona would lead to different velocity distributions, since the resulting pressure increase would accelerate the plasma in the loop. The flow of mass in a loop heated at the top would be different from a loop heated near the foot points, as long as no equilibrium has been reached. The first would produce initially down flows, while the latter would produce upflows into the loop. A more localized heating at a point along the loop would induce a combination of up- and downflows. Therefore we expect that a different distribution of heating unambiguously leads to differently observed Doppler shifts. Therefore comparing Doppler shift of synthesized emission lines, might provide important information on the most likely heating mechanism.

We investigate the Doppler shifts of the three numerical experiments as function of formation temperature. These are displayed in the left panels of Fig. 7.8 for every 90 seconds, over a timespan of 15 minutes, indicated with different colours. These are centred around 45 minutes into the simulation for the Ohmic heating and centred around 50 minutes for the Alfvénic and turbulent heating mechanisms. The colours indicate the time, from blue to green to red indicates further in time. The black line represents the averaged Doppler

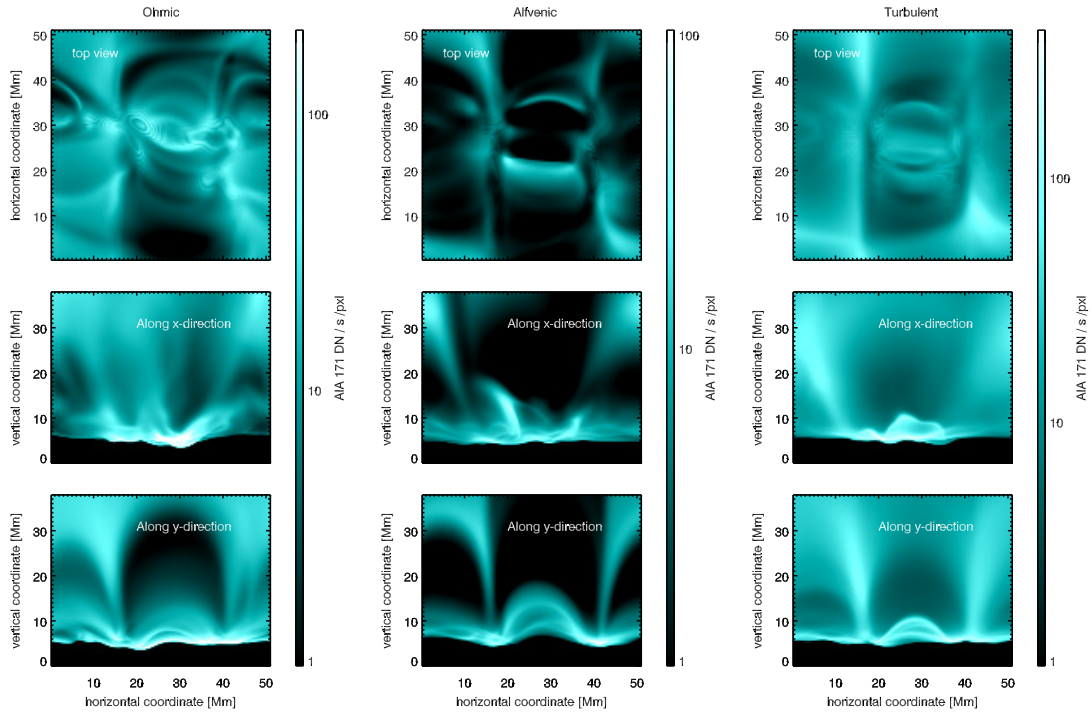


Figure 7.5: Integrated emission as it would be observed by the 131 \AA filter of SDO/AIA. This filter has maxima in response function around 5.6 , 7.0 and $7.2 \log T[\text{K}]$. The colour scale is scaled logarithmically, and the range is chosen individually for each run for clarity. The runs are, from left to right, the reference run (Ohmic heating), the run heated according to a parametrization of Alfvén wave dissipation, and the run heated through the parametrization of MHD turbulence. The top panel shows the integrated intensities along the z -axis. The middle and bottom panel show the sideview from the box along respectively the x and y -axis.

shifts derived from the synthesized emissions lines. The vertical bars show the 0.1σ spread of the observed Doppler shifts. The results for the reference run are discussed in the previous chapter in Sect. 6.3.2. The right panels in Fig. 7.8 show the Doppler shifts of the vertical integrated emission line profiles. This represents what EUV spectrometers, e.g. SoHo/SUMER, Hinode/EIS, would actually observe.

As already expected from Fig. 7.4 the derived Doppler shift patterns are stable in time, they are, however, not zero. Based on these results the turbulent heating, heating through current cascades, produces the best match with observed Doppler shifts in active regions. It shows the same tendency as the dashed line in Fig. 2.2, which dips toward blue-shifts at higher temperatures. This shows that different heating distributions have a clear distinct Doppler pattern and can therefore be used as a probe for the heating distribution.

7.3.3 Direct comparison of heat input for parametrizations

The heating distributions for both parametrizations are compared to the Ohmic heating distribution in Fig. 7.9. This figure compares the Ohmic heating in the grid points of the

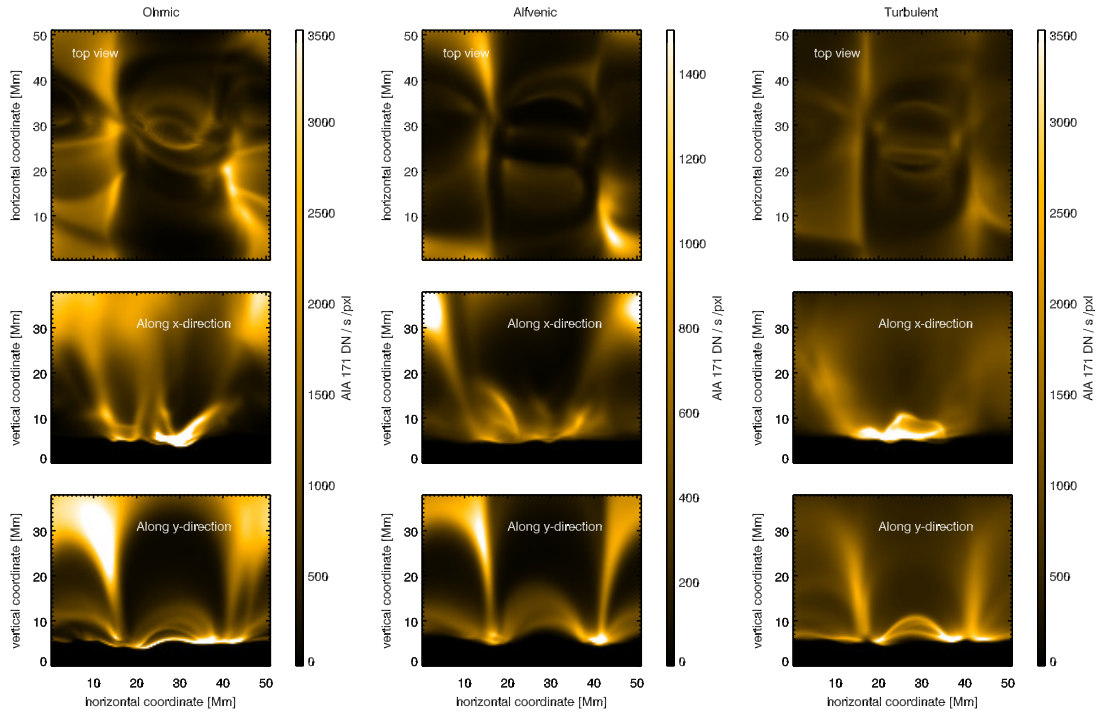


Figure 7.6: Same as Fig. 7.5, but for the 171 Å filter of SDO/AIA, which has a response function that peaks at $5.8 \log T[\text{K}]$.

reference run with the Turbulent or Alfvénic heating at those grid points at 50 minutes into the simulation. The black lines indicates the values where the heating rates would be the same. The figure is a 2D histogram, where colour indicates the amount of points corresponding to that combination of heating rates. Two concentrations of points at the bottom of the plot correspond to heating along the field-lines that leave the domain at the top (and have therefore a very long length associated with it), and have nearly no heating for the parametrizations. The heating for the turbulence case follows the Ohmic heating closer than the Alfvénic heating.

7.4 Discussion and conclusion

In this chapter we discussed the results of numerical experiments in which we replaced the Ohmic heating with a parametrized version of an heating mechanism. These parametrized heating functions depended on local variables such as, ρ , L or B . We did this by using the results of the self consistent run 2.2 of the previous chapter as reference model for the Ohmic heating and as a starting point. At the 45 minute mark we used a snapshot as the initial condition for two runs with the parametrized heating. Also at that point we trace the length of each field-line going through each grid point in the box, this information is then used for the parametrized heating according to Eqs. (4.5.2) and (4.5.3). This assumes that during the run the length of the field-lines do not change significantly. For this purpose the granular driver at the bottom boundary is turned off. The parametrized heating is then scaled to ensure that the total energy deposition in the corona is roughly the same as for

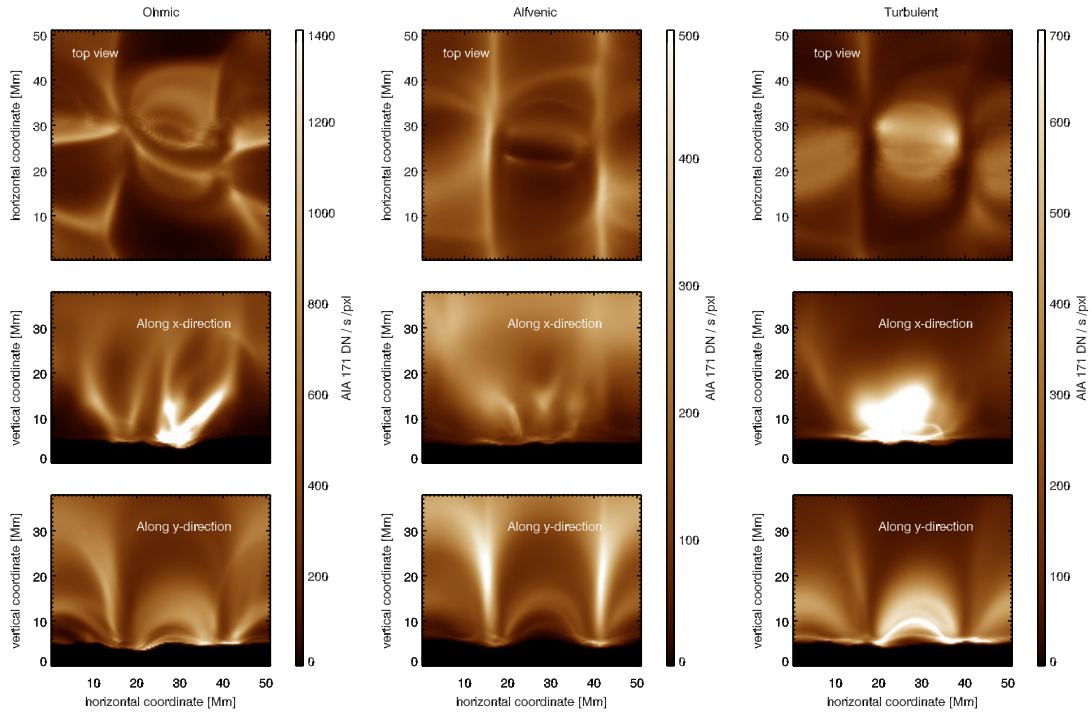


Figure 7.7: Same as Fig. 7.5, but for the 193 \AA filter of SDO/AIA, which has a response function that peaks at $5.8 \log T[\text{K}]$.

the Ohmic heating.

We see that each parametrization is able to produce a hot and loop-dominated corona as far as the synthesized emission structures go. From these images alone one would not be able to identify the heating distribution. Therefore the synthesized emission is insufficient to distinguish between the heating parametrizations. We therefore turn to the Doppler shifts, which are more sensitive to a difference in heating distribution. The Doppler shifts of vertically integrated emission lines as a function of formation temperature show that the different parametrizations show a significantly different pattern. The most Solar-like profile is found for the experiment with the parametrization based on turbulent heating.

The results of this work show that it is possible to investigate different heating mechanisms by replacing the standard heating with a parametrization. This adds the possibility to investigate heating mechanisms outside the scope of this work. One of these is a suggestion by Van Doorselaere et al. (2007), based on heating through wave dissipation.

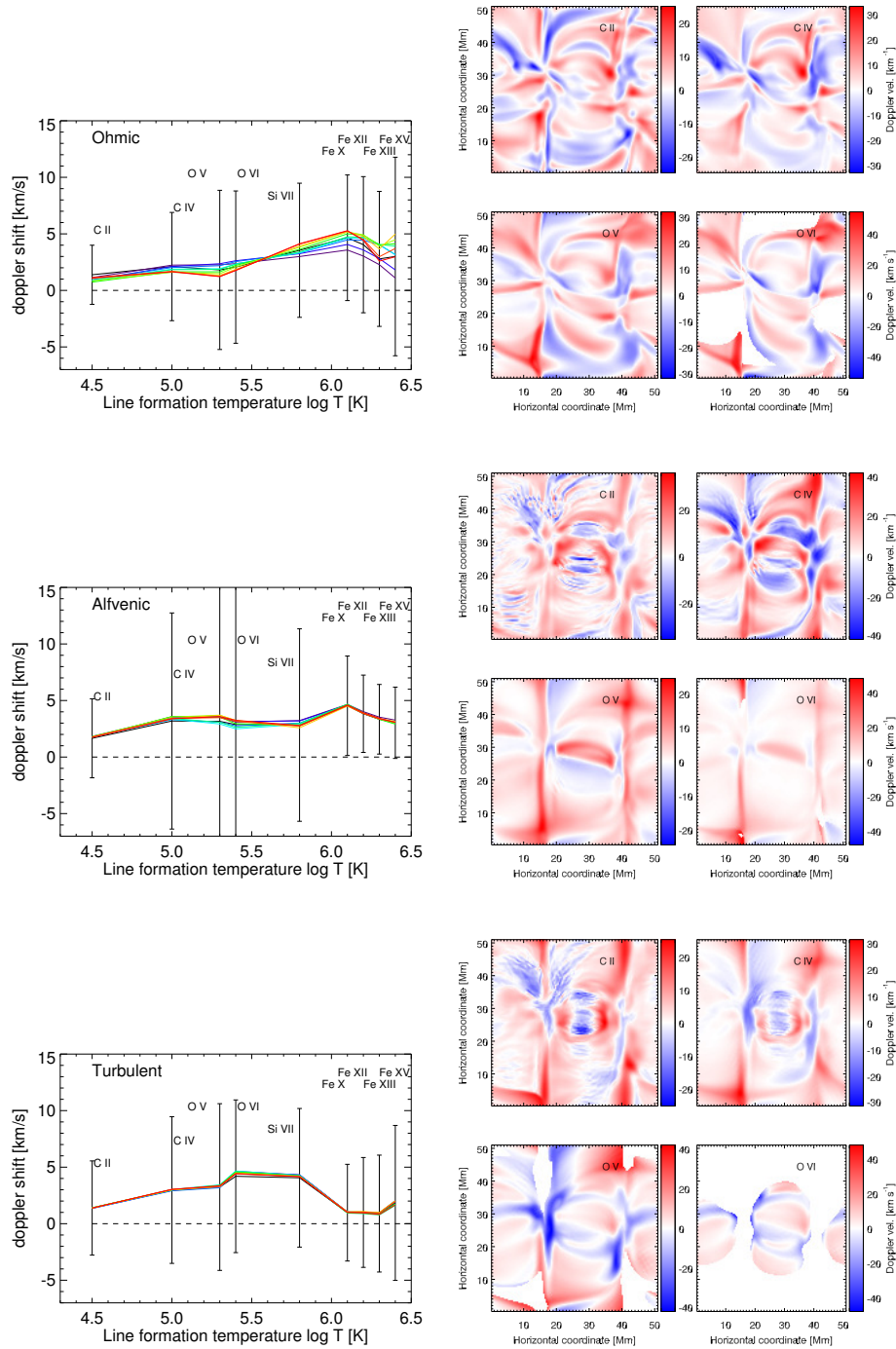


Figure 7.8: The Doppler shifts around 45 minutes (Ohmic heating) and 50 minutes (Alfvénic and turbulent heating) in the simulation. The left panels show the doppler shifts as a function of the line formation temperature. The coloured lines represent the Doppler shifts of one snapshot for every 90 seconds, over a timespan of 15 minutes centred around 45 minutes Solar time. The black line shows the average of these and the vertical bars represent the 0.1σ spread. The right panel show the Doppler shifts of the vertical integrated emission line profiles. For the C II, C IV, O V and O VI lines. From top to bottom the figures are come the run with Ohmic heating, Alfvénic heating and turbulent heating.

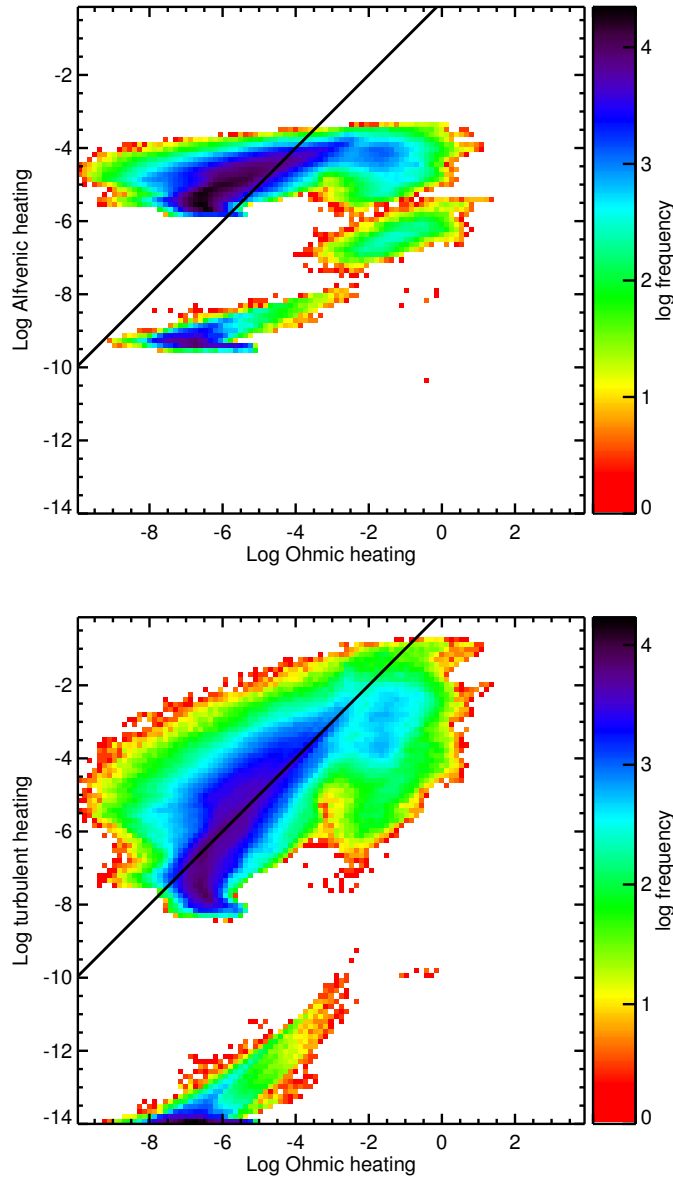


Figure 7.9: Comparison of the two parametrizations of the heating rate with the Ohmic heating. The plot shows the Ohmic heating at one point compared to the Alfvénic or turbulent heating at that point. The colour indicates the density of those points. The black line divides the plot in two halves, above the line the parametrized heating is higher than the Ohmic heating and below the line vice versa. The top panel is a comparison of the Ohmic heating with the Alfvénic heating distribution, the bottom panel the Ohmic heating with the turbulent heating distribution.

8 Discussion and conclusion

8.1 Conclusion

In this work we have investigated the dynamics of the corona when subject to different Poynting flux of heating distributions. Two different heating distributions were chosen according to a parametrization derived from results of RMHD-models. These models were based on dissipation Alfvén waves (van Ballegooijen et al. 2011) and MHD turbulence (Rappazzo et al. 2006).

As a first step we looked at how the parametrized heating distributions along individual closed magnetic field-lines in a self consistent 3D MHD model behaved. This model was heated self-consistently through Ohmic dissipation, driven by photospheric granular motion. From that we investigated whether a different distribution of the heating in such a loop would produce a different corona. We found that the Alfvénic heating had a longer scale height than the turbulent heating. For the latter the scale height was similar to that of heating through Ohmic dissipation, which is not too surprising as both are derived from the same principles.

Next we investigated the influence of the photospheric magnetic field strength on the heating and dynamics of the corona. The results were surprising in the sense that the actual heating not necessarily scales with the magnetic field strength in the photosphere. Although the heating in the whole of the physical domain scales with the photospheric magnetic field, the heating in the corona does not. Instead the heating scales with a measure of the pointing flux at the height of the TR. These Poynting fluxes do not scale with the photospheric magnetic field strength.

Comparing the results of these models with observations of magnetic active stars we found an interesting match with Doppler shifts patterns as a function of line formation temperature. A similar interesting correlation was found for the C IV emission and emission from highly ionized iron, such as Fe XV and Fe XII. Observation found a similar relation for the X-ray flux with the magnetic flux, which in turn scales with the observed flux from C IV. The model set-up only covers a small range of the parameters, and as such it could prove fruitful to expand this range in future work. We use one model of this work in which we replace the heating by Ohmic dissipation with a parametrized version of the heating. We did this for Alfvénic heating and for turbulent heating. The experiments with these parametrized heating use a snapshot of the model heated through Ohmic dissipation at 45 minutes as a starting point. Since the parametrized heating does not require braiding of magnetic fields the granular driver is turned off. To ensure a proper comparison we scale the parametrizations so that the total heating in the corona is the same as for the Ohmic heating. We find that the different heating distributions all produce

a corona in the emission structures derived from synthesized emission. If these were actual observations they would not provide a hint on the actual heating distribution. Doppler shift from synthesized line emission does produce distinct patterns, and as such could be used as a test on which heating mechanism is most likely.

8.2 Outlook

The work described in this thesis leaves room for additional investigation. In the experiment done on the effect of the photospheric magnetic field strengths several improvements could be made. First of all, a stronger magnetic field would lead to longer scale height for the magnetic field, and as such would require a larger computational domain. Too strong magnetic configuration would be significantly influenced by itself through the periodic boundaries. A larger set-up would allow for a less constrained expansion of the magnetic field, and inclusion of quiet Sun magnetic fields would be able to "shield" strong magnetic fields from itself (through the periodic boundaries). Also, a stronger magnetic field would influence the granular motion, an effect not included in our current simulations.

In this work we only replaced the Ohmic heating with two other parametrizations. The results showed that it is feasible to replace the Ohmic heating with a parametrized version. Future work would expand this to include a wider variety of heating parametrizations.

Bibliography

- Adams, D., 1984, *So Long, and Thanks for All the Fish*, Pan Books, UK; Harmony Books, US.
- Alfvén, H. H., 1941, On the solar corona, *Arkiv för Matematik, Astronomi och Fysik*, 27
- Aschwanden, M. J., 2004, *Physics of the Solar Corona. An Introduction*, Praxis Publishing Ltd
- Aschwanden, M. J., Winebarger, A., Tsiklauri, D., Peter, H., 2007, The coronal heating paradox, *ApJ*, 659, 1673–1681
- Athay, R. G., 1984, The origin of spicules and heating of the lower transition region, *ApJ*, 287, 412–417
- Bingert, S., Peter, H., 2011, Intermittent heating in the solar corona employing a 3D MHD model, *A&A*, 530, A112, 1103.6042
- Boerner, P. F., Edwards, C. G., Lemen, J. R., et al., 2012, Initial Calibration of the Atmospheric Imaging Assembly (AIA) on the Solar Dynamics Observatory (SDO), *Sol. Phys.*, 275, 41–66
- Boris, J. P., Mariska, J. T., 1982, An explanation for the systematic flow of plasma in the solar transition region, *ApJ*, 258, L49–L52
- Brandenburg, A., Dobler, W., 2002, Hydromagnetic turbulence in computer simulations, *Computer Physics Communications*, 147, 471–475, [arXiv:astro-ph/0111569](#)
- Bushby, P. J., Houghton, S. M., Proctor, M. R. E., Weiss, N. O., 2008, Convective intensification of magnetic fields in the quiet Sun, *MNRAS*, 387, 698–706, 0804.1238
- Cattaneo, F., Emonet, T., Weiss, N., 2003, On the Interaction between Convection and Magnetic Fields, *ApJ*, 588, 1183–1198
- Cook, J. W., Cheng, C.-C., Jacobs, V. L., Antiochos, S. K., 1989, Effect of coronal elemental abundances on the radiative loss function, *ApJ*, 338, 1176–1183
- Dere, K. P., Landi, E., Mason, H. E., Monsignori Fossi, B. C., Young, P. R., 1997, CHIANTI - an atomic database for emission lines, *A&AS*, 125, 149–173
- Dowdy, Jr., J. F., Rabin, D., Moore, R. L., 1986, On the magnetic structure of the quiet transition region, *Sol. Phys.*, 105, 35–45

- Edlén, B., 1943, Die Deutung der Emissionslinien im Spektrum der Sonnenkorona. Mit 6 Abbildungen., *ZAp*, 22, 30
- Gabriel, A. H., 1976, A magnetic model of the solar transition region, *Royal Society of London Philosophical Transactions Series A*, 281, 339–352
- Grotian, W., 1931, Ergebnisse der Potsdamer Expedition zur Beobachtung der Sonnenfinsternis am 9. Mai 1929 in Takengon (Nordsumatra). 6. Mitteilung. Über die Intensitätsverteilung des kontinuierlichen Spektrums der inneren Korona. Mit 8 Abbildungen. (Eingegangen am 27. Juni 1931), *ZAp*, 3, 199
- Grotian, W., 1934, Über das Fraunhofersche Spektrum der Sonnenkorona. Mit 10 Abbildungen., *ZAp*, 8, 124
- Güdel, M., 2004, X-ray astronomy of stellar coronae, *A&A Rev.*, 12, 71–237, [arXiv:astro-ph/0406661](#)
- Gudiksen, B. V., Nordlund, Å., 2002, Bulk Heating and Slender Magnetic Loops in the Solar Corona, *ApJ*, 572, L113–L116
- Gudiksen, B. V., Nordlund, Å., 2005a, An Ab Initio Approach to the Solar Coronal Heating Problem, *ApJ*, 618, 1020–1030, [arXiv:astro-ph/0407266](#)
- Gudiksen, B. V., Nordlund, Å., 2005b, An AB Initio Approach to Solar Coronal Loops, *ApJ*, 618, 1031–1038, [arXiv:astro-ph/0407267](#)
- Hansteen, V. H., Hara, H., De Pontieu, B., Carlsson, M., 2010, On Redshifts and Blueshifts in the Transition Region and Corona, *ApJ*, 718, 1070–1078, [1001.4769](#)
- Ionson, J. A., 1978, Resonant absorption of Alfvénic surface waves and the heating of solar coronal loops, *ApJ*, 226, 650–673
- Karpen, J. T., Antiochos, S. K., Klimchuk, J. A., 2006, The origin of high-speed motions and threads in prominences, *ApJ*, 637, 531–540
- Klimchuk, J. A., 2006, On Solving the Coronal Heating Problem, *Sol. Phys.*, 234, 41–77, [arXiv:astro-ph/0511841](#)
- Lemen, J. R., Title, A. M., Akin, D. J., Boerner, P. F., Chou, C., Drake, J. F., Duncan, D. W., Edwards, C. G., Friedlaender, F. M., Heyman, G. F., Hurlburt, N. E., Katz, N. L., Kushner, G. D., Levay, M., Lindgren, R. W., Mathur, D. P., McFeaters, E. L., Mitchell, S., Rehse, R. A., Schrijver, C. J., Springer, L. A., Stern, R. A., Tarbell, T. D., Wuelser, J.-P., Wolfson, C. J., Yanari, C., Bookbinder, J. A., Cheimets, P. N., Caldwell, D., Deluca, E. E., Gates, R., Golub, L., Park, S., Podgorski, W. A., Bush, R. I., Scherrer, P. H., Gumm, M. A., Smith, P., Aufer, G., Jerram, P., Pool, P., Soufli, R., Windt, D. L., Beardsley, S., Clapp, M., Lang, J., Waltham, N., 2012, The Atmospheric Imaging Assembly (AIA) on the Solar Dynamics Observatory (SDO), *Sol. Phys.*, 275, 17–40
- Linsky, J. L., Bushinsky, R., Ayres, T., Fontenla, J., France, K., 2012a, Far-ultraviolet Continuum Emission: Applying This Diagnostic to the Chromospheres of Solar-mass Stars, *ApJ*, 745, 25, [1109.5653](#)

- Linsky, J. L., Bushinsky, R., Ayres, T., France, K., 2012b, Ultraviolet Spectroscopy of Rapidly Rotating Solar-Mass Stars: Emission-line Redshifts as a Test of the Solar-Stellar Connection, *ApJ*, 754, 69, 1205.6498
- Longcope, D. W., 2005, Topological Methods for the Analysis of Solar Magnetic Fields, *Living Reviews in Solar Physics*, 2, 7
- Müller, D., Hansteen, V. H., Peter, H., 2003, Dynamics of solar coronal loops. I. Condensation in cool loops and its effect on transition region lines, *A&A*, 411, 605–613
- Parker, E. N., 1972, Topological Dissipation and the Small-Scale Fields in Turbulent Gases, *ApJ*, 174, 499
- Parker, E. N., 1983, Magnetic Neutral Sheets in Evolving Fields - Part Two - Formation of the Solar Corona, *ApJ*, 264, 642
- Patsourakos, S., Klimchuk, J. A., 2006, Nonthermal Spectral Line Broadening and the Nanoflare Model, *ApJ*, 647, 1452–1465
- Peter, H., 2007, Modeling the (upper) solar atmosphere including the magnetic field, *Advances in Space Research*, 39, 1814–1825, [arXiv:astro-ph/0703575](#)
- Peter, H., Bingert, S., 2012, Constant cross section of loops in the solar corona, *A&A*, 548, A1
- Peter, H., Bingert, S., 2012, Constant cross section of loops in the solar corona, *ArXiv e-prints*, 1209.0789
- Peter, H., Judge, P. G., 1999, On the Doppler Shifts of Solar Ultraviolet Emission Lines, *ApJ*, 522, 1148–1166
- Peter, H., Gudiksen, B., Nordlund, Å., 2004, Coronal heating through braiding of magnetic field lines, *ApJ*, 617, L85–L88
- Peter, H., Gudiksen, B., Nordlund, Å., 2006, Forward modeling of the corona of the sun and solar-like stars: from a three-dimensional magnetohydrodynamic model to synthetic extreme-ultraviolet spectra, *ApJ*, 638, 1086–1100
- Peter, H., Bingert, S., Kamio, S., 2012, Catastrophic cooling and cessation of heating in the solar corona, *A&A*, 537, A152, 1112.3667
- Pevtsov, A. A., Fisher, G. H., Acton, L. W., Longcope, D. W., Johns-Krull, C. M., Kankelborg, C. C., Metcalf, T. R., 2003, The Relationship Between X-Ray Radiance and Magnetic Flux, *ApJ*, 598, 1387–1391
- Priest, E. R., 1982, *Solar magneto-hydrodynamics*
- Rappazzo, A. F., Dahlburg, R. B., Einaudi, G., Velli, M., 2006, Nonlinear interactions in coronal heating, *Advances in Space Research*, 37, 1335–1341
- Rappazzo, A. F., Velli, M., Einaudi, G., Dahlburg, R. B., 2008, Nonlinear dynamics of the parker scenario for coronal heating, *ApJ*, 677, 1348–1366

- Reeves, E. M., 1976, The EUV chromospheric network in the quiet sun, *Sol. Phys.*, 46, 53–72
- Reiners, A., 2012, Observations of Cool-Star Magnetic Fields, *Living Reviews in Solar Physics*, 9, 1, 1203.0241
- Rosner, R., Tucker, W. H., Vaiana, G. S., 1978, Dynamics of the quiescent solar corona, *ApJ*, 220, 643–645
- Saar, S. H., 2001, Recent Measurements of (and Inferences About) Magnetic Fields on K and M Stars (CD-ROM Directory: contribs/saar1), in 11th Cambridge Workshop on Cool Stars, Stellar Systems and the Sun, (Eds.) R. J. Garcia Lopez, R. Rebolo, M. R. Zapaterio Osorio, vol. 223 of Astronomical Society of the Pacific Conference Series, p. 292
- Schrijver, C. J., 1990, Relations between the photospheric magnetic field and the emission from the outer atmospheres of cool stars. II - The C IV 1550 Å doublet, *A&A*, 234, 315–322
- Schrijver, C. J., Cote, J., Zwaan, C., Saar, S. H., 1989, Relations between the photospheric magnetic field and the emission from the outer atmospheres of cool stars. I - The solar CA II K line core emission, *ApJ*, 337, 964–976
- Serio, S., Peres, G., Vaiana, G. S., Golub, L., Rosner, R., 1981, Closed coronal structures. II - Generalized hydrostatic model, *ApJ*, 243, 288–300
- Spadaro, D., Lanza, A. F., Karpen, J. T., Antiochos, S. K., 2006, A Transient Heating Model for the Structure and Dynamics of the Solar Transition Region, *ApJ*, 642, 579–583
- Spitzer, L., 1962, *Physics of Fully Ionized Gases*
- Stein, R. F., Nordlund, Å., 2006, Solar Small-Scale Magnetoconvection, *ApJ*, 642, 1246–1255
- Tian, H., Marsch, E., Curdt, W., He, J., 2009, Upflows in Funnel-like Legs of Coronal Magnetic Loops, *ApJ*, 704, 883–890, 0909.0739
- Tomczyk, S., McIntosh, S. W., Keil, S. L., Judge, P. G., Schad, T., Seeley, D. H., Edmondson, J., 2007, Alfvén Waves in the Solar Corona, *Science*, 317, 1192–
- van Ballegooijen, A. A., 1986, Cascade of magnetic energy as a mechanism of coronal heating, *ApJ*, 311, 1001–1014
- van Ballegooijen, A. A., Asgari-Targhi, M., Cranmer, S. R., DeLuca, E. E., 2011, Heating of the Solar Chromosphere and Corona by Alfvén Wave Turbulence, *ApJ*, 736, 3, 1105.0402
- Van Doorselaere, T., Andries, J., Poedts, S., 2007, Observational evidence favors a resistive wave heating mechanism for coronal loops over a viscous phenomenon, *A&A*, 471, 311–314

- van Wettum, T., Bingert, S., Peter, H., 2013, Parameterisation of coronal heating: spatial distribution and observable consequences, *A&A*, 554, A39, 1303.1371
- Vögler, A., Shelyag, S., Schüssler, M., Cattaneo, F., Emonet, T., Linde, T., 2005, Simulations of magneto-convection in the solar photosphere. Equations, methods, and results of the MURaM code, *A&A*, 429, 335–351
- Withbroe, G. L., Noyes, R. W., 1977, Mass and energy flow in the solar chromosphere and corona, *ARA&A*, 15, 363–387
- Zacharias, P., Peter, H., Bingert, S., 2011, Investigation of mass flows in the transition region and corona in a three-dimensional numerical model approach, *A&A*, 531, A97, 1105.5491

Publications

Refereed articles:

Parameterisation of coronal heating: spatial distribution and observable consequences.
van Wettum, T., Bingert, S., & Peter, H. 2013, A& A, 554, A39

Posters

13th ESPM, Rhodes, Greece (2011):

Response of the corona to different heating mechanisms.

Hinode 6, St. Andrews, Scotland (2012):

Response of the corona to different heating mechanisms.

Rocks 'n Stars, Göttingen, Germany (2012):

Response of the corona to different heating mechanisms.

Acknowledgements

So long, and thanks for all the fish.
(Adams 1984)

First of all I would like to thank my supervisor Hardi Peter for his excellent supervision. Also a lot of gratitude goes to Sven Bingert who supported me throughout the whole of my PhD-research and taught me the magic of MHD and the pencil code. And I thank Philippe for guiding me through the maze of German bureaucracy.

Also I want to thank Jens Niemeyer for carefully reading my thesis. I am grateful to have been part of the IMPRS, and to have had the opportunity to work on cutting edge solar system science.

Dieter for his superb supervision of the IMPRS. And I wish Sonja all the best with the the future supervision of this group of unruly PhD-students.

Thanks to the people at the GWDG computing center who's infrastructure I so graciously used for my simulation and excessive data-storage. Peter Strub and Thomas Gastine for always driving me to the middle-of-nowhere where our institute happens to be.

Many thanks to Wieland, Julia, Judith, Peter Kollmann, Feng, Robert, Farhad, Stephan, Shahin, Sebastian, Anne, Mark, David, both Maria's, Kok Leng, Borys, Fatima, Uwe, Innes, JuanJo, and anyone whom I undoubtedly forgot. I thank you all for the Brocken hikes, the interesting conversations, the cakes, the Civilization 4 weekends, and all the laughs and beers we shared.

I also like to thank my family for their support and love during this time, and for making this study possible.

よっちゃん いつも 僕を支え 励まして くれて どうも ありがとう。

Curriculum Vitae

Nationality: Dutch

Born: 21 May 1984, Nieuwegein

Civil status: Unmarried, no children

Education:

High school: VWO 2001

University of Utrecht: Starting date: 01-09-2002

-Bsc physics Finish date: 22-12-2005

University of Utrecht: Starting date: 01-09-2006

-Msc astrophysics Finish date: 02-09-2009

Master thesis: *2D MHD-Simulations of a Coronal Funnel*

Other Skills and qualifications:

Languages: Fluent: English and Dutch, basic knowledge of German and Japanese

Organisation: Scientific Organisation Committee of the Rock'n Stars conference.